



The Solar Neighborhood. LII. M Dwarf Twin Binaries—Presumed Identical Twins Appear Fraternal in Variability, Rotation, $H\alpha$, and X-Rays

Andrew A. Couperus^{1,2} , Todd J. Henry² , Rachel A. Osten^{3,4} , Wei-Chun Jao¹ , Eliot Halley Vrijmoet^{2,5} , Aman Kar^{1,2} , and Elliott Horch⁶

¹Department of Physics and Astronomy, Georgia State University, Atlanta, GA 30302, USA; andcoup1@gmail.com

²RECONS Institute, Chambersburg, PA 17201, USA

³Space Telescope Science Institute, Baltimore, MD 21218, USA

⁴Center for Astrophysical Sciences, Department of Physics and Astronomy, Johns Hopkins University, Baltimore, MD 21218, USA

⁵Five College Astronomy Department, Smith College, Northampton, MA 01063, USA

⁶Department of Physics, Southern Connecticut State University, New Haven, CT 06515, USA

Received 2024 September 20; revised 2024 October 23; accepted 2024 October 29; published 2024 December 18

Abstract

We present an investigation into the rotation and stellar activity of four fully convective M dwarf “twin” wide binaries. Components in each pair have (1) astrometry confirming they are common-proper-motion binaries, (2) Gaia BP, RP, and 2MASS J , H , and K_s magnitudes matching within 0.10 mag, and (3) presumably the same age and composition. We report long-term photometry, rotation periods, multiepoch $H\alpha$ equivalent widths, X-ray luminosities, time series radial velocities, and speckle observations for all components. Although it might be expected for the twin components to have matching magnetic attributes, this is not the case. Decade-long photometry of GJ 1183 AB indicates consistently higher spot activity on A than B, a trend matched by A appearing 58% \pm 9% stronger in L_X and 26% \pm 9% stronger in $H\alpha$ on average—this is despite similar rotation periods of A = 0.86 day and B = 0.68 day, thereby informing the range in activity for otherwise identical and similarly rotating M dwarfs. The young β Pic Moving Group member 2MA 0201+0117 AB displays a consistently more active B component that is 3.6 \pm 0.5 times stronger in L_X and 52% \pm 19% stronger in $H\alpha$ on average, with distinct rotation at A = 6.01 days and B = 3.30 days. Finally, NLTT 44989 AB displays remarkable differences with implications for spindown evolution—B has sustained $H\alpha$ emission while A shows absorption, and B is $\geq 39 \pm 4$ times stronger in L_X , presumably stemming from the surprisingly different rotation periods of A = 38 days and B = 6.55 days. The last system, KX Com, has an unresolved radial velocity companion, and is therefore not a twin system.

Unified Astronomy Thesaurus concepts: M dwarf stars (982); Magnetic variable stars (996); Stellar activity (1580); Stellar evolution (1599); Stellar rotation (1629); Wide binary stars (1801); X-ray stars (1823)

Materials only available in the online version of record: data behind figures, machine-readable table

1. Introduction

M dwarfs comprise about three-quarters of all stars in the solar neighborhood (T. J. Henry et al. 2006, 2018), and presumably all over the local Universe. They span roughly a factor of 8 in mass across their spectral range (G. F. Benedict et al. 2016; A. W. Mann et al. 2019), with stars above $\sim 0.35M_\odot$ hosting partially convective (PC) structures like our Sun while cases below $\sim 0.35M_\odot$ are fully convective (FC) without a radiative core (G. Chabrier & I. Baraffe 1997). These low-mass stars also host strong magnetic fields that cause starspots, faculae, flares, chromospheric activity, X-ray coronal enhancement, radio emission, and more (G. Basri 2021, and references therein). Among the consequences are flux variations spanning timescales of minutes to decades that manifest across a range of wavelengths.

Investigating this magnetic behavior is critical for understanding the potential habitability of any exoplanets orbiting these stars. M dwarfs are likely candidates for hosting detectable Earth-like exoplanets (K. Ment & D. Charbonneau 2023), upon which the incident stellar flux directly influences

atmospheric and surface conditions. The high activity levels of M dwarfs may have dangerous consequences for habitability (J. C. Tarter et al. 2007; A. L. Shields et al. 2016), or may be advantageous in the drive for prebiotic chemistry and evolution of any lifeforms on planetary surfaces (S. Ranjan et al. 2017). Regardless, there is interest in studying the poorly understood dynamos of FC M dwarfs (D. Shulyak et al. 2015), as they allow for an exploration of dynamo theory in a new regime for comparison to the solar magnetic dynamo. The final motivation we posit is the most fundamental: that of understanding the astrophysical behavior of the most abundant stars in the Universe.

Together, these factors generate the desire for reliable predictions of the evolving stellar activity throughout the lives of M dwarfs. Fully assessing their activity is intrinsically tied to understanding the spindown process for these stars as well, because rotation drives activity through the stellar dynamo. However, work by E. R. Newton et al. (2016, 2018) uncovered a strong bimodality in the observed rotation periods of FC M dwarfs, with W.-C. Jao et al. (2023; hereafter J23) finding significantly higher historical magnetic braking strengths in the most-massive FC M dwarfs compared to PC stars and lower-mass FC stars. The bimodality is likely caused at least in part by a poorly understood temporary phase of very rapid spindown in these FC stars’ lifetimes, with the mass-dependent

age of onset being variable across stars and likely linked to the initial rotation period and evolution of the magnetic field morphology (C. Garraffo et al. 2018; E. K. Pass et al. 2022, 2023a; A. Sarkar et al. 2023; E. K. Pass et al. 2024, and references therein; E. K. Pass et al. 2024 is hereafter referred to as P24).

Rotational evolution presumably drives activity evolution but, somewhat surprisingly, significant activity level differences have been observed for otherwise nearly identical M dwarfs. For example, the two components in the BL+UV Ceti binary system (GJ 65 AB) have virtually identical masses ($A = 0.120 \pm 0.003 M_{\odot}$, $B = 0.117 \pm 0.003 M_{\odot}$; G. F. Benedict et al. 2016) and rotation periods ($A = 0.24$ day, $B = 0.23$ day; J. R. Barnes et al. 2017), and are presumably of the same age. However, they display incongruous starspot distributions (J. R. Barnes et al. 2017), markedly different magnetic field strengths and topologies (O. Kochukhov & A. Lavail 2017), mismatched X-ray variability (M. Audard et al. 2003), and different levels of radio emission (M. Audard et al. 2003; K. Plant et al. 2024, and references therein). The difference in X-ray variability was recently observed to have possibly normalized to roughly similar activity levels compared to 18 yr earlier (S. Wolk et al. 2022), while the radio differences have persisted over several decades. Radio emission differences have also been found between the similar M dwarf components in Ross 867-8 (L. H. Quiroga-Nuñez et al. 2020). In addition, H. C. Gunning et al. (2014) found marked differences in chromospheric $H\alpha$ activity between near-equal-mass components in several M dwarf wide binaries, although rotation periods were unavailable, thereby limiting a fully contextualized interpretation of their results.

Beyond wide binaries, similar behavior has also been observed for M dwarfs in young open clusters. For example, in T. J. Henry & W.-C. Jao (2024), we examined plots of rotation period versus M_G (a better tracer of mass than color) for M dwarfs in clusters spanning ages of 10–750 Myr using results from M. Popinchalk et al. (2021) and references therein, highlighting that stars in the same cluster (i.e., same age and metallicity) at similar M_G (i.e., similar mass) can show pronounced spread in rotation periods around transition regions from fast to slow rotators. This behavior can be seen in stellar activity for cluster M dwarfs as well in the $H\alpha$ comparisons of M. Popinchalk et al. (2021) based on values from S. T. Douglas et al. (2014), E. R. Newton et al. (2017), and R. Kiman et al. (2021). This activity and rotation scatter appears most strongly when initial formative rotation periods are still a relevant factor and around regions of strong spindown. While very-low-mass late-type M dwarfs are often more sparsely covered in existing cluster results, the general behavior remains that some M dwarfs of similar fundamental parameters can display quite varied activity and rotation behaviors.

A dynamo bistability has been proposed to explain some of the magnetic mismatches in late-type M dwarfs, where two distinct dynamo states could emerge from similar initial fundamental stellar parameters (T. Gastine et al. 2013). Other efforts have instead implicated long-term stellar cycles with dynamically changing magnetic structures to explain some magnetic mismatches in various mass and rotation regimes (L. L. Kitchatinov et al. 2014; A. O. Farrish et al. 2021). Fundamental spindown properties are a culprit as well (E. K. Pass et al. 2024). Altogether, the cases of observed activity differences in otherwise similar M dwarfs remain

inadequately understood, indicating that work remains to be done to improve any predictions about their magnetic attributes and consequent effects on orbiting exoplanets. In particular, the strong mass dependence of M dwarf spindown timescales, the metallicity sensitivity of M dwarfs, and their varied interior structures, all suggest that any stars being compared for activity and/or rotation differences need to have very tight constraints for matching their fundamental parameters. This would thus truly constrain how different M dwarfs can be in activity and rotation even if stars are otherwise nearly identical, and probes if the underlying origins of these differences are only from mass/age/composition or if other aspects, such as formation or dynamo factors, may be involved.

To this end, and to improve our understanding of M dwarf magnetism and rotation, here we report first results from our investigation of a sample of 36 “twin” M dwarf wide binaries under the aegis of the REsearch Consortium On Nearby Stars (RECONS; www.recons.org). For each of the pairs, we seek to determine if the twin components show the same or meaningfully different magnetic properties and rotation. Any observed mismatches in the rotation periods between twin stars could imply stochasticity and set constraints on the spindown process, while differences in activity for otherwise similarly rotating twin stars sets constraints on the potential intrinsic scatter in magnetic activity for even equal-mass/age/composition/rotation stars. Of particular note is the understudied long-term years-to-decades variability, where out-of-phase stellar magnetic cycles may be the cause of some activity differences at a given epoch of observation.

Results from this twin study will be split into a two-paper series. This first effort outlines our overall methodology while focusing on a subset of four intriguing sets of twins for which a variety of observations have revealed activity differences. A second forthcoming paper will then discuss the remaining 32 twin systems and overall results for our cumulative sample (A. A. Couperus et al. 2024, in preparation).

This first paper is split into seven further Sections: Section 2 outlines our sample, followed by details of each observing campaign in Section 3. In Sections 4 and 5 we present our results, and we give additional notes on the systems in Section 6. We then discuss the results in Section 7 and summarize the key insights in Section 8. Additional materials are provided in the Appendix.

2. Sample

The RECONS Twins sample was constructed by searching Gaia DR2 (Gaia Collaboration et al. 2018) for common proper-motion wide binaries with nearly identical components. First, we extracted M stars within 50 pc by selecting for $\text{parallax} > 20 \text{ mas}$ and $\text{BP} - \text{RP} > 2.0$. We then selected source pairs with angular separations of $4'' - 300''$, which allows sources to be resolved in many observing programs while still close enough to fit within typical detector fields of view. Pairs with components having BP, RP, or 2MASS J , H , or K_s differing by $> 0.10 \text{ mag}$ were then removed in order to select only “twin” stars with nearly identical magnitudes across the optical and near-IR wavelengths, where M dwarfs emit most of their light. Finally, we removed pairs whose component parallax distances differed by more than 1 pc. No additional criteria such as parallax error cutoffs or proper-motion matches were needed (pairs all have proper-motion components matching within a few mas yr^{-1}). This yielded an all-sky

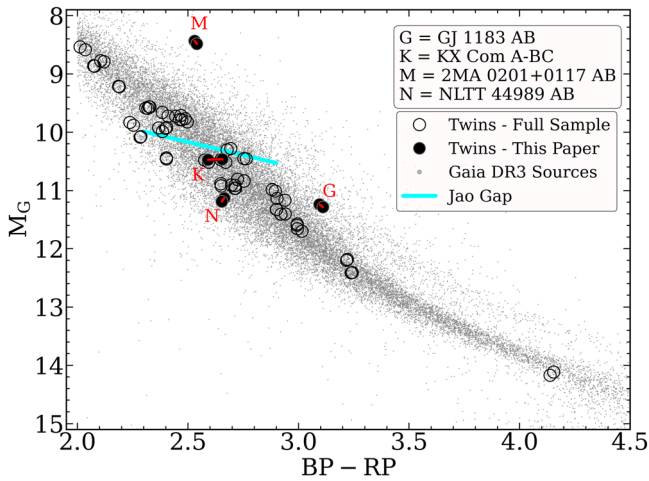


Figure 1. An observational Hertzsprung–Russell Diagram using Gaia DR3 magnitudes and parallaxes. Gray points show a sample of Gaia sources within 50 pc to illustrate the main sequence. Large black circles indicate stars in our sample of 36 M dwarf twin binary pairs. The four systems examined in this paper are filled in and labeled, with red lines connecting the two components in those pairs. A diagonal cyan line represents the gap marking the transition between partially and fully convective M dwarfs near $\sim 0.35M_{\odot}$ (W.-C. Jao et al. 2018, 2023), offset downward by 0.05 mag to approximately match the middle of the gap instead of the upper edge.

sample of 36 M dwarf twin binaries that are still astrometrically associated and pass these same cuts in updated Gaia DR3 data (Gaia Collaboration et al. 2022). To further confirm the binary nature of our stars, we crossmatched with the SUPERWIDE catalog of Z. D. Hartman & S. Lépine (2020), finding all four systems considered here to be real wide binaries at $>99.99\%$ probability.

The four systems we highlight in this current publication are GJ 1183 AB, KX Com A-BC, 2MA 0201+0117 AB, and NLTT 44989 AB, chosen for their standout activity behaviors among our sample and their inclusion in the Chandra X-ray study detailed here. “KX Com” nominally refers to what we call our A component, and we added the name association to what we call our B component and its subsequently discovered C companion discussed later in Sections 4.3.2 and 6.2. The designation NLTT 44989 specifically refers to A, while B is NLTT 44988, but we refer to them as NLTT 44989 A and B for clarity throughout this paper; this system also goes by the name LP 920-61 AB. A and B labels were decided following some existing catalog component names (GJ 1183 A and B), but were otherwise chosen by DR2 BP brightness. The A or B distinction is somewhat arbitrary for these twin stars because different measurements or catalogs will often flip-flop between which is the brighter A star, so precise coordinates may prove more useful for the interested investigator.

The twin binaries are shown on an observational Hertzsprung–Russell Diagram in Figure 1, where the four systems of interest for this paper are highlighted with solid points connected by short red lines. As expected, this Figure confirms that no binary giants were mistakenly captured in our search. The significantly elevated pair is 2MA 0201+0117 AB, a member of the young 25 Myr β Pictoris association (F. J. Alonso-Floriano et al. 2015; S. Messina et al. 2017a); the other slightly elevated system is GJ 1183 AB. All components in the four systems targeted here are fully convective stars—three systems are below the partially/fully convective transition gap of W.-C. Jao et al. (2018), indicated with the diagonal cyan line, whereas

2MA 0201+0117 AB has been functionally fully convective throughout its brief life because it is a pre-main-sequence (PMS) system. We also note that none of the four systems—except KX Com A-BC, a non-twin triple—land within the activity dip sub-gap region identified in J23 between $M_G = 10.3$ – 10.8 .

Astrometric and photometric parameters for the four systems targeted in this paper are given in Tables 1 and 2, respectively. All data in Table 1 are from Gaia DR3, as well as the derived M_G values, G , BP, and RP in Table 2. JHK_s values are from 2MASS. The key values have average errors as follows: $\pi \pm 0.03$ mas, $G \pm 0.003$ mag, $BP \pm 0.007$ mag, $RP \pm 0.005$ mag, $J \pm 0.028$ mag, $H \pm 0.035$ mag, and $K_s \pm 0.028$ mag. Tables are ordered alphabetically by star name, where “2MA” counts as M. The projected separations are greater than 80 au for all four wide systems, implying orbital periods $\gtrsim 1000$ yr at their low masses, significantly longer than the ~ 100 days limit on tidal interaction and locking predicted by D. P. Fleming et al. (2019)—we thus conclude that present-day stellar tidal interactions between these wide pairs are negligible.

For context, estimated masses are given in Table 2, derived from the V -band mass–luminosity relation (MLR) for M dwarfs in G. F. Benedict et al. (2016) via a prescription similar to that described in E. Vrijmoet (2023). Briefly, several hundred M dwarfs on the RECONS long-term 0.9 m program (T. J. Henry et al. 2018) with measured M_V were used with the V -band MLR to estimate their masses. We then correlated these masses with the stars’ Gaia DR2 M_{BP} values, and fit that relation with a high-order polynomial, which was then used to estimate masses for our twin stars via their Gaia DR2 M_{BP} values. Masses are shown in parentheses for the unresolved KX Com BC component, as well as 2MA 0201+0117 A and B, for the latter pair because they are PMS stars and therefore provide upper-limit mass estimates at best. Regardless of the exact mass estimation method, our magnitude criteria are ultimately the fundamental observables that select our pairs to be twins in mass; we presume they host functionally identical ages, compositions, and environments as well under the assumption the binary components formed together and are co-eval.

We also employed the BANYAN Σ tool of J. Gagné et al. (2018), which uses a Bayesian analysis to probabilistically determine a target’s candidate membership in nearby young stellar associations based on inputs optionally combining astrometry, radial velocities (RVs), or photometric distance constraints. We utilized Gaia DR3 astrometry and ran the analysis both with and without our weighted mean CHIRON RVs (Section 4.3) given the binary nature of our targets. The results indicate GJ 1183 A has a 13% chance of membership in the young Carina-Near association, but only for the A component and only when excluding RVs—this low probability, combined with the low number of 13 stars used to define the group in BANYAN Σ , leads us to disregard the possible membership. The results do correctly support 2MA 0201+0117 AB belonging to the β Pictoris association, and otherwise find no membership probabilities $>2\%$ for the other stars considered here.

2.1. Higher-order Multiplicity Checks

Our intended comparisons between binary components require the stars be true twins, so it is crucial to search for any higher-order companions—especially unresolved ones—that could disrupt the components’ twin natures. Three Gaia parameters were assessed to check for unresolved companions

Table 1
Four Twin Systems Explored in This Paper—Astrometry

Name	R.A. [ICRS-2016]	Decl. [ICRS-2016]	π (mas)	μ_α (mas yr ⁻¹)	μ_δ (mas yr ⁻¹)	Ang. Sep. (arcsec)	2D Sep. (au)	RUWE	RV _{Gaia} (km s ⁻¹)	IPDfmp (%)
GJ 1183 A	14 27 55.69	-00 22 30.5	57.01	-361.15	41.70	13.07	229.3	1.510	-11.72 ± 3.27	0
GJ 1183 B	14 27 56.01	-00 22 18.3	57.03	-363.17	52.54			1.524	...	0
KX Com A	12 56 52.80	+23 29 50.7	36.61	70.27	4.10	7.72	211.2	1.234	-7.89 ± 0.84	0
KX Com BC	12 56 52.24	+23 29 50.2	36.52	74.89	8.56			1.436	-10.81 ± 4.90	0
2MA 0201+0117 A	02 01 47.00	+01 17 05.1	20.30	74.77	-49.21	10.45	514.7	1.404	5.18 ± 0.95	0
2MA 0201+0117 B	02 01 46.85	+01 17 15.3	20.31	75.86	-46.73			1.501	5.99 ± 2.84	1
NLTT 44989 A	17 33 05.98	-30 35 10.1	54.68	-113.37	-123.01	4.75	86.9	1.001	40.09 ± 0.68	0
NLTT 44989 B	17 33 05.62	-30 35 11.3	54.61	-121.23	-122.86			1.167	44.42 ± 1.16	39

Note. All astrometric information is from Gaia DR3. Physical separations are from 2D projections on the sky assuming an average of the two component distances. Separations for KX Com refer to A-BC, not B-C. GJ 1183 B has no RV available in DR3. See Section 2.1 for a discussion of RUWE, RV_{Gaia}, and IPDfmp.

Table 2
Four Twin Systems Explored in This Paper—Photometry and Mass Estimates

Name	G (mag)	BP (mag)	RP (mag)	J (mag)	H (mag)	K_s (mag)	M_G (mag)	Mass (M_\odot)
GJ 1183 A	12.46	14.27	11.17	9.31	8.70	8.40	11.24	0.21
GJ 1183 B	12.50	14.33	11.22	9.35	8.76	8.46	11.28	0.21
KX Com A	12.66	14.07	11.48	9.86	9.33	9.09	10.47	0.32
KX Com BC	12.65	14.12	11.46	9.83	9.29	9.04	10.47	(0.32)
2MA 0201+0117 A	11.90	13.26	10.73	9.10	8.46	8.26	8.44	(0.54)
2MA 0201+0117 B	11.95	13.33	10.79	9.15	8.53	8.27	8.49	(0.53)
NLTT 44989 A	12.44	13.91	11.25	9.61	9.06	8.80	11.13	0.25
NLTT 44989 B	12.50	13.93	11.28	9.61	9.03	8.78	11.19	0.25

Note. Mass estimates are derived from the G. F. Benedict et al. (2016) mass–luminosity relation (MLR) for main-sequence M dwarfs; values in parentheses are less reliable or unreliable estimates, as discussed in Section 2. Gaia G , M_G , BP, and RP magnitudes reported here are from DR3, though note our stars were originally selected using DR2 information. JHK_s magnitudes are from 2MASS (M. F. Skrutskie et al. 2006).

and are included in Table 1. First is the renormalized unit weight error (RUWE; L. Lindegren 2018; L. Lindegren et al. 2021), where an elevated value may indicate an unresolved component. Ongoing RECONS work by M. R. LeBlanc et al. (2024, in preparation) on the nearest ~ 3000 M dwarf systems finds that $\text{RUWE} > 1.7$ indicates an unseen companion, in line with the results of E. H. Vrijmoet et al. (2020), which compared RECONS data to Gaia DR2.⁷ All eight components considered here have $\text{RUWE} < 1.7$, implying no companions that affect the astrometry over the 34 months timescale of the DR3 data. The second parameter is the error on RV_{Gaia} , where all are generally less than $\sim 3 \text{ km s}^{-1}$, appropriate for single stars with these magnitudes. Note, however, that KX Com B has an RV_{Gaia} error value of nearly 5 km s^{-1} , implying a companion, which is in fact the case (see Sections 4.3.2 and 6.2).

The third Gaia parameter, `ipd_frac_multi_peak` (IPDfmp), reports the fraction of Gaia windows of the source for which a double peak is identified, possibly indicating an unresolved companion or contaminating source. For context, A. Tokovinin (2023) demonstrated that source pairs closer than $\sim 2''.5$ can generally display elevated IPDfmp values just due to proximity and not unseen bound companions. The components considered here all have $\text{IPDfmp} \leq 1\%$, consistent with no

unresolved sources, except NLTT 44989 B at 39% presumably because of a very nearby Gaia source $0''.84$ away at the DR3 2016.0 epoch ($0''.22$ away at $\text{Ep} = 2021.0$).⁸ Our careful examination of archival DSS (B. M. Lasker et al. 1996; R. R. Gal et al. 2004) and VPHAS (J. E. Drew et al. 2014) images and Gaia astrometry clearly shows this very nearby source—along with a second nearby source $3''.23$ away from B ($3''.02$ away at $\text{Ep} = 2021.0$)—are both physically unassociated fainter background stars that NLTT 44989 AB has approached over time via proper motion. These two contaminating sources are discussed further in Section 3.6.

Our stars were searched for inclusion in the VizieR collection of Gaia DR3 non-single stars catalogs (Gaia Collaboration 2022), which report various assessments indicating likely unresolved multiples, but no matches were found. We also searched Gaia DR3 for any potential additional wide companions within a 2D projected separation of 10,000 au around each of our eight components, finding no sources in this radius with parallaxes within 10 mas of each associated twin star’s parallax. A crossmatch found none of our components are present in the SB9 spectroscopic binary catalog as well (D. Pourbaix et al. 2004). Finally, the four systems were matched against the Washington Double Star Catalog (B. D. Mason et al. 2001), where the only result of note was the entry of a supposed additional “C” component for NLTT 44989 AB. A careful investigation reveals this extra

⁷ While conventional criteria often use $\text{RUWE} > 1.4$ (e.g., L. Lindegren 2018; K. G. Stassun & G. Torres 2021), we adopt a more conservative RUWE limit of 1.7 because our research finds this to be a more appropriate cutoff for true M dwarf binaries in the solar neighborhood (E. H. Vrijmoet et al. 2020, M. R. LeBlanc et al. 2024, in preparation).

⁸ We often use the notation “Ep = year” throughout this paper to designation the Julian epoch of coordinates used to derive an angular separation value at a certain point in time.

“C” source to be the aforementioned unassociated background star $3''.23$ away from B, so it is not a real companion.

3. Observations and Data Processing

Our twin targets have been observed with five observing campaigns: (1) long-term optical photometry with the CTIO/SMARTS 0.9 m spanning several years to probe for stellar activity cycles, (2) short-term optical photometry with the CTIO/SMARTS 0.9 m to capture rotation—our rotation period determinations are also supported by archival data from TESS (G. R. Ricker et al. 2015), ZTF (E. C. Bellm et al. 2019), and ASAS-SN (B. Shappee et al. 2014; T. Jayasinghe et al. 2019a), (3) multiepoch high-resolution optical spectroscopy using the CHIRON echelle spectrograph on the CTIO/SMARTS 1.5 m to determine RVs and $H\alpha$ equivalent widths (EWs), (4) Chandra X-ray imaging observations to determine X-ray luminosities and coronal parameters, and (5) speckle imaging with HRCam on the SOAR 4.1 m and QWSSI on the LDT 4.3 m to search for hidden companions. We outline the methodology for each of these five observing campaigns in the following subsections: long-term photometry in Section 3.1, rotation in Section 3.2, optical spectroscopy in Section 3.3, X-rays in Section 3.4, speckle in Section 3.5, and a subsequent cumulative discussion about contamination in Section 3.6.

3.1. Stellar Cycles—CTIO/SMARTS 0.9 m Long-term Campaign

The CTIO/SMARTS 0.9 m has been used to observe nearby M dwarfs as part of an ongoing RECONS long-term monitoring program since 1999 (see T. J. Henry et al. 2018 for a recent summary). Past work has used the multidecade photometry to investigate stellar variability (W.-C. Jao et al. 2011; A. D. Hosey et al. 2015; T. D. Clements et al. 2017; A. Kar et al. 2024), with an ongoing project to reveal stellar activity cycles (A. A. Couperus et al. 2024, in preparation). GJ 1183 AB had fortuitously already been on the program since 2013; 2MA 0201+0117 AB and NLTT 44989 AB were added to the long-term program in 2019; and KX Com A-BC was added in 2021. KX Com A-BC is the only case we do not report long-term variability results for here, as the system still has insufficient coverage to be informative for long-term cycles.

Details of the differential photometry reduction and analysis procedures for the 0.9 m long-term program are described in W.-C. Jao et al. (2011) and A. D. Hosey et al. (2015). To summarize, each target typically receives two visits per year with five frames taken per visit using the same optical V , R , or I filter and positioned consistently in the $6''.8$ square field to provide a set of 5–15 reference stars to be used as differential photometry calibrators. Measurements are made with SExtractor (E. Bertin & S. Arnouts 1996), specifically using the MAG_WIN parameter; this routine obtains instrumental magnitudes by summing the source pixel counts falling within a circular Gaussian window function that is scaled to the light distribution of each source. Following the methodology of R. K. Honeycutt (1992), the instrumental magnitudes of all reference stars in all frames are simultaneously minimized from their individual mean brightnesses to yield corrective offsets for each frame due to changes in atmospheric transmission, instrumental efficiency, and exposure time. Any photometrically variable reference stars are identified by eye and removed to ensure that only constant calibrator stars are used. The

offsets are then applied to the target science star magnitudes, giving the final relative light curve.

Results from the long-term program are discussed later in Section 4.1.

3.2. Rotation—CTIO/SMARTS 0.9 m, TESS, ZTF, and ASAS-SN

Archival data alone did not provide reliable periods identifiable for each star in a system in most cases, either because of blending or due to no rotation signal being evident in one component or the other. This situation motivated collecting our own observations with the 0.9 m, as that telescope system can outperform the archival sources in vital ways. For example, the noise floor for the 0.9 m is typically ~ 7 mmag (W.-C. Jao et al. 2011; A. D. Hosey et al. 2015), with the key advantage of high resolution with a $401 \text{ mas pixel}^{-1}$ plate scale, which is the best of the four data sources utilized here. This is markedly better than for ZTF with ~ 10 – 20 mmag precision at $r = 14$ – 17 and $1''.01$ pixels (F. J. Masci et al. 2019), or ASAS-SN with ~ 15 – 25 mmag at $V = 13$ – 14 with $8''.0$ pixels (T. Jayasinghe et al. 2019a). Whereas TESS provides exquisite precision for the photometry, its $21''$ pixels mean that all four of our systems are blended in TESS measurements, thereby still requiring 0.9 m measurements to assign rotations periods to individual components. For 2MA 0201+0117 AB, ZTF data were able to determine reliable periods for each star independently, but we still observed this system with the 0.9 m to validate our rotation methodology.

The 0.9 m observations targeting our twins’ stellar rotation periods were carried out using NOIRLab time (ID 2023A-549259; PI Couperus). Observing cadences were tailored to each system based on likely or possible periods indicated by their $H\alpha$ activity and the archival data from TESS, ZTF, or ASAS-SN. At the 0.9 m, we made ~ 50 – 70 visits to each target during two separate 20-night observing runs, with a few additional visits during adjacent long-term program (Section 3.1) runs to extend baselines and coverage for GJ 1183 AB and NLTT 44989 AB. At each visit, we routinely acquired four images with both components falling in a single detector field of view. Observations for all systems were made in the V filter to provide enhanced spot contrast (A. D. Hosey et al. 2015) and to balance the brightnesses of the targets and reference stars. The light curves from the 0.9 m rotation effort were derived following the same procedures as the long-term RECONS program (Section 3.1).

For TESS, we extracted Pre-search Data Conditioning Simple Aperture Photometry (PDCSAP) light curves using 20 s (20s) and 2 minutes (2m) high-cadence data as well as 10 minutes (10m) and 30 minutes (30m) full frame image (FFI) data, provided by the TESS-SPOC pipeline (J. M. Jenkins et al. 2016; D. A. Caldwell et al. 2020). We used all available data products from all available TESS sectors for each of our targets as follows: GJ 1183 AB has 2 m and 10 m data from sector 51, KX Com A-BC has a mix of 20s/2m/10m/30m data from sectors 23/49, 2MA 0201+0117 AB has a mix of 20s/2m/10m/30m data from sectors 4/42/43, and NLTT 44989 AB has a mix of 2m/10m/30m data from sectors 12/39.

In addition to the standard TESS results, we also generated FFI light curves with the unpopular package of S. Hattori et al. (2022). This approach uses an alternative causal pixel model method that corrects for systematics by modeling trends common across many different sources in the field. A key facet of unpopular is the optional inclusion of a polynomial

component that is simultaneously fit during this detrending process to better capture and preserve long-term astrophysical variations—such as rotation signals with periods beyond half a TESS sector baseline (~ 13.5 days)—thereby allowing us to search for longer-duration signals in TESS. We followed the approach outlined in A. Kar et al. (2024), where the polynomial component and any resulting long-term signal are only used and deemed reliable if the raw simple aperture photometry (SAP) TESS flux also shows a long-term signal. A long-term signal appearing in multiple sectors further validates a detection. Apertures used with `unpopular` were manually selected rectangles chosen to closely match the default TESS pipeline apertures while minimizing blending and contamination where possible. The same sectors of data were used with `unpopular` for each target as noted above for the normal TESS products.

Beyond the 0.9 m and TESS, two other sources of rotation data were utilized. ZTF PSF-fit light curves were obtained from Data Release 18 via the IPAC/Caltech system (F. J. Masci et al. 2019), using *zr* and *zg* filter data separately, with measurements from different ZTF fields and CCDs but for the same star all combined into a single light curve in each filter. ASAS-SN pre-computed light curves in the *V* band were extracted via the photometry page⁹ (T. Jayasinghe et al. 2019a), or new *V*-band and *g*-band aperture photometry curves were generated with all cameras merged using the ASAS-SN Sky Patrol resource¹⁰ if the aforementioned pre-computed data were unavailable (C. S. Kochanek et al. 2017). No light curves or rotation data were available from Gaia DR3 (L. Eyer et al. 2023), Kepler (W. J. Borucki et al. 2010), K2 (S. B. Howell et al. 2014), or MEarth (Z. K. Berta et al. 2012) for the four systems discussed here, and a literature review found no other rotation results not already surpassed in quality by the 0.9 m or archival sources.

To search for and measure rotation periods, we first addressed flares and outliers as follows. Any obviously strong flares in the 0.9 m data were manually excluded. We removed poor-quality measurements from the archival data (TESS-SPOC, TESS-unpopular, ZTF, and ASAS-SN) using provided quality flags if available, along with removal of any outlier points greater than 3σ from the mean. Note that ASAS-SN Sky Patrol curves had stricter cuts for points at $>2\sigma$ and >50 mmag error owing to less curated starting data. For archival data sets, points indicating lingering mild flares not removed by our outlier cut were left untouched as we found the separate archival sources gave extremely congruent period measurements regardless.

Each light curve was inspected visually and analyzed with the generalized Lomb–Scargle periodogram (N. R. Lomb 1976; J. D. Scargle 1982; M. Zechmeister & M. Kürster 2009) using the Astropy implementation (Astropy Collaboration et al. 2013, 2018). Periodograms used 100,000 samples evenly spaced in frequency between 0.05 and 300 days. False-alarm probabilities (FAPs) were computed using the approximate upper-limit Baluev method (R. V. Baluev 2008). The maximum power peak and its corresponding FAP value, $2/3/4$ harmonic multiples, $n = -3$ to $+3$ one-day aliases (for ground-based observatories), and relative FAP lines were all considered in the determination of periods for each case. FAP

values were de-emphasized in these reviews, and our manual assessment instead relied more on criteria such as the photometric amplitude of a signal relative to the noise level of the data itself, the visual robustness of candidate periods in raw and phase-folded light curves, a signal repeating over time or not, the periodogram power of a peak relative to the power of noise peaks, and the reoccurrence of trends in multiple independent data sources. That said, very small FAP values routinely accompanied our final choices. We point the interested reader to J. T. VanderPlas (2018) for a discussion of the subtleties involved with interpreting FAP values.

The final rotation period chosen for each star was determined through a comprehensive review of all available light curves from the various sources outlined above, in conjunction with knowledge about the different amounts of blending, contamination, and photometric precision between the data sources. For example, our resolved 0.9 m data might confidently suggest period *X* in star A but only gives a weak uncertain detection of period *Y* in star B, while blended TESS data shows a combined signal of two robust periods also near *X* and *Y*, allowing us to confidently assess that the *Y* period is legitimate and belongs to star B. Either data set alone may be inconclusive, but combined they confirm a period exists and to which star it belongs. The mix of data sources also allows us to better vet 1 day sampling alias peaks in ground-based data by comparing to space-based data without such aliases. Generally, our resolved 0.9 m results were able to either outright confirm or give indications toward a specific period in each star, with external blended data providing confirmation that such periods exist within the system as a whole to validate a weaker 0.9 m detection. Note that we did not attempt to combine separate data sources into merged light curves or a global simultaneous analysis given the significantly different precision, systematics, cadences, filters, reduction procedures, timescales, blending, and contamination present across the many archival sources used individually here.

Results from the rotation analysis are discussed later in Section 4.2.

3.3. $H\alpha$ Equivalent Widths and Radial Velocities—CTIO/SMARTS 1.5 m and CHIRON

Optical spectra were obtained at the CTIO/SMARTS 1.5 m with the CHIRON echelle spectrograph (A. Tokovinin et al. 2013; L. A. Paredes et al. 2021). Each of the four systems were observed at least five times spread over several months to determine $H\alpha$ EWs and RVs, with an additional sequence of five visits 5 nights in a row to search for close, potentially interacting unresolved companions via changes in RVs. For KX Com A and B, only three of the five nightly sequence visits were secured due to poor weather. After preliminary RV analyses found a likely unresolved companion to KX Com B (the C component), we obtained another 23 single-spectrum visits on just B over 1 month to confirm or refute the companion. NLTT 44989 AB also received several additional visits to extend the time baseline beyond 1 yr in order to further rule out any companion with an orbital period up to a few years.

Spectra were taken in fiber mode with 4×4 binning, yielding $R \approx 27,000$. Components were well resolved given the $2''7$ diameter fiber (see Section 3.6 for additional contamination details). A typical visit consisted of four total exposures, two on each binary component, along with ThAr wavelength calibration images at each pointing. For each system, spectra on

⁹ Available at <https://asas-sn.osu.edu/photometry>.

¹⁰ Available at <https://asas-sn.osu.edu/>.

each component were secured back-to-back, not at disjointed times from each other, so that our A-B comparisons are robust at consistent snapshots in time. Exposure times of 900–1800 s were used, and the two spectra at a given epoch were combined to yield a typical continuum signal-to-noise ratio (SNR)¹¹ of ~ 27 .

Reduced data were received from the CHIRON pipeline as described in L. A. Paredes et al. (2021). The process includes routine bias and flat corrections, order extraction, and wavelength calibration using time-adjacent ThAr frames. We manually reviewed each spectrum to remove any cases with critical observing failures or strong cosmic rays on or near H α . Spectra were then further processed using the procedures and code of J23, who used the same CHIRON configuration as our work and also targeted H α and RVs in M dwarfs. Briefly, the two back-to-back spectra in a single star’s visit were barycenter corrected following J. T. Wright & J. D. Eastman (2014), combined to a mean spectrum to boost the SNR, blaze function normalized, and trimmed for cosmic rays along the way. RV and $v \sin(i)$ values were obtained via cross-correlation with two mid-M standard stars, specifically Barnard’s star and GJ 273, using 6 echelle orders and following the methodology of J. M. Irwin et al. (2018) and A. H. Nisak et al. (2022; see J23 for details). Each standard star gives six measures from the 6 respective orders, yielding a mean and standard deviation of the RV, as well as $v \sin(i)$. A weighted average of the two standard star results then gives our final RV and $v \sin(i)$ for that target star at that epoch.

Our H α EWs also follow the process outlined in J23. Spectra were shifted to rest-frame using the stellar RVs and manually reviewed to define three wavelength windows, one centered on the H α feature and two on either side to capture the mean continuum level. Our default regions for absorption cases are as given in Figure 2 and Table 2 of J23. In emission cases, the H α region was adjusted in width to capture line wings based on visual inspection using the template of J23. If an H α wing came close to or overlapped the default continuum regions, we shifted both continuum regions outward slightly to consistent “wide” positions designed to yield nearly the same mean continuum level as the default positions in order to avoid systematic offsets. Some poor SNR cases also used slightly wider continuum regions to better estimate the mean continuum levels. To avoid biasing our resulting measures and comparisons, specific care was taken to be as consistent as possible when defining all regions for two components in the same twin binary.

Our EWs are measured following Equation (1) of J23, and we adopt the convention of negative EWs indicating H α emission. The EW uncertainties follow the procedure in R. Cayrel (1988) and use a Gaussian fit to H α to estimate the needed FWHM. We note that a handful of spectra with weak (often double-peaked) emission near the continuum were fit with overly wide Gaussians, inflating the EW uncertainties from the typical $\sim 0.02 \text{ \AA}$ up to falsely larger values near $\sim 0.10 \text{ \AA}$ —this has no meaningful impact on our results.

Results from the CHIRON spectral analysis are discussed later in Section 4.3.

¹¹ Our reported SNRs are the mean SNRs per pixel across both continuum regions using the per-pixel method in Equation (1) of A. Tokovinin et al. (2013).

3.4. X-Rays—Chandra Observatory

To evaluate the coronal behavior of the target stars, we obtained observations with the Chandra X-ray Observatory for our four systems from 2020–2022 through the GO proposal “Fraternal or Identical? The Magnetic Properties of M Dwarf Twins” (ID 22200260; PI Osten). The spatially resolved ACIS-S imaging study resulted in eight exposures across the four systems—three each for GJ 1183 AB and KX Com A-BC and one each for 2MA 0201+0117 AB and NLTT 44989 AB. The cases with multiple exposures are noted as TARGET-1, TARGET-2, etc., and all are outlined in Table 3. These observations allow us to produce X-ray light curves and nongrating spectra for subsequent analysis. Data were analyzed using the Chandra Interactive Analysis of Observations (CIAO) software package v4.14.3 and CALDB v4.9.8 (A. Fruscione et al. 2006), with `chandra_repro` used to apply the corresponding calibrations. Spectral fitting was carried out using the Sherpa package within CIAO (P. Freeman et al. 2001).

Nonoverlapping circular apertures were manually constructed for the A and B components in each observation, placed at corresponding source locations determined by the CIAO `wavdetect` algorithm. Source aperture radii were chosen based on the manual inspection of radial plots for each source, with selected radii of 3–6 pixels depending on the extent of each source’s photon signals. Background apertures were ~ 50 pixel radius circles encompassing the components, with enlarged regions excluded around each source to ensure the removal of all source photons. In a single case, NLTT 44989 A, we did not obtain a confident detection at the expected source location, the handling of which is detailed further in Section 3.4.1.

For each source, X-ray light curves filtered to 0.3–10 keV, the nominal energy-calibrated range of ACIS, were inspected for noise background flares but none were found. We captured time-resolved stellar flares during four of the eight total exposures. An example light curve for the strongest flare, in this case for NLTT 44989 B, is shown in Figure 2—all other X-ray light curves can be seen in Figure 16 in the Appendix. In these flare cases, data were visually split into flaring and nonflaring time periods and analyzed separately; we report both the quiescent and flaring measurements separately in Table 3.

Nongrating Pulse Height Amplitude (PHA) spectra were extracted for each detected source, background subtracted, and filtered to 0.3–10 keV. We grouped data to 9 counts per bin in all cases for consistency—in spectra with total counts $\lesssim 200$, we tested 6 counts per bin as well, but it did not substantively change our resulting measurements. The X-ray coronal spectra were fit with Astrophysical Plasma Emission Code (APEC) models within Sherpa that parameterize the plasma temperature (kT in keV units), joint coronal abundances relative to solar of 13 atomic species other than hydrogen, redshift (fixed to 0 for our nearby stars), and a normalization parameter tied to the emission measure. We used a forward-folding technique typical for this application that takes into account the instrumental response function and utilized the `chi2xspecvar` reduced- χ^2 statistic. Fits were carefully tested in every case with the Sherpa `levmar` optimizer and `moncar` Markov Chain Monte Carlo optimizer, along with several different initial parameter values, to validate consistent convergence to the final selected solutions.

A model component to account for interstellar medium absorption was tested using hydrogen column density estimates

Table 3
Chandra X-Ray Observations and Results

Data set	ObsID	ObsID-Start (yyyy-mm-dd.d)	Exp. (ks)	Counts (cts)	Pileup (%)	F_X $\times 10^{-14}$ (erg s $^{-1}$ cm $^{-2}$)	L_X $\times 10^{27}$ (erg s $^{-1}$)	T_1 (MK)	VEM_1 $\times 10^{50}$ (cm $^{-3}$)	T_2 (MK)	VEM_2 $\times 10^{50}$ (cm $^{-3}$)	Abund. [rel. solar]	Red.- χ^2
GJ 1183 A-1	24504	2020-12-15.4	14.7	475	2.2	48.8 $^{+3.7}_{-6.1}$	18.0 $^{+1.4}_{-2.2}$	10.91 $^{+0.65}_{-0.65}$	20.1 $^{+4.2}_{-3.5}$	0.159 $^{+0.057}_{-0.046}$	1.00
GJ 1183 A-2	24899	2020-12-15.8	13.3	345	1.7	36.9 $^{+3.2}_{-4.5}$	13.6 $^{+1.2}_{-1.7}$	10.49 $^{+0.66}_{-0.64}$	13.8 $^{+3.6}_{-3.3}$	0.198 $^{+0.101}_{-0.064}$	1.62
GJ 1183 A-3	23392	2022-04-12.4	28.3	994	2.4	59.8 $^{+2.3}_{-2.3}$	22.0 $^{+0.8}_{-0.9}$	11.41 $^{+0.37}_{-0.46}$	23.3 $^{+2.9}_{-2.5}$	0.176 $^{+0.039}_{-0.034}$	1.25
GJ 1183 B-1	24504	2020-12-15.4	14.7	340	1.6	39.6 $^{+3.2}_{-3.7}$	14.6 $^{+1.2}_{-1.4}$	9.21 $^{+0.53}_{-0.53}$	14.1 $^{+3.4}_{-3.1}$	0.216 $^{+0.089}_{-0.061}$	0.87
GJ 1183 B-2	24899	2020-12-15.8	14.9	196	...	23.0 $^{+2.0}_{-1.9}$	8.5 $^{+0.7}_{-0.7}$	8.66 $^{+0.58}_{-0.59}$	7.9 $^{+0.8}_{-0.8}$	[0.216]	1.17
GJ 1183 B-3	23392	2022-04-12.4	28.3	777	1.9	47.3 $^{+2.0}_{-2.1}$	17.4 $^{+0.7}_{-0.8}$	11.41 $^{+0.55}_{-0.82}$	22.2 $^{+3.9}_{-2.4}$	0.105 $^{+0.028}_{-0.029}$	1.10
KX Com A-1	23393	2021-03-15.4	16.4	323	1.4	30.8 $^{+2.3}_{-2.8}$	27.5 $^{+2.1}_{-2.5}$	11.01 $^{+0.75}_{-0.70}$	32.5 $^{+6.5}_{-6.1}$	0.135 $^{+0.060}_{-0.042}$	0.86
KX Com A-2	24991	2021-03-15.8	9.3	140	...	24.6 $^{+2.7}_{-2.7}$	22.0 $^{+2.4}_{-2.4}$	9.64 $^{+0.88}_{-1.04}$	25.8 $^{+3.5}_{-2.9}$	[0.135]	1.12
KX Com A-3	24503	2022-03-22.6	30.2	583	1.3	35.1 $^{+2.1}_{-2.8}$	31.3 $^{+1.9}_{-2.5}$	10.32 $^{+0.56}_{-0.55}$	38.7 $^{+6.3}_{-5.5}$	0.120 $^{+0.036}_{-0.030}$	0.90
KX Com BC-1	23393	2021-03-15.4	14.4	39	...	7.7 $^{+3.9}_{-3.6}$	6.9 $^{+3.5}_{-3.2}$	4.86 $^{+2.17}_{-1.04}$	11.2 $^{+6.5}_{-5.1}$	[0.150]	1.49
KX Com BC-2	24991	2021-03-15.8	16.9	67	...	6.1 $^{+0.9}_{-1.0}$	5.5 $^{+0.8}_{-0.9}$	9.92 $^{+0.93}_{-1.09}$	6.1 $^{+1.0}_{-0.9}$	[0.150]	2.39
KX Com BC-3	24503	2022-03-22.6	30.2	79	...	4.4 $^{+0.5}_{-0.5}$	3.9 $^{+0.4}_{-0.4}$	12.02 $^{+1.38}_{-1.33}$	4.4 $^{+0.5}_{-0.5}$	[0.150]	0.62
2MA 0201+0117 A	23394	2020-10-10.2	13.9	605	...	62.5 $^{+4.2}_{-7.8}$	181.5 $^{+12.2}_{-22.7}$	10.87 $^{+0.59}_{-0.68}$	207.6 $^{+41.8}_{-31.1}$	0.149 $^{+0.046}_{-0.042}$	1.04
2MA 0201+0117 B	23394	2020-10-10.2	13.9	2071	1.7	225.8 $^{+11.1}_{-15.3}$	654.8 $^{+32.3}_{-44.4}$	9.75 $^{+0.71}_{-0.59}$	370.3 $^{+228.8}_{-93.7}$	20.9 $^{+5.5}_{-1.7}$	331 $^{+52}_{-116}$	0.170 $^{+0.062}_{-0.065}$	1.05
NLTT 44989 A	23395	2022-07-28.6	49.8	≤ 4.3	...	≤ 0.2	≤ 0.1	[10.00]	≤ 0.1	[0.200]	...
NLTT 44989 B	23395	2022-07-28.6	42.8	223	...	9.7 $^{+0.9}_{-0.9}$	3.9 $^{+0.4}_{-0.4}$	9.09 $^{+0.64}_{-0.67}$	4.4 $^{+0.5}_{-0.4}$	[0.150]	1.32
GJ 1183 A-2 Flare	24899	2020-12-15.8	1.6	96	4.7	111.8 $^{+15.0}_{-14.9}$	41.2 $^{+5.5}_{-5.5}$	10.10 $^{+1.11}_{-1.14}$	46.2 $^{+7.5}_{-6.5}$	[0.150]	0.57
KX Com A-2 Flare	24991	2021-03-15.8	7.6	327	2.8	69.0 $^{+6.4}_{-10.0}$	61.6 $^{+5.7}_{-8.9}$	6.56 $^{+1.67}_{-2.95}$	35.4 $^{+24.5}_{-11.2}$	18.3 $^{+5.3}_{-2.3}$	39 $^{+11}_{-10}$	[0.150]	1.65
KX Com BC-1 Flare	23393	2021-03-15.4	2.0	43	1.5	34.0 $^{+5.8}_{-5.6}$	30.5 $^{+5.2}_{-5.0}$	12.97 $^{+2.22}_{-1.88}$	34.6 $^{+5.8}_{-5.7}$	[0.150]	0.71
NLTT 44989 B Flare	23395	2022-07-28.6	7.1	252	2.3	52.3 $^{+4.2}_{-5.1}$	21.0 $^{+1.7}_{-2.0}$	13.94 $^{+1.74}_{-1.22}$	27.4 $^{+5.3}_{-5.2}$	0.092 $^{+0.074}_{-0.044}$	1.60

Note. Exposure times are what is left after separating the stellar flare segments, where relevant. Counts are for 0.3–10 keV after background subtraction. Cases with a reported pileup fraction used a pileup component in their spectral modeling while those without a reported value did not. Values in square brackets were fixed in the coronal models. The uncertainties are all 1σ (68% confidence interval) values (see Sections 3.4 and 4.4 for details). NLTT 44989 A was a weak detection or nondetection, with values provided here indicating estimated upper limits only (see Section 3.4.1 for details). All of the Chandra observations here are available in doi:10.25574/cdc.305.

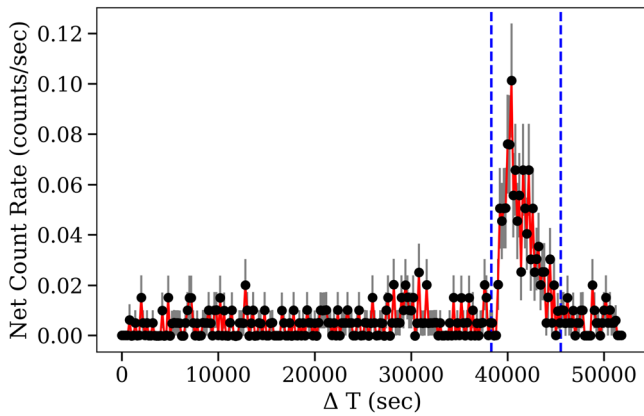


Figure 2. A background-subtracted Chandra X-ray light curve for NLTT 44989 B, showcasing a strong stellar flare during the exposure. Vertical dashed blue lines indicate the time period used for isolating the stellar flare. Counts are merged into 200 s bins. Light curves for all of the other X-ray data sets can be seen in Figure 16 in the Appendix.

from the Local Interstellar Cloud model of S. Redfield & J. L. Linsky (2000),¹² which gave relatively small values of 10^{16} – 10^{18} cm^{-2} because the model only extends out to a few parsecs. Using these low densities, including the absorption model component had functionally no impact on the resulting coronal parameters—the minuscule changes were significantly smaller than the underlying parameter uncertainties. Given that our stars can be found out to nearly 50 pc, we also tested with column densities of $\sim 10^{20}$ cm^{-2} for the highest- and lowest-SNR data sets; this indicated the resulting coronal parameters and fluxes would deviate by no more than $\sim 0.1\sigma$ – 0.5σ , insufficient to change the interpretation of our results. Based on this and the low densities from S. Redfield & J. L. Linsky (2000), we removed the absorption component for simplicity.

Another concern was pileup, the coincident arrival of two or more X-ray photons in the same pixel region within a single frame time. We used the Sherpa `jdpileup` implementation of the J. E. Davis (2001) pileup model and followed suggestions in the Chandra ABC Guide to Pileup documentation.¹³ Test fits indicated the pileup parameters `alpha` and `psfrac` were poorly constrained even in our best cases, so we adopted a fixed pileup model with parameters set to typical values advised by the documentation. When the fit-measured pileup fractions were $\lesssim 1\%$, the overall impact was negligible and changed the resulting coronal parameters by markedly less than the underlying uncertainties—the pileup component was removed in these cases for simplicity. When $\gtrsim 1\%$, values sometimes changed by more than the uncertainties, especially in cases with a second hotter coronal component—the pileup model was kept in these $\gtrsim 1\%$ cases and typically slightly improved the reduced- χ^2 . Table 3 reports a pileup fraction if it was included in the spectral model for a data set.

Each spectrum was tested with gradually increasing model complexity, including one-temperature and two-temperature coroneae, pileup inclusion or exclusion as outlined above, varying or fixed global coronal abundances, and alternate VAPEC models that use APEC models just with different combinations of fixed and varying individual elemental

abundances. Such thorough testing was motivated by the range of SNR values and different features present in various data sets. Final model selections were informed foremost by the reduced- χ^2 proximity to unity, the presence of any poorly constrained or unconstrained parameters in the solution, the visual quality of the fit to the data, and in some cases F-test comparisons between competing models. We favored simpler models and consistent choices when there was an ambiguity in the best choice. Example spectral fits can be seen in Figure 3 for the β Pic Moving Group members 2MA 0201+0117 A and B, with all other quiescent spectral fits shown in Figure 17 in the Appendix. For most cases, one-temperature corona models provided reasonable fits to the data. A second temperature component was indicated but not fully constrained for data sets GJ 1183 A–2, GJ 1183 A–3, and GJ 1183 B–3.

A few notes about the global coronal abundances are in order. In two cases, GJ 1183 B–2 and KX Com A–2, the abundances were not constrained, so were instead fixed to quiescent values obtained from separate exposures on the same stars taken earlier in each day. Global abundances were otherwise fixed to a representative subsolar value of 0.15 if unconstrained in other fits, with 0.15 determined from the average measured abundance we see in the quiescent data sets. We tested our fixed subsolar abundance cases using a solar abundance instead, but most F_X and coronal temperature results deviated by less than $\sim 1\sigma$ – 2σ . We ultimately chose to exclude solar-abundance-fixed models given that all of our measured abundances indicated firmly subsolar values around 0.1–0.2, in agreement with the typically subsolar coronal abundances found in other M dwarfs (J. Robrade & J. H. M. M. Schmitt 2005). For the four flaring events, we used the same fixed 0.15 subsolar coronal abundance where needed despite knowing that abundances can change during X-ray flares (e.g., F. Favata et al. 2000) because our one measured abundance during a flare was still subsolar at 0.092 in NLTT 44989 B. Flares are not our principle science focus here; a more careful analysis of the flares is possible, but beyond the scope of this work. Finally, we note that subsolar abundances were indicated but not fully constrained for the GJ 1183 A–2–Flare, GJ 1183 B–2, KX Com A–2, and KX Com BC–3 data sets.

We report 68% confidence interval (1σ) asymmetric uncertainties for the APEC coronal parameters, computed with the `conf` Sherpa sampling method. X-ray fluxes were determined between 0.3 and 10 keV using the `sample_energy_flux` Sherpa method, which repeatedly draws parameter values and sums over the model to calculate a flux at each iteration. We adopt the median of the resulting distribution of 10,000 flux samples as our chosen flux value, with the asymmetric 1σ bounds of the distribution as our flux uncertainties.

Results from the Chandra X-ray analysis are discussed later in Section 4.4.

3.4.1. NLTT 44989 A Detection

The expected source location for NLTT 44989 A at the epoch of the Chandra observation, based on Gaia DR3 coordinates and proper motions, did not show a clear detection above the background noise, nor did the `wavdetect` source-detection method identify any sources within several arcseconds. The projected separation of the AB pair gives an orbital period > 1000 yr, eliminating orbital motion as a possible explanation. Furthermore, the Gaia astrometry over 2014–2017

¹² We used the column density web calculator available at <http://lism.wesleyan.edu/ColoradoLIC.html>.

¹³ The Chandra pileup guide is found at https://xc.harvard.edu/ciao/download/doc/pileup_abc.pdf.

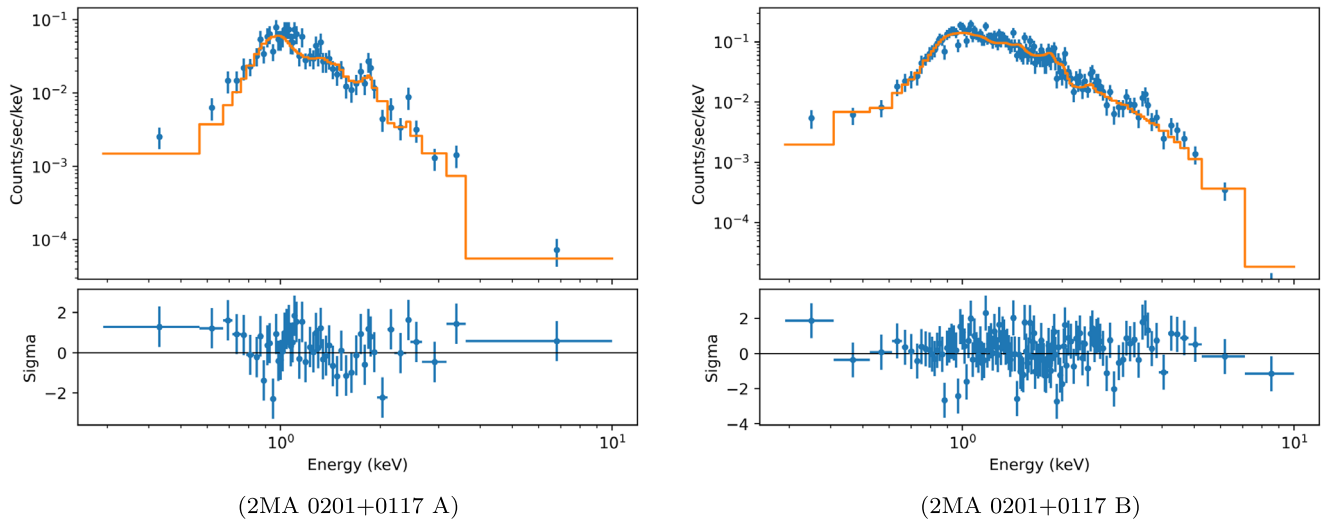


Figure 3. Blue data points show the observed Chandra coronal X-ray spectrum from 0.3–10 keV for the β Pic Moving Group members 2MA 0201+0117 A and B, grouped to 9 counts per bin. Overplotted in orange are the forward-folded best-fit APEC models; A uses a single-temperature component whereas B uses a two-temperature component in the coronal model. The bottom panels show the residual values divided by the errors, with horizontal bars indicating the energy bin widths. Spectral fits for all of the other quiescent X-ray data sets can be seen in Figure 17 in the Appendix.

yielded a proper motion for A that is consistent with the RECONS proper-motion fit using data over 2019–2024,¹⁴ indicating no deviation in the star’s path between Gaia DR3 and the Chandra observations in 2022.

There is a weak grouping of roughly 5–10 counts across all energies over several pixels within $\sim 1''$ of the expected location, but this is qualitatively comparable to many other regions of noise in the image. That said, we cannot strictly rule out the possibility of some detected source photons from A, so we used the few counts at its expected location to derive an upper limit on its X-ray luminosity and emission measure.

We used a 2 pixel radius source aperture centered at the expected location of NLTT 44989 A to capture the small grouping of nearby counts. After filtering to 0.3–10 keV and subtracting the background, only 4.3 counts remain. The associated count rate was then used with the Chandra PIMMS¹⁵ calculator to determine an X-ray flux assuming an APEC source model ($T = 10^7$ K, Abundance = 0.2, Redshift = 0, $nH = 0$), returning a Norm value of 2×10^{-6} as well. The final limiting luminosity and emission measure values are reported in Table 3. If the 4.3 counts are true source photons and not a coincidental clustering of background noise, then this offers a rough estimate for the NLTT 44989 A X-ray flux under our model assumptions; it otherwise gives an approximate upper limit only.

3.5. Speckle Imaging—SOAR and LDT

GJ 1183 AB and NLTT 44989 AB were observed using the High-Resolution Camera (HRCam; A. Tokovinin 2018) with the SOAR Adaptive Module (SAM; A. Tokovinin et al. 2016) on SOAR through a separate RECONS project led by coauthor Vrijmoet and summarized in E. H. Vrijmoet et al. (2022). Observations occurred during 2019–2020, with one visit to the GJ 1183 AB system and two visits to the NLTT 44989 AB

system. Data were taken in the I band, and otherwise used procedures typical for the observing program as outlined in E. H. Vrijmoet et al. (2022). Data were processed using the methodology of A. Tokovinin et al. (2010) and A. Tokovinin (2018), yielding measures of the angular separation and magnitude difference either as detections or limits.

2MA 0201+0117 AB and KX Com A-BC were observed with the Quad-camera Wavefront-sensing Six-wavelength-channel Speckle Interferometer instrument (QWSSI; C. A. Clark et al. 2020) on the Lowell Discovery Telescope as part of an ongoing RECONS speckle effort led by coauthor Henry. Stars were observed once each during 2021 in each of the four 40 nm wide channels at 577, 658, 808, and 880 nm. Data were processed following the procedures typical for QWSSI, which are similar to that of its predecessor DSSI as outlined in E. P. Horch et al. (2009), E. P. Horch et al. (2015). As with the SOAR data, the results are parameters for detections or limits for nondetections.

Results from the speckle analysis are discussed later in Section 4.5.

3.6. Blending and Contamination

Our new data from all five observing campaigns spatially resolve the A and B components in a twin pair in all four cases in reasonably good seeing. As shown in Table 1, GJ 1183 AB, KX Com A-BC, and 2MA 0201+0117 AB are well separated by $7''$ – $13''$, and all three systems are also free from contamination because the nearest background Gaia DR3 sources are $>15''$ away at $E_p = 2021.0$.

For the closest of the four pairs, NLTT 44989 AB with a separation of $4''.75$, care was taken to only observe and use data with suitably good seeing to prevent AB blending. Background contamination is more complex for this system given its location in a dense field, with sources closer than roughly $4''.5$ possibly contaminating the new measurements. Here we examine potentially contaminating sources, although overall we deem all of the new observations of NLTT 44989 A and B to be suitably free from contamination at any meaningful level.

¹⁴ The RECONS data undergo a full astrometric analysis alongside each photometric analysis, yielding the RECONS proper motion mentioned here. See T. J. Henry et al. (2018) for a recent summary of the RECONS long-term program.

¹⁵ PIMMS is found at <https://xc.harvard.edu/toolkit/pimms.jsp>.

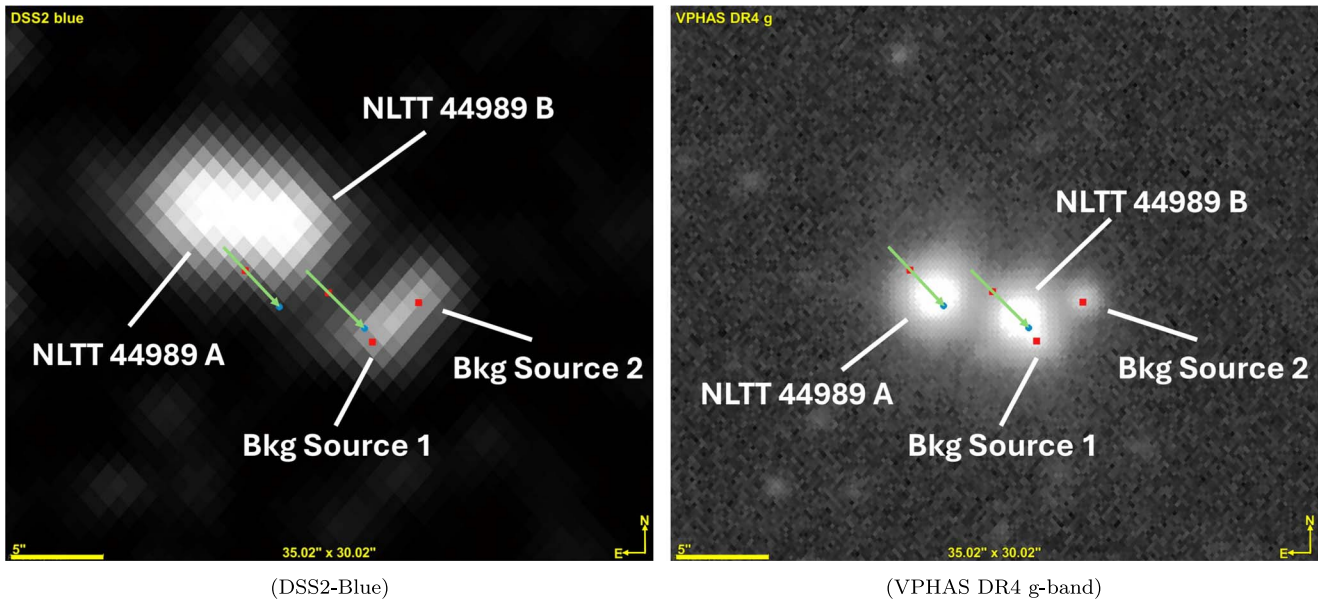


Figure 4. Optical images of the NLTT 44989 AB system, showing the relative positions of the brighter target M dwarfs and fainter background contaminating sources. The left panel shows a DSS2-Blue image taken roughly half a century ago (Ep. \approx 1975; B. M. Lasker et al. 1996; R. R. Gal et al. 2004), and the right panel shows a VPHAS DR4 g -band image taken more recently, about a decade ago (Ep. \approx 2012; J. E. Drew et al. 2014). Red squares and blue circles show the relevant source positions from Gaia DR3 at J2000 and J2016, respectively, with green arrows along the proper-motion vectors of the twin stars—the background sources have negligible proper motions. Our new observations of the system span 2019–2024, when proper motion has moved B farther on top of background source 1. Several other background sources in Gaia DR3 are not shown in these images for visual clarity, but all are negligibly faint and/or resolved from our target stars. See Sections 3.6 and 3.6.1 for a discussion of the small contamination impacts in the various observations we use.

NLTT 44989 A has two Gaia sources within $4''.5$ away but each is ~ 6.5 mag fainter than A at G , making them negligible in the optical where four of our five campaigns observe. In X-rays, we see no confident detection at A’s location (Section 3.4.1) nor at its $<4''.5$ nearby neighbors, so we consider the star to be uncontaminated in the Chandra measurements as well.

NLTT 44989 B has several background sources within $4''.5$; all are negligible at 6.4 – 7.4 mag fainter in G except for two that warrant further consideration. The first (source 1) is separated from B by only $0''.22$ at 2021.0 ($0''.84$ away at Ep = 2016.0), is 3.75 mag fainter in G , and has no parallax information available. The second (source 2) is $3''.02$ away at 2021.0 ($3''.23$ away at Ep = 2016.0), is 3.97 mag fainter in G , and is possibly an evolved giant star based on the Gaia DR3 parallax with large error. Both are shown relative to the twin system over time in Figure 4. In the 0.9 m photometry of NLTT 44989 B, we utilize relative brightness changes, so while source 1 always adds $\sim 3\%$ contaminating flux, its impact is negligible within our uncertainties—this assumes source 1 does not vary by large fractions of its entire brightness at timescales (or morphologies) matching our observed signal. Source 2 is trickier for the 0.9 m because seeing changes that vary the contaminating flux could easily mimic a weak variability signal. We took extreme care to only observe with excellent seeing $\leq 1''.4$ and manually reviewed radial source profiles for all 0.9 m frames to remove any cases with unacceptable overlap between the B star and source 2 light distributions. TESS data, which always have both background sources entirely blended with both NLTT 44989 A and B, yield period measures from two sectors that are consistent with the 6.55 day signal we see in the 0.9 m photometry of B (discussed later in Section 4.2), confirming that variable blending with source 2 is not markedly influencing our 0.9 m results for B. In addition, a fully convective M dwarf with this period would be

expected to display activity that is generally consistent with what we observe in $H\alpha$ and L_X for B (Section 5). In the CHIRON spectra of B, source 1 adds $\sim 3\%$ contaminating optical flux while source 2 may occasionally contribute minimal contamination from its wings depending on the seeing. However, the $H\alpha$ EWs are total brightness measures (as opposed to differential measurements), and B’s observed $H\alpha$ variability is well beyond 3% (Section 4.3), so these sources do not meaningfully impact the $H\alpha$ results. For RVs, our measures from the CHIRON spectra for NLTT 44989 A and B are consistent and in agreement with resolved Gaia DR3 RV values as well. Finally, in the X-ray observations, we do not see a clear indication of B’s X-ray source being a merged or multisource profile with source 1, and we also see no signal beyond the noise at the location of source 2.

Considering the rotation archival data sources, for all systems for which data are available in ZTF, the components are resolved. TESS and ASAS-SN data always blend A and B together in each system, sometimes with background sources too, but their resulting blended periods agree with the periods we find in the resolved 0.9 m data, so we do not elaborate further on their contamination here, with the exception of NLTT 44989 A discussed further in Section 4.2.

3.6.1. Blending and Contamination in the Gaia and 2MASS Apparent Magnitudes

The final data we assess for contamination are the BP, RP, J , H , and K_s magnitudes we used for selecting equal-mass components, where disruptions could make non-twins appear falsely twin-like and influence the interpretation of our results with even small deviations. Focusing first on Gaia BP and RP, values are obtained from spectral extraction windows $3''.5$ by $2''.1$ in size (F. De Angeli et al. 2023), subsequently sampling a region roughly $3''.5$ by $3''.5$ wide around a given source as Gaia

scans along different angles—two sources closer than roughly $3''.5$ would therefore contaminate each other. We can estimate the contaminating flux in BP and RP using Gaia DR3 G because G magnitudes come from spatially smaller windows with profile fitting and are much less susceptible to nearby contamination (C. Fabricius et al. 2016; N. Rowell et al. 2021). All four systems here have AB separations $>4''$ so do not blend A and B, and GJ 1183 AB, KX Com A-BC, and 2MA 0201+0117 AB all lack background sources within at least $15''$ of each star so are entirely uncontaminated. NLTT 44989 A has a single source within $3''.5$ but it only adds $\sim 0.2\%$ flux in G so A is also functionally uncontaminated. However, NLTT 44989 B has five background sources $0''.84$ – $3''.26$ away at $Ep = 2016.0$ totaling about 6.3% extra optical flux based on G , possibly falsely brightening BP and RP for the component by up to that much depending on the exact extraction regions and spectral energy distributions of the background sources.

We also assessed the Gaia DR3 `phot_bp_rp_excess_factor`, which compares combined BP and RP fluxes relative to G fluxes to find inconsistencies between the measures that can indicate contamination or other issues (M. Riello et al. 2021). We calculated the corrected C^* excess factors for this using the relations provided in Table 2 of M. Riello et al. (2021), finding seven of our eight components have minimal excess BP+RP flux $\leq 3.1\%$, but the eighth case of NLTT 44989 B again finds a 6.3% excess, congruent with our more approximate manual estimations of contaminating fluxes above. Furthermore, the background source $0''.84$ away from NLTT 44989 B at $Ep = 2016.0$ and 3.75 mag fainter in G (source 1 above) has the Gaia parameter `ipd_frac_odd_win` (IPDfow) significantly elevated at 80% , meaning most scans have this background source’s astrometric G -band windows truncated or otherwise disrupted; this implies source 1 and B are somewhat blended in their individual G measurements as well, so further contaminating deviations of order $\sim 1\%$ – 3% might exist in G and the subsequent BP+RP excess for NLTT 44989 B but are hard to constrain.

Overall, this indicates the BP and RP measures are not markedly impacted by blending or contamination for seven of our eight components, with just NLTT 44989 B possibly having BP and RP falsely brightened by up to approximately 6.3% (~ 66 mmag). We used BP to estimate our masses (see Section 2), so NLTT 44989 B may therefore actually have a mass very slightly smaller than we calculated. The important implications of this for our results are discussed later in Section 7.1.5.

Now considering the 2MASS catalog used in our target selection criteria, it hosts $2''.0$ pixels and a typical $2''.4$ – $2''.7$ FWHM (M. F. Skrutskie et al. 2006). Per the 2MASS catalog, our sources’ 2MASS magnitudes were derived from either PSF profile fitting or $4''$ radii apertures, with $14''$ – $20''$ background annuli—sources within $5''$ of each other also used simultaneous multicomponent fitting. GJ 1183 AB, KX Com A-BC, and 2MA 0201+0117 AB are therefore resolved and uncontaminated in all three bands given their $7''.72$ – $13''.07$ AB separations and aforementioned lack of background sources within $15''$ —KX Com A-BC at $7''.72$ may have minimal blending on the wings, but its 2MASS magnitudes are ignored given that we already know it has a third companion blended into its photometry. NLTT 44989 A and B show some overlap between their wings, with nearby contaminating background sources almost certainly mildly disrupting the target star

measures and sky background corrections. That said, our nearby M dwarf stars are much brighter in the 2MASS near-IR bands than the distant background stars. Minor issues impacting both components similarly would still retain similar relative measures as well. The 2MASS magnitude uncertainties for our four systems span 0.016 – 0.061 mag, which, compared to our <0.10 mag selection cutoff, indicates that minor contamination of up to several percent would also not markedly impact our results. Overall, our mass estimates derived from the higher-resolution BP mags are in excellent agreement between components, showing $\Delta M \leq 2.3\%$ for the pairs here, so we do not expect these 2MASS contamination factors to change our general takeaways despite using the magnitudes in our sample construction.

4. Results

Results from each of the five observing campaigns are described next. For the long-term variability (Section 4.1), rotation (Section 4.2), $H\alpha$ activity (Section 4.3.1), and X-ray properties (Section 4.4), our primary interest is whether or not the two stars in a given twin pair display similar or dissimilar activity and rotation behaviors. For the RVs (Section 4.3.2) and speckle imaging (Section 4.5), our goal is to validate the twin natures of our targets by searching for and ruling out unseen companions.

4.1. Stellar Cycles—CTIO/SMARTS 0.9 m Long-term Campaign

One of the four systems targeted here has substantial long-term data from the SMARTS 0.9 m—the decade-long light curves of GJ 1183 A and B are shown in Figure 5. The same set of comparison reference stars is used for both target stars, so the significantly higher level of variability for A compared to B is secure. Given the long-term nature of these light curves, we strongly favor the explanation of overall enhanced spot activity in A compared to B, rather than a coincidental mismatch in spot contrast levels. Indications of stellar activity cycles are possibly evident in these light curves, but moderate rotational modulation is also present, and the true cycle periods are likely close to or longer than a decade if they exist. Nonetheless, these results indicate that the difference in spot activity is sustained over at least a decade in GJ 1183 AB. Figure 5 also shows the few years of data presently available for the other two true twin systems; 2MA 0201+0117 A and B both show substantial scatter presumably from their strong rotational modulation shown later in Figure 6, whereas NLTT 44989¹⁶ A and B both show minimal photometric variation close to the noise limit.

The long-term 0.9 m program also analyzes differential astrometry in search of positional photocenter perturbations that might indicate an unresolved orbiting companion (see E. H. Vrijmoet et al. 2020 for a recent discussion of this process with these data). No such perturbations are seen in the 10 yr of astrometry for GJ 1183 A and B or in the more limited ~ 2 – 5 yr of data available for the other three systems, consistent with no additional companions within the measurement limitations (roughly 7 mas photocentric displacement). Proper motion has also not moved any of the systems over background stars during the ~ 2 – 10 yr of long-term 0.9 m observations for these targets, except for NLTT 44989 AB where minimal motion of

¹⁶ NLTT 44989 AB was observed in the I band for the long-term visits shown in Figure 5 but the V band for the rotation observations shown later in Figure 6.

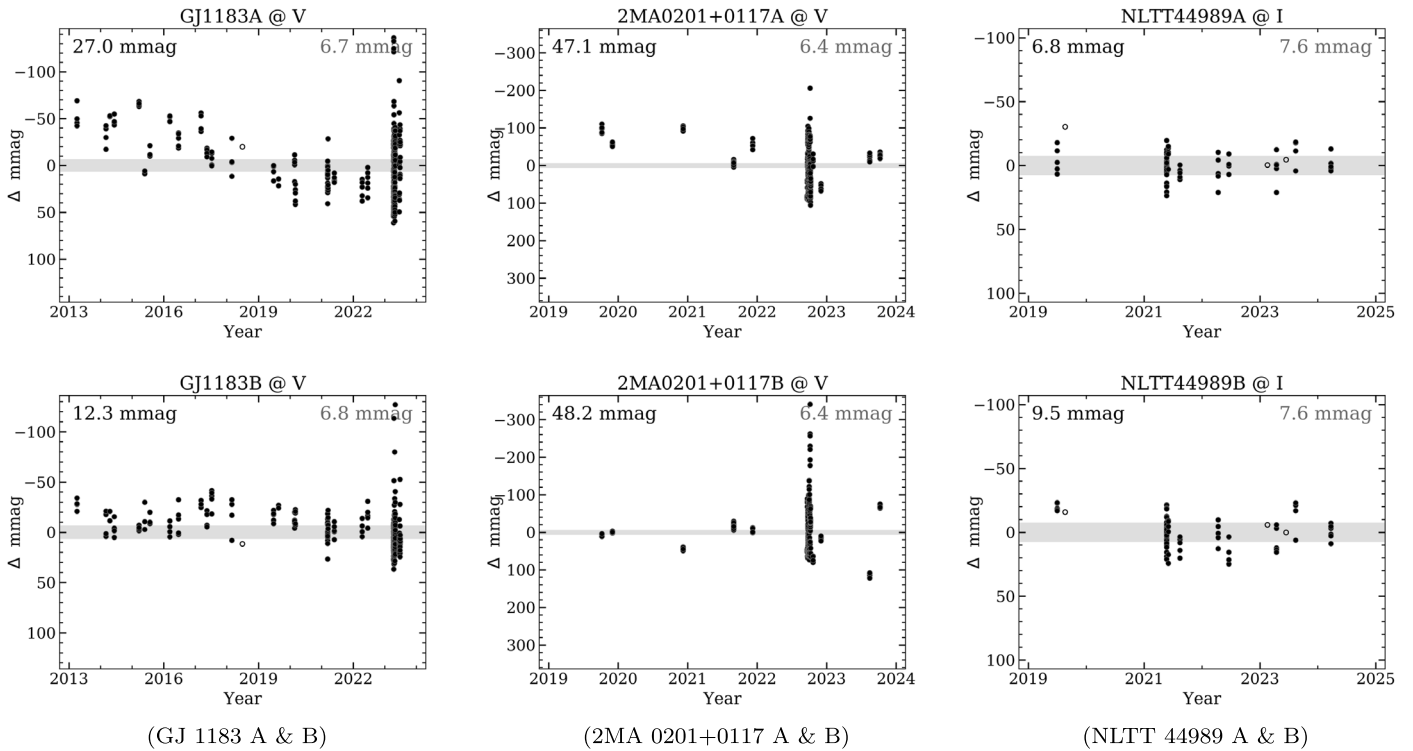


Figure 5. Long-term 0.9 m light curves for the three true twin systems. A (top) and B (bottom) components are shown for each pair, with a brightening trend indicated by a rise in each plot. Observation filters are noted in each subplot title. GJ 1183 A and B are shown spanning over a decade of coverage, while the other two systems capture several years. Note the very different y-axis scale for 2MA 0201+0117 A and B. Year times are the Julian epoch, i.e., J2000 plus the number of Julian years since then. Large clusters of points in 2022 for 2MA 0201+0117 AB and 2023 for GJ 1183 AB are from the additional rotation visits analyzed in Figure 6, with moderate flaring points left included here as examples. Open circles represent visits when only a single frame was secured; these are excluded from all quantitative analyses. Black numbers in the upper left of each panel are the mean absolute deviation (MAD) values (average of absolute value offsets from the mean) for the solid points for each component. Gray numbers in the top right of each panel are the average noise levels of the nonvarying reference stars used in the differential photometry analyses, again calculated as MAD values; these noise levels are indicated visually as gray shaded regions above and below 0 in each panel. The light-curve data are available as Data behind the Figure (DbF) products.

(The data used to create this figure are available in the [online article](#).)

$\sim 0''.8$ over roughly 5 yr has occurred around the nearby fainter background stars discussed in Section 3.6.

4.2. Rotation—CTIO/SMARTS 0.9 m, TESS, ZTF, and ASAS-SN

The rotation results are summarized in Table 4, providing the measured periods from each data source along with the final period we adopt for each star. In TESS and ASAS-SN data, the systems are unresolved so the periods are noted with “bl” for blended. All 0.9 m light curves are shown in Figure 6, and example light curves from the archival data sources can be seen in Figures 7 and 8. We note that the TESS and TESS-unpopular periodogram peaks can often correspond to FAPs numerically comparable to 0, hence their nonvalues for some cases in Figures 7 and 8. Here we provide details for each system.

GJ 1183 A has a period of 0.86 day in 0.9 m data, consistent with values from all other sources. The alternative alias peak around 6.5 days in the ZTF light curve is not found in the TESS data, confirming 0.86 day as the correct period. GJ 1183 B shows a low-amplitude 0.68 day signal from the 0.9 m that is supported by the presence of an asymmetric secondary peak at 0.69 day in the AB-blended TESS-unpopular results (see bottom right of Figure 7) distinct from the 0.86 day peak.

KX Com A shows a period of 2.54 days in 0.9 m data, in excellent agreement with the 2.55 day period in the resolved ZTF and blended TESS and ASAS-SN data sets. The various

strong alias peaks present in ground-based data for A do not appear in the TESS results, confirming 2.55 days as the true signal. X. Chen et al. (2020) found a 2.55 day rotation period from z_r-band ZTF data for KX Com A, and E. Magaudda et al. (2022) found 2.55 days from ABC blended TESS data, both exactly matching the results of our own rotation analyses of these data. KX Com BC exhibits a clear period of 6.93 days in the 0.9 m data, seen best in the raw light curve with two clear repeats (bottom right of Figure 6). This period is not evident in any other data set. Because B and C are unresolved, this could be the rotation period for either star, but is likely from B based on H α information discussed later in Section 6.2.

2MA 0201+0117 A and B have periods from the 0.9 m that are in excellent agreement with the resolved ZTF periods. The longer period of ~ 6 days for A is seen in all data sets. TESS blended data visually show intermixing of the stronger ~ 6 day pattern and a second weaker signal at a shorter period, presumably the 3.30 day period for the B component. Beyond what we report in Table 4, S. Messina et al. (2017b) also reported rotation periods of 6.00 days/3.41 days from ASAS (G. Pojmanski 1997), 5.87 days from INTEGRAL/OMC (A. Domingo et al. 2010), and 5.98 days/3.30 days from NSVS (P. R. Woźniak et al. 2004), all using blended photometry. M. Kiraga (2012) reported 6.01 days, also from blended ASAS data. Observations by Evryscope found 6.00 days with AB blended (W. S. Howard et al. 2020). Separate from our own ASAS-SN rotation analysis, T. Jayasinghe et al. (2019b)

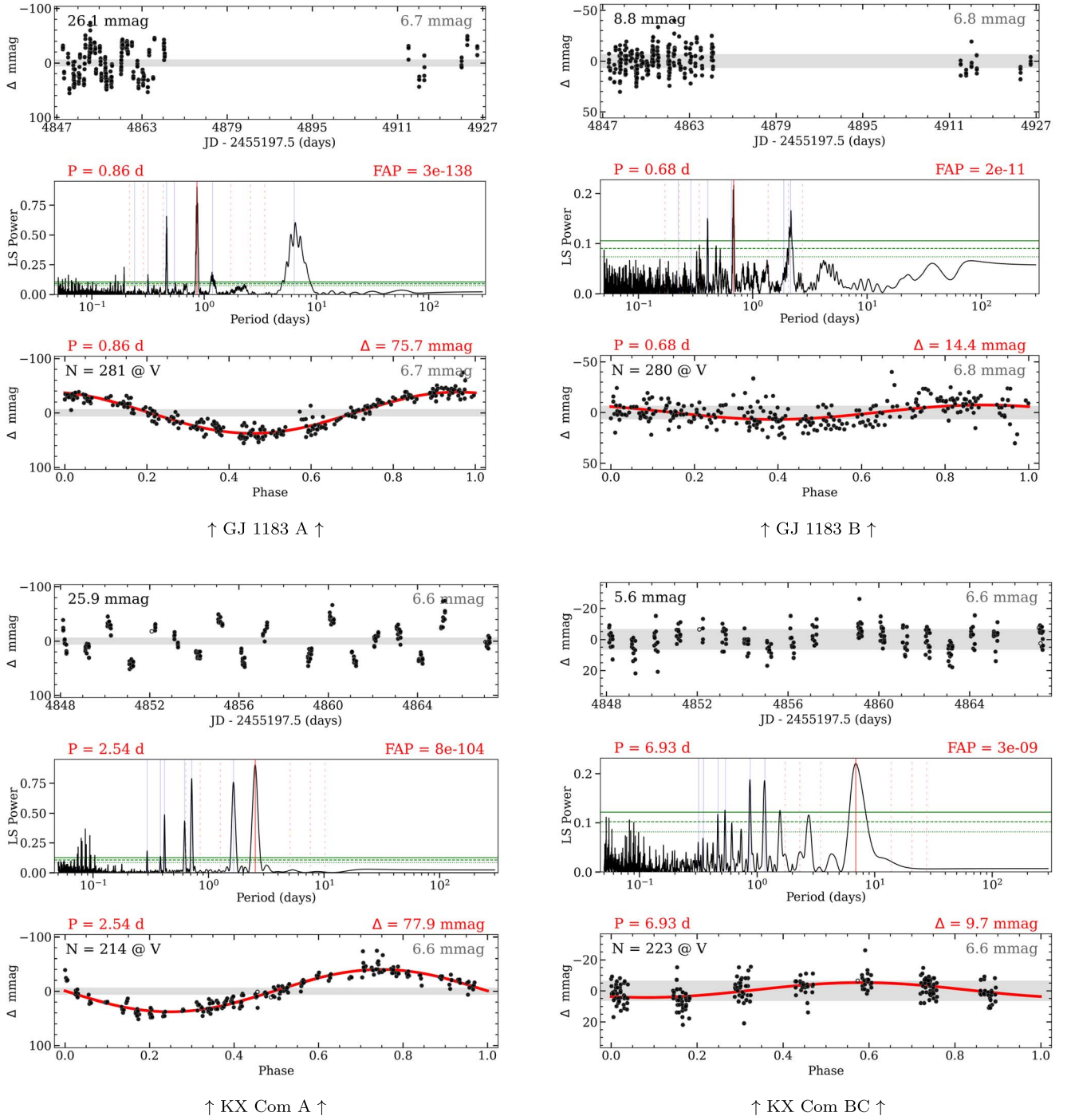


Figure 6. Each set of three vertical panels shows 0.9 m V-band rotation results for a single component in a twin system. The top panel is a relative light curve in the same general format as Figure 5, the middle panel is a Lomb–Scargle Periodogram of the same data, and the bottom panel is a phase-folded light curve of the same data based on the measured period. The Julian time of 2455197.5 corresponds to the 2010.0 epoch, a convenient reference time preceding all new observations in this paper. Note the different vertical scales between light curves. The periodogram shows horizontal green lines at the 10% (dotted)/1% (dashed)/0.1% (solid) Baluev false-alarm probability (FAP) values, the selected maximum power period peak with a vertical solid red line, vertical dashed orange lines at the 2/3/4 harmonic multiples, and vertical solid purple lines at the integer $n = [-3, \dots, 3]$ 1 day⁻¹ sampling aliases. Phase-folding begins at the epoch of the first point, with a red sine wave corresponding to the selected Lomb–Scargle model result. Values in red are given for the rotation period, FAP, and peak-to-peak amplitude (Δ) in mmag. The number of filled data points (N) and the observation filter (V for all of these stars) are given in the top left of the phase-folded subplot—open points correspond to incomplete visits that only obtained one frame. The un-phased light-curve data are available as Data behind the Figure (DbF) products. (The data used to create this figure are available in the [online article](#).)

reported 6.00 days from blended ASAS-SN data. All are consistent with our results for the stars.

NLTT 44989 A has an uncertain low-amplitude period near 38 days (or longer) in the resolved 0.9 m data. The blended PDCSAP TESS data do not show the long-period trend (see

Figure 8), presumably because it is removed by the default TESS pipeline, but we note a long-term signal does appear in both sectors’ raw SAP light curves (not shown here). The TESS-unpopular data, which better preserve long-term astrophysical trends, are shown on the right in Figure 8—a

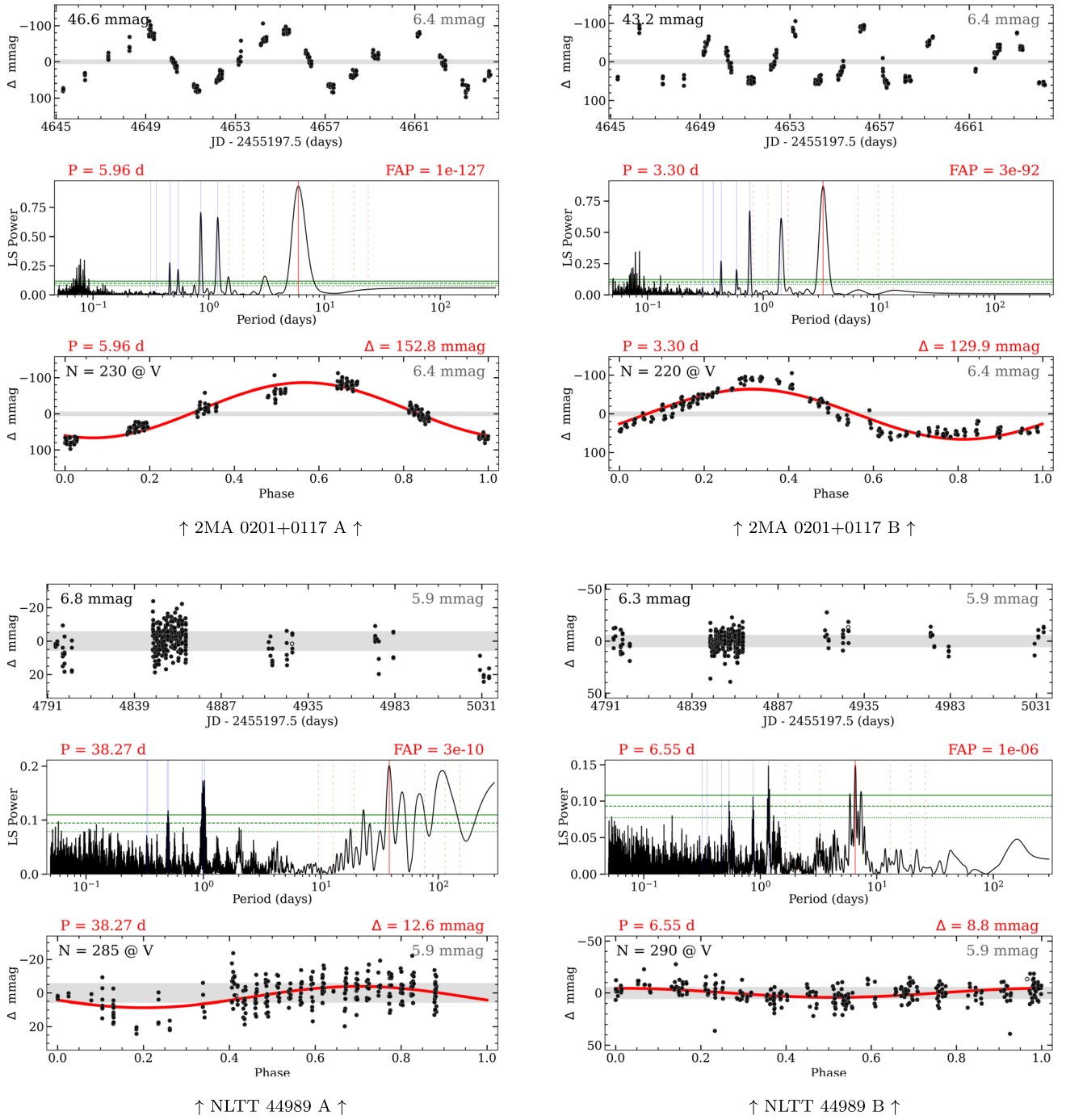


Figure 6. (Continued.)

candidate long-term signal $\gtrsim 22$ days is seen mixed with the B component’s shorter 6.55 day variations across two nonconsecutive sectors. A Lomb–Scargle analysis of the two sectors’ unpopular data merged indicates a possible period of roughly 20–100 days. Our TESS-unpopular aperture for NLTT 44989 A (with B blended) was a 3×3 pixel grid ($63 \times 63''$), capturing many faint background stars from the dense field; although A and B are still the brightest stars in the aperture. To support the trend’s connection to the A component instead of a background star, we reanalyzed the TESS-unpopular data using 16 different aperture configurations drawn from the same set of 3×3 pixels in various arrangements; the long-term signal

remained evident in both sectors for all 16 cases. In Figure 8 we overlay the 38 day 0.9 m signal extended in time to assess the phase alignment with each sector’s turnover trend, finding generally good agreement despite the two sectors and 0.9 m data all having been observed several years apart from each other—the small phase mismatch in sector 39 is possibly due to our measured period deviating slightly from the true value, or differential rotation could be occurring. We also note that as we acquired additional 0.9 m data for NLTT 44989 A, the periodogram peak around ~ 38 days generally strengthened relative to other peaks. Altogether, while the spatially resolved 0.9 m period detection is weak, it is congruent in period and phase

Table 4
Rotation Periods and Amplitudes

Name	0.9 m P_{rot} (day)	ZTF P_{rot} (day)	TESS P_{rot} (day)	TESS-unpop P_{rot} (day)	ASAS-SN P_{rot} (day)	Final P_{rot} (day)	0.9 m Δ (mmag)
GJ 1183 A	0.86	0.86 or 6.49	bl: 0.86	bl: 0.69 & 0.86	bl: 0.86	0.86	75.7
GJ 1183 B	0.68	...	bl: 0.86	bl: 0.69 & 0.86	bl: 0.86	0.68	14.4
KX Com A	2.54	2.55	bl: 2.55	bl: 2.55	bl: 2.55	2.55	77.9
KX Com BC	6.93	...	bl: 2.55	bl: 2.55	bl: 2.55	6.93	9.7
2MA 0201+0117 A	5.96	6.01	bl: [5.92–6.09]	bl: 6.33	bl: 6.01	6.01	152.8
2MA 0201+0117 B	3.30	3.30	bl: [5.91–6.03]	bl: 6.32	bl: 6.01	3.30	129.9
NLTT 44989 A	38.27	...	bl: [6.36–6.62]	bl: $\gtrsim 22$...	38	12.6
NLTT 44989 B	6.55	...	bl: [6.42–6.71]	bl: $\gtrsim 22$...	6.55	8.8

Note. Rotation periods from four sources (two treatments for TESS) are shown for the components in the four targeted systems. An unreported result for a given archival source indicates data were either unavailable or showed no confident rotation signal. Entries with a leading “bl” flag are derived from photometry with the components either partially or entirely blended. Adopted rotation periods are given in the next-to-last column, and the peak-to-peak model amplitude (Δ) in the V filter from the 0.9 m is given in the final column. This 0.9 m amplitude value is chosen because the four systems are all spatially resolved, rotation was detected in all cases, and a consistent filter was used. The 6.93 day result for KX Com BC is from photometry blending the B and C stars but resolved from A. See also Section 4.2.

with the TESS-unpopular signal and with the low activity levels we observe for the star in $H\alpha$ and L_X (Section 5), so we adopt 38 days as our final period for NLTT 44989 A. A rotation period shorter than ~ 38 days would move the star to a unique position in the rotation–activity plane for both $H\alpha$ and L_X (see Figure 14, discussed in Section 5), where no other field stars are observed to exist, further supporting the long period we adopt. A period longer than 38 days may be possible but would actually compound the A/B mismatch and strengthen our overall findings.

NLTT 44989 B shows a candidate low-amplitude 6.55 day period from the 0.9 m with a similar-strength alias peak of 1–1.5 days, but blended TESS data reveal a confident signal around ~ 6.5 days with no significant peaks in the 1–1.5 days region, confirming 6.55 days as the true signal for B.

4.3. $H\alpha$ Equivalent Widths and Radial Velocities—CTIO/SMARTS 1.5 m & CHIRON

Results from the optical spectroscopy effort are summarized in Table 5, with individual epochal values outlined in Table 6. For the four systems considered here, we measure $H\alpha$ EWs spanning -15.03 (a flare epoch) to 0.31 \AA and reach typical single-visit RV precision of 210 m s^{-1} and averages of $20\text{--}60 \text{ m s}^{-1}$. Our CHIRON RVs are in good agreement with the Gaia DR3 RVs (provided in Table 1) when available. Our $v \sin(i)$ measurements span $1.41\text{--}15.84 \text{ km s}^{-1}$, but we caution that any $v \sin(i)$ values below $\sim 10 \text{ km s}^{-1}$ should be considered less reliable, per J23, and these are enclosed in parentheses in Table 5.

At some epochs, spectra were only successfully acquired for one component, either due to inclement weather or because one star had to be thrown out due to strong cosmic rays on $H\alpha$ or critical observational mistakes. The successful component’s data are still useful for RV and $v \sin(i)$ analyses, but we entirely remove such epochs for any A–B $H\alpha$ activity comparisons to ensure we only ever compare $H\alpha$ data taken at consistent snapshots in time for both stars.

We searched for Li 6708 doublet features in our spectra but found no confident detections, even for the 2MA 0201+0117 AB binary that is a member of the β Pictoris association, nor for the GJ 1183 AB system that has components slightly elevated in the Hertzsprung–Russell Diagram (Figure 1).

4.3.1. $H\alpha$ Activity

Before comparing $H\alpha$ in binary components, we first consider observations when any component is flaring. A few visits captured prominent $H\alpha$ flares (indicated in Table 6), which we identify as epochal EWs satisfying the following: (1) show emission ($\text{EW} < 0$), (2) have stronger emission at that epoch than the median EW for the star ($\text{EW} < \text{EW}_{\text{Median}}$), and (3) the EW changes by more than 3 times the typical scatter in EW for that star ($\text{Abs}(\text{EW} - \text{EW}_{\text{Median}}) > 3 \times \text{MAD}_{\text{Median}}$). These cutoffs were derived in part via manual inspection of all of the spectra and EW time series to identify brightened outliers and flaring $H\alpha$ line profiles compared to nonflaring epochs for the same star. When comparing the $H\alpha$ activity between components, we exclude any epochs for both A and B if either star is flaring at an epoch.

$H\alpha$ EWs are compared between A and B components with an equivalency plot in Figure 9. The scatter for any individual star indicates the intrinsic $H\alpha$ variability of the source. Even accounting for this scatter, it is clear that sustained differences exist between components in all four systems examined, i.e., none of the points lie on the one-to-one line. The corresponding $H\alpha$ line profiles are compared between components in Figure 10, where the same conclusion is evident. NLTT 44989 AB offers a significant result, with one component in emission and the other in absorption. This disparity in $H\alpha$ implies very different levels of magnetically induced chromospheric heating, representing a total mismatch in magnetic activity between twin stars.

Several stars in Figure 10 display split-horned $H\alpha$ emission profiles. Such patterns are expected theoretically, as discussed in L. E. Cram & D. J. Mullan (1979), due to non-LTE and optical depth effects in the heated chromospheres of active M dwarfs. Figure 10 also demonstrates a remarkable overlap in the continuum “wiggles” between components in each system. The spectrum for a given star and epoch was RV shifted and blaze corrected in isolation, i.e., the analysis gave no consideration to the RV or spectral behavior at other epochs or in the other component. This means the overlap in continuum features is truly astrophysical and consistent over many visits (even in the RV-variable case of KX Com BC, see below), validating and underscoring the twin-like natures of our pairs.

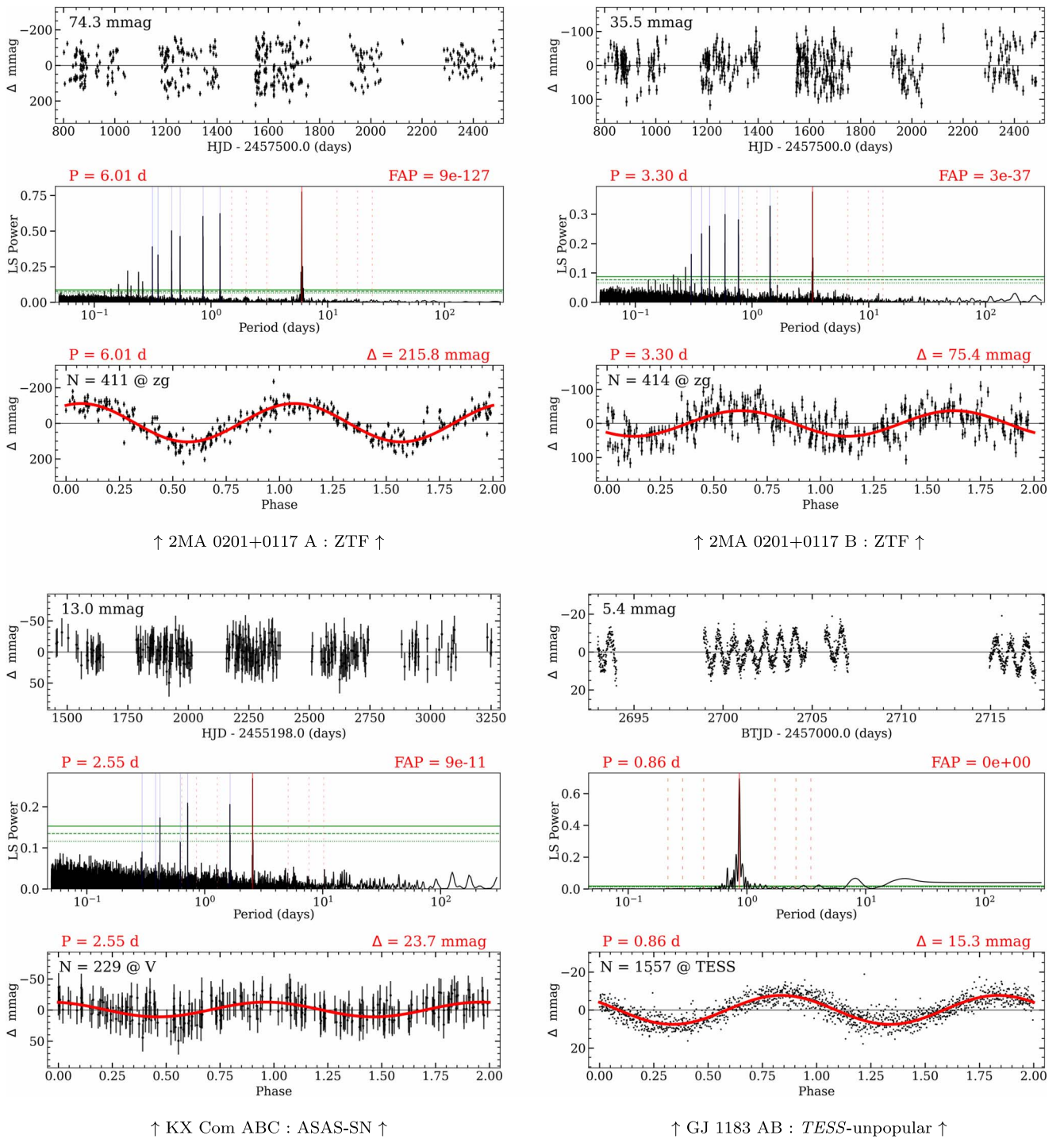


Figure 7. Format details are largely the same as for Figure 6, now showing example results using archival data from ZTF (top left and top right), ASAS-SN (bottom left), and TESS-unpopular (bottom right). The phased light curves show data folded every two phases in time instead of one phase for visual clarity. TESS is also space-based without 1 day sampling, so does not show the corresponding alias lines. ZTF spatially resolves 2MA 0201+0117 A and B, while the other two examples have the A-B(C) components blended.

4.3.2. Radial Velocities

Of the eight components in four systems, only one shows RV variations beyond the measurement uncertainties, KX Com B. As examples, the flat RV curves for NLTT 44989 A, NLTT 44989 B, and KX Com A are shown in Figure 11. The additional visits we acquired for KX Com B to further investigate its RV signal are shown in the bottom right of Figure 11 and confirm the presence of a new orbiting companion we dub “C”—this makes the overall

KX Com A-BC system a hierarchical triple. Our data provide a lower limit of ~ 24 days on the BC orbital period.

The $v \sin(i)$ measures for KX Com BC vary from 2.64 – 15.84 km s^{-1} , and double-lined SB2 behavior is seen. Our RV analysis methodology did not explicitly take this into account for KX Com BC, but the $H\alpha$ spectra shown in Figure 10 do not show marked RV misalignment, which might be expected if the RV measures were poor. Improved RVs from our data are possible for BC, but this is left as future work. The

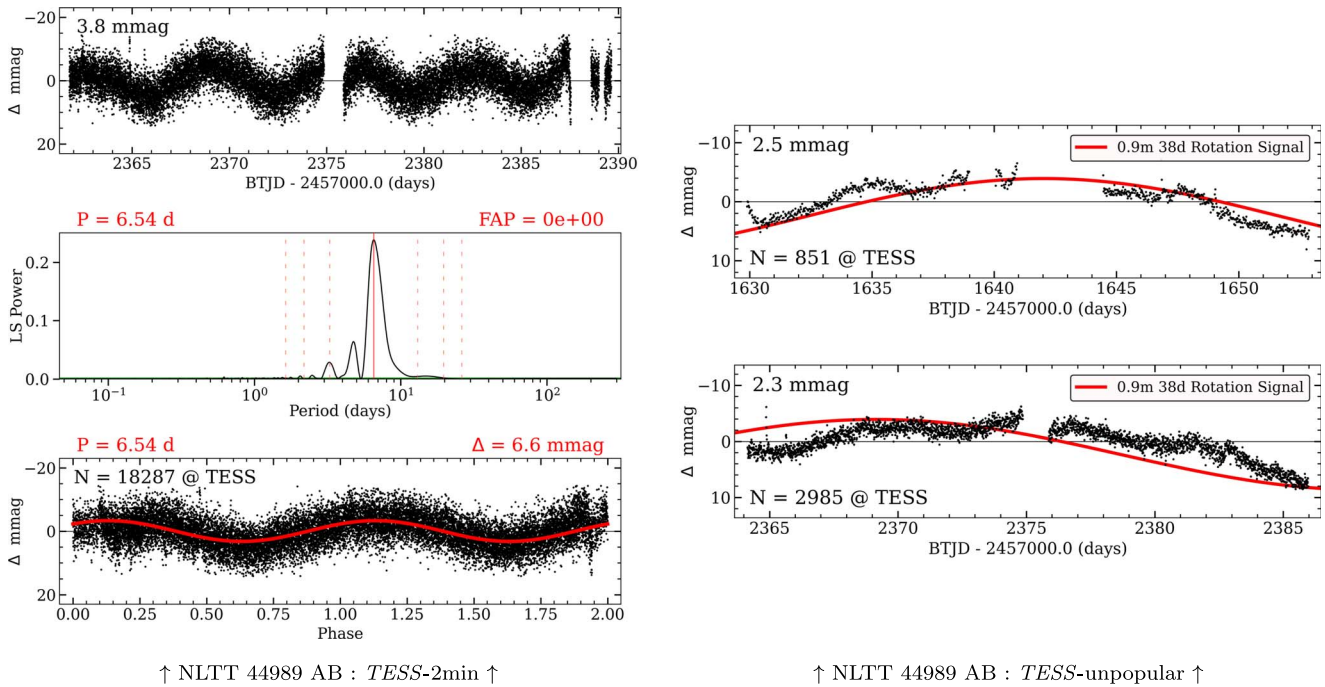


Figure 8. Blended light curves for the NLTT 44989 AB system. (Left)—TESS 2 minutes cadence PDCSAP pipeline data from sector 39, shown in the same general format as Figures 6 and 7. The ~ 6.55 day rotation period from the B component is plainly evident, while the A component’s longer signal is absent due to the default TESS pipeline processing. (Right)—Alternative TESS-unpopular light curves from sectors 12 (top) and 39 (bottom), with the MADs given in the top left and numbers of data points (N) in the bottom left. The shorter periodic rotation pattern of ~ 6.55 days from the B component is weakly visible intermixed with the more obvious long-term rotation signal of the A component. Red curves overlay the 38.27 days Lomb–Scargle sine wave result from the 0.9 m data (Figure 6) but extended in time to compare the phase alignment with the signal in each TESS-unpopular sector; the small shift in phase in sector 39 is likely explained by a small offset between the adopted and true period, or possibly differential rotation. See Section 4.2 for further discussion.

SB2 nature was further confirmed and the orbit analyzed using higher-resolution spectra in recent work by P24, discussed further in Section 6.2.

4.4. X-Rays—Chandra Observatory

Our Chandra X-ray fluxes (F_X) in the 0.3–10 keV band and Gaia DR3 parallaxes were used to calculate the X-ray luminosities (L_X) given in Table 3. The APEC-fit coronal normalization (Norm) values were converted to volume emission measures¹⁷ (VEMs) using $\text{Norm} = 10^{-14} \text{ VEM}/4\pi d^2$, per XSPEC/APEC documentation, and the VEM values are also given in Table 3.

There are individual distance measurements for each star in a given system, but components should be at functionally the same distance. We evaluated the implications of measured distance offsets by calculating L_X and VEM while fixing both components to the A then B star distances and found changes always $< 2\%$, much smaller than the L_X and VEM uncertainties themselves, owing to the precise Gaia parallaxes. Based on this, we chose to simply use the individual distance measurements for each star’s calculations in our reported results. Our asymmetric uncertainties in flux (σ_{F_X}), Norm (σ_{Norm}), and distance (σ_d) were used to calculate asymmetric σ_{L_X} and σ_{VEM} values using traditional error propagation methods on the upper and lower 1σ uncertainties in turn¹⁸.

¹⁷ This is sometimes labeled EM in other works instead of VEM. It parameterizes the coronal plasma’s electron density and volume, effectively tracing the amount of emitting material.

¹⁸ This approach yields reasonable uncertainties despite its simplifying assumptions because the typically large σ_{F_X} and σ_{Norm} radically dominate over the Gaia σ_π errors that are ~ 25 – $250\times$ smaller fractionally, enabling nearly unchanged asymmetric fractional errors upon propagation.

The left panel of Figure 12 shows a one-to-one plot comparing L_X between components of the four systems at each observing epoch. The gray diagonal line traces equal strengths, and the pink shaded region outlines a factor of 4 both above and below equality. This spread is based on the observed long-term L_X behavior of M dwarfs reported in E. Magaúda et al. (2022) that shows roughly a factor of 2 in variability scatter (see their Figure 13). Our twins could have one star sampled $2\times$ lower and the other $2\times$ higher, or the inverse, resulting in the $4\times$ value used here. Theoretical work by A. O. Farrish et al. (2021) also supports that a large portion of this scatter in L_X could be legitimate astrophysical variation linked to stellar activity cycles in M dwarfs.

Each system is worthy of comment:

NLTT 44989 AB (N in the plot) is the one system in which the two stars show a complete mismatch in L_X . This pair breaks the identical twin paradigm because the two stars’ L_X is radically different, as was also the case for their $H\alpha$ and rotation behavior. The difference between A and B is well beyond the level ascribable to intrinsic X-ray variations, so this result is robustly capturing typical behavior for the two stars. The weak- or nondetection from A (see Section 3.4.1) also means the X-ray activity mismatch may be even more pronounced than we measure here.

GJ 1183 AB (G) exhibits modest differences in L_X that can possibly be explained by intrinsic X-ray variability for isolated stars due to activity cycles. The change in quiescent L_X values between the first and second Chandra observations of A and B is intriguing given the exposures occurred only a few hours apart. We speculate that this might be due to the rapid 0.86 day and 0.68 day rotation periods causing shifted views of the stellar coronae to be visible in each observation. The two

Table 5
Optical Spectra—Mean CHIRON Measurements

Name	N_{All}	$N_{\text{H}\alpha}$	$\overline{\text{EW}}_{\text{H}\alpha}$ (Å)	$\text{EW}_{\text{H}\alpha}$ Lo-Hi (Å)	$\overline{\text{RV}}$ (km s^{-1})	$\sigma_{\overline{\text{RV}}}$ (km s^{-1})	$\overline{v \sin(i)}$ (km s^{-1})	$\sigma_{\overline{v \sin(i)}}$ (km s^{-1})
GJ 1183 A	10	7	-8.05	[-7.65, -8.57]	-11.23	0.05	13.08	0.11
GJ 1183 B	10	7	-6.37	[-5.61, -6.84]	-11.26	0.05	15.52	0.13
KX Com A	8	7	-3.71	[-2.90, -4.61]	-7.61	0.04	(4.98)	...
KX Com BC	30	7	-0.53	[-0.43, -0.82]	var	var	var	var
2MA 0201+0117 A	11	9	-3.67	[-3.18, -4.09]	5.61	0.04	(4.53)	...
2MA 0201+0117 B	10	9	-5.60	[-4.93, -6.49]	6.36	0.06	10.52	0.24
NLTT 44989 A	15	15	+0.25	[+0.31, +0.12]	42.05	0.02	(1.85)	...
NLTT 44989 B	15	15	-0.88	[-0.54, -1.42]	43.69	0.02	(2.31)	...

Note. The $\text{H}\alpha$ EW mean and range values consider only the epochs ($N_{\text{H}\alpha}$) with both A and B observed back-to-back successfully and with neither flaring. RV and $v \sin(i)$ values use all available visits for each star (N_{All}) and give the weighted means and associated uncertainties. Square brackets indicate the range of observed $\text{H}\alpha$ values. $v \sin(i)$ values $< 10 \text{ km s}^{-1}$ are less reliable measurements, indicated with parentheses and exclusion of the unreliable uncertainties.

Table 6
Optical Spectra—All CHIRON Measurements

Name	J. Epoch (YYYY.YYYY)	Flare? (y/n)	$\text{EW}_{\text{H}\alpha}$ (Å)	$\sigma\text{-EW}_{\text{H}\alpha}$ (Å)	RV (km s^{-1})	$\sigma\text{-RV}$ (km s^{-1})	$v \sin(i)$ (km s^{-1})	$\sigma\text{-}v \sin(i)$ (km s^{-1})	SNR
GJ 1183 A	2022.2497	y	-15.03	0.01	-11.03	0.14	13.28	0.38	32.8
GJ 1183 B	2022.2497	n	-6.91	0.02	-11.23	0.08	15.57	0.38	33.0
KX Com A	2021.3732	n	-3.63	0.02	-7.60	0.13	4.95	1.46	25.4
KX Com BC	2023.2708	y	-5.36	0.03	-8.79	0.17	7.12	0.68	35.0
2MA 0201+0117 A	2019.9441	n	-3.66	0.02	5.50	0.18	4.17	1.01	25.4
2MA 0201+0117 B	2019.9441	n	-4.93	0.01	6.52	0.21	10.39	0.98	21.6
NLTT 44989 A	2022.2473	n	+0.23	0.02	42.08	0.05	1.85	0.52	35.2
NLTT 44989 B	2022.2474	n	-0.69	0.11	43.68	0.07	2.18	0.46	36.1

Note. One example set of CHIRON measurements is shown here for each component. The full table of all measurements is available in machine-readable form. The “Flare?” column indicates visits with an $\text{H}\alpha$ flare observed, with “y” for a flare and “n” for no flare. Any $v \sin(i)$ values $< 10 \text{ km s}^{-1}$ should be treated as potentially unreliable, with weaker confidence as the value decreases. SNRs are for the continuum near $\text{H}\alpha$ and not the $\text{H}\alpha$ line itself.

(This table is available in its entirety in machine-readable form in the [online article](#).)

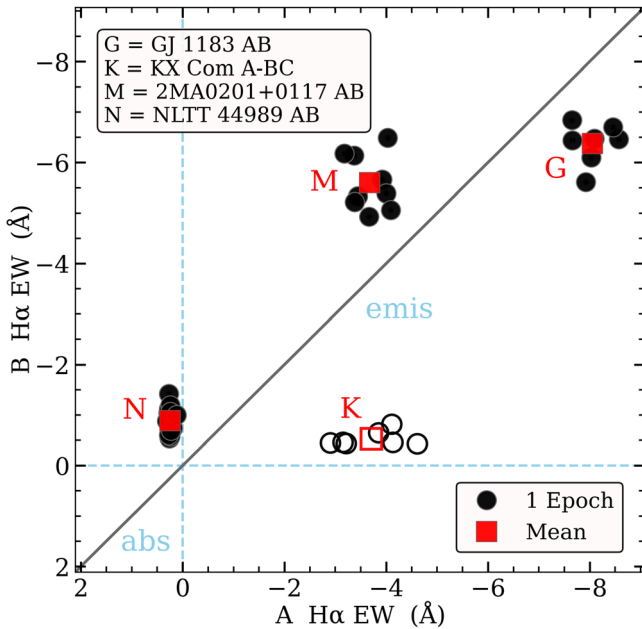


Figure 9. A one-to-one equivalency plot comparing $\text{H}\alpha$ EWs between components in each system. Individual epochal measurements are black circles while the means of these are red squares. Open symbols indicate the non-twin triple KX Com A-BC. Absorption and emission regions are indicated with blue lines and labels. We only include nonflaring epochs with both stars successfully observed back-to-back.

exposure midpoints are separated by 10.68 hr, implying that the stars would have rotated by $\sim 186^\circ$ and $\sim 236^\circ$, respectively. However, the X-ray light curve for GJ 1183 B-1 shows a few minor peaks lasting several minutes each with slightly elevated counts that could be weak flares mixed in the noise (see Figure 16). Excluding these points and reanalyzing GJ 1183 B-1, we find $F_X = 27.3_{-8.2}^{+4.5} \times 10^{-14} \text{ erg s}^{-1} \text{ cm}^{-2}$, now overlapping with GJ 1183 B-2 at $F_X = 23.0_{-1.9}^{+2.0} \times 10^{-14} \text{ erg s}^{-1} \text{ cm}^{-2}$, so the difference may instead stem from analysis uncertainty in what data points are truly “quiescent.”

2MA 0201+0117 AB (M) also exhibits a modest difference in L_X , explicable by intrinsic X-ray variability during each star’s possible cycle, although it does lie near the upper edge of the $4\times$ shaded region. This is a young PMS system, so its astrophysical X-ray behavior may be somewhat different than that of the dwarf stars used in E. Magaudda et al. (2022), and it might be expected to exhibit larger-than-average L_X variations.

KX Com A-BC (K) is not a true twin, given that one component has a close companion, so it is shown with open symbols in Figure 12 and subsequent X-ray Figures. Offsets from the one-to-one line may be due to interactions of the B and C stars and/or their different masses and rotation from the A component.

The right panel of Figure 12 compares VEM between components, where the overall trends align well with L_X —this shows that where we find higher or lower X-ray luminosities,

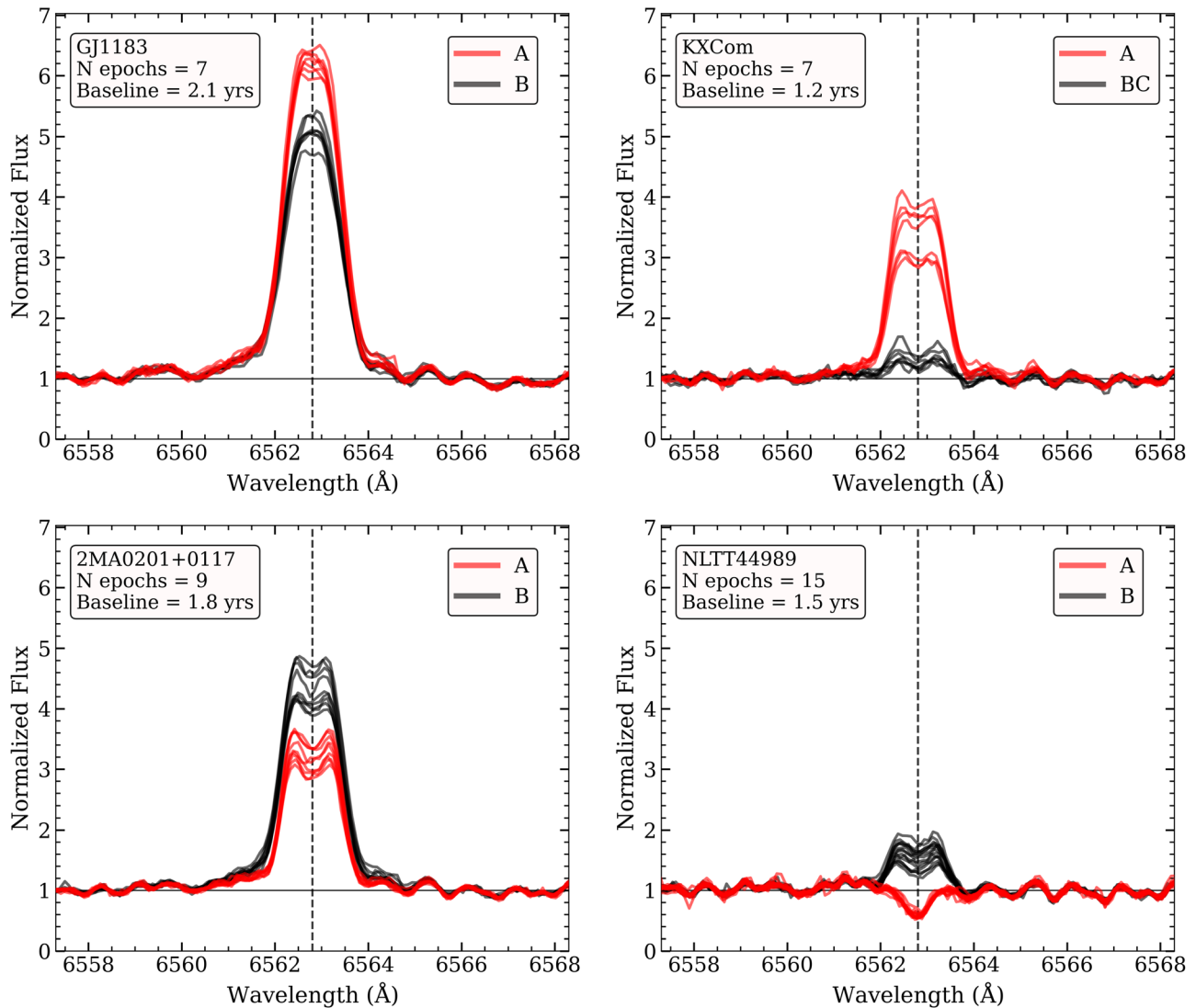


Figure 10. CHIRON spectra of the $H\alpha$ line region—shifted to zero RV and blaze corrected—stacked for multiple epochs to visually compare the A and B components in each system. We only include nonflaring epochs with both stars successfully observed back-to-back; the legends indicate the final number of epochs shown and the time span of those spectra. Work by E. K. Pass et al. (2024) indicates the emission seen in the blended spectra for KX Com BC is primarily from the B star while C is flat (see Section 6.2).

we correspondingly measure higher or lower amounts of emitting coronal plasma. The coronal temperatures, not plotted here, show no definitive patterns beyond a possible slight indication of larger X-ray luminosities at hotter temperatures. A comparison of the coronal temperatures between the A and B components also yields no confident trends of note, with most temperatures being in the region of 8–13 MK.

4.5. Speckle Imaging—SOAR and LDT

For each component in the four systems, speckle observations found no additional companions down to subarcsecond separations. An example detection limit curve from QWSSI +LDT for 2MA 0201+0117 A is shown in Figure 13. In the 880 nm band, the LDT results generally reached to roughly $\Delta\text{mag} \approx 1.9$ at $0''.1$, $\Delta\text{mag} \approx 3.4$ at $0''.2$, and $\Delta\text{mag} \approx 4$ at $\gtrsim 0''.3$. The RV companion to KX Com B was not detected by speckle at LDT due to the small separation of 0.13 au, or 5 mas at 27 pc, expected for an orbital period of 25 days for these stars with masses of $\sim 0.2 M_{\odot}$ (see Section 6.2). In the I band, the SOAR results typically reached $\Delta\text{mag} \approx 2.5$ at $0''.15$ and

$\Delta\text{mag} \approx 3.3$ at $1''.0$. We did not detect the background contaminating source underneath NLTT 44989 B (discussed in Section 3.6), presumably because it has separations from B of $0''.29$ and $0''.23$ at the epochs of the two SOAR visits and a ΔG of 3.75 mag, putting it beyond the detection limits. Overall, these nondetections in all four systems help preclude potentially unresolved companions that would break the twin natures of the pairs.

5. Rotation-activity Comparisons

Many efforts have shown that the rotation–activity relationship for M dwarfs divides into rapidly rotating stars with saturated activity and slower-rotating stars with unsaturated activity that follow a Skumanich-like trend (A. Skumanich 1972). We plot our twins in this space in Figure 14 for both chromospheric $H\alpha$ activity and coronal L_X activity, underplotting results from E. R. Newton et al. (2017), N. J. Wright et al. (2011), and N. J. Wright et al. (2018) to illustrate the saturated and unsaturated regimes. We re-derived L_X values for the N. J. Wright et al. (2018) sources using Gaia DR3

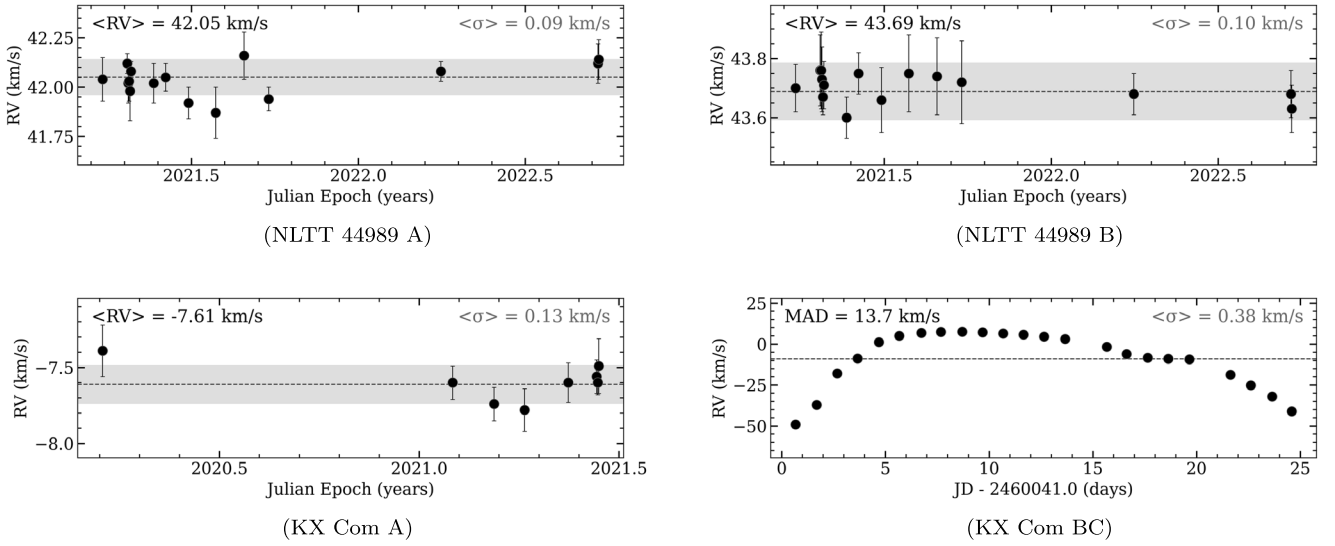


Figure 11. Radial velocity time series from CHIRON for four resolved targets. The weighted average RV value for each case is shown with a black dashed line and given in black in the top left (except KX Com BC listing the MAD instead), with the average single-point uncertainty spanning above and below in gray and given in the top right. Error bars are always shown, but appear smaller than the points for KX Com BC owing to the different scale. (Top)—NLTT 44989 A and B show all 15 epochs across roughly 1.5 yr, with neither star showing RV variations beyond the noise. (Bottom)—KX Com A also appears nonvarying within the noise for the eight available epochs. In contrast, KX Com “B” shows the only case we find with RV variations, which we ascribe to orbital motion with an unresolved third component “C.” We only show 23 of the 30 total epochs available for KX Com BC so as to highlight the orbital arc captured from our sequential visits throughout 2023 April.

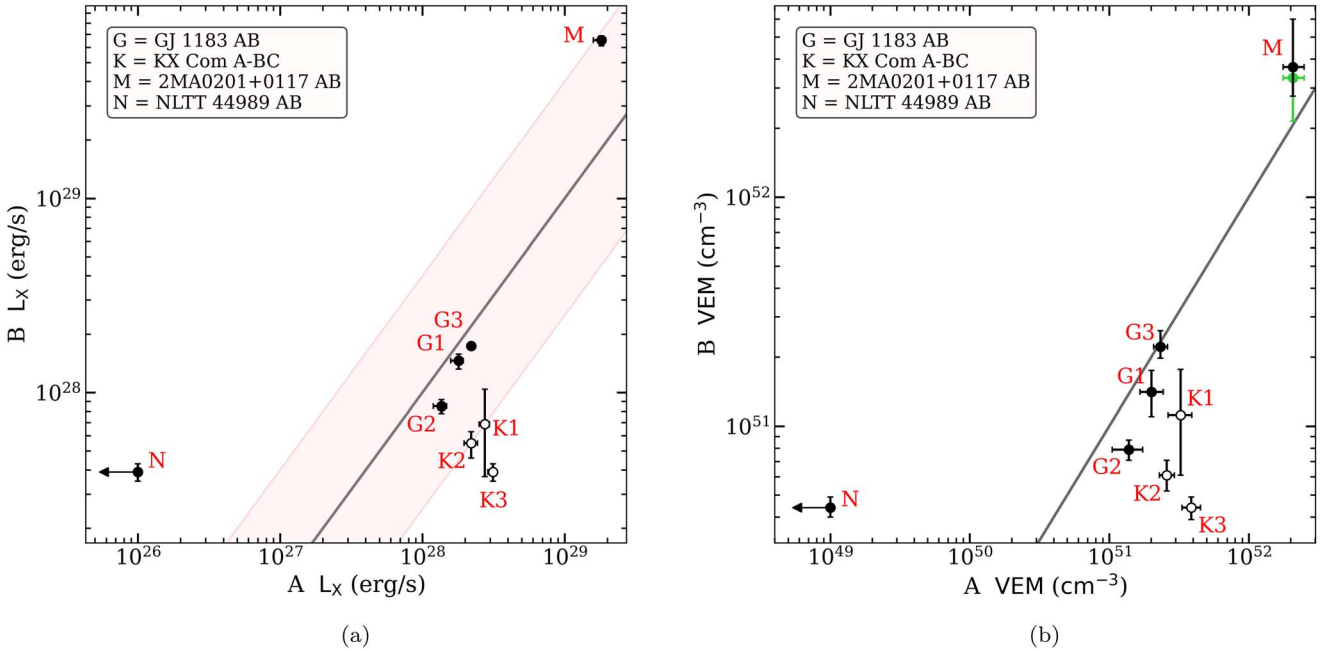


Figure 12. One-to-one equivalency plots comparing (a) L_X and (b) VEM between components in each of the four systems for each observation ID. The cases with three exposures from Chandra—KX Com A-BC and GJ 1183 AB—have results from their individual epochs numbered after the associated system letter label following the designations in Table 3. Gray diagonal one-to-one lines are shown along with leftward arrows for the upper limits on NLTT 44989 A. Open symbols indicate the non-twin triple KX Com A-BC. In panel (a), the pink shaded region shows a factor of 4 both above and below the one-to-one line (see Section 4.4 for discussion). In panel (b), a green point indicates the hotter component in the 2T model result for 2MA 0201+0117 B.

parallaxes and their reported Chandra X-ray fluxes in an energy bandpass very similar to ours.

We plot P_{rot} , L_X , and $H\alpha$ EW directly, instead of the often used Rossby number ($R_o = P_{\text{rot}}/\tau_{\text{conv}}$), L_X/L_{bol} , and $L_{H\alpha}/L_{\text{bol}}$ parameters for a few reasons. Traditionally, the incorporation of τ_{conv} and L_{bol} helps account for the luminosity and convective properties changing with mass when considering a collection of different mass stars; the minimum $H\alpha$ absorption depth is also a function of mass (J. R. Stauffer &

L. W. Hartmann 1986; E. R. Newton et al. 2017). Luckily, our twin stars have nearly identical masses, meaning their τ_{conv} and L_{bol} factors would be functionally the same—a robust comparison between our twin components is therefore possible in the rotation–activity plane without applying these corrections. This has the added benefit of avoiding empirical relations often used to derive these parameters, which would otherwise add new assumptions and uncertainties at each step. For example, we previously showed in W.-C. Jao et al. (2022) that

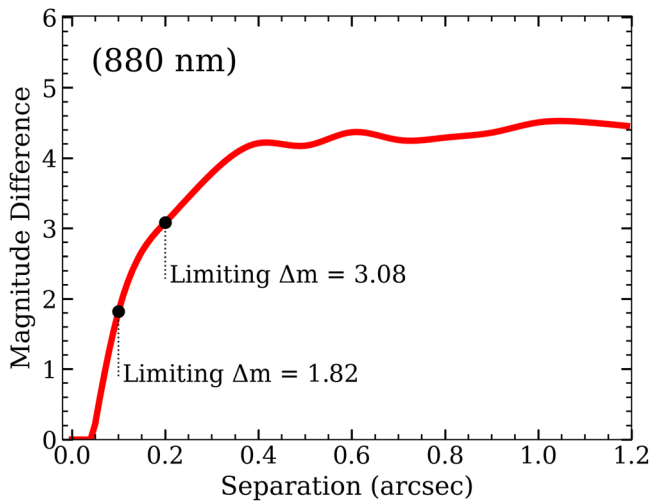


Figure 13. An example speckle detection limit curve from the 880 nm channel of QWSSI on LDT for 2MA 0201+0117 A is shown. No new unresolved companions were found for this star, to limiting magnitude differences (Δm) of 1.82 mag at $0''.1$, 3.08 mag at $0''.2$, and 4 mag or more beyond $\sim 0''.3$. A $0''.1$ separation corresponds to 4.93 au at the stellar distance of 49.3 pc.

the N. J. Wright et al. (2011) τ_{conv} relation is built upon a sample with poor mass estimates in the fully convective regime—our underplotted FC sources from N. J. Wright et al. (2011) likely include many interloping PC M dwarfs as a consequence.

While this means care should be taken to only compare our twins within a pair and not across different types of M dwarfs without considering mass, the qualitative appearance of the saturated and unsaturated regimes is still evident enough for general comparison. The most striking result in Figure 14 is again that of NLTT 44989 AB, where B appears on the lower envelope of the saturated sequence while A is well evolved toward the unsaturated, slowly rotating inactive clump. The right side of Figure 14 shows $H\alpha$ versus L_X , where a twin star appearing more active in $H\alpha$ is always the more active component in L_X as well (i.e., all lines trend diagonally upward)—this broadly agrees with the comparison field M dwarf results from J. G. Doyle (1989). In the case of GJ 1183 AB, the three different Chandra epochs do overlap in L_X for A and B, but for each specific epoch, A is always larger in L_X than B (see Figure 12).

We plot the remaining combinations of L_X , $H\alpha$ EW, P_{rot} , and rotation amplitude (peak-to-peak Δ) against each other in Figure 15. Here it can be seen that unlike for $H\alpha$ and L_X , the amplitudes of magnitude changes during rotation do not always track with other activity parameters. This agrees with existing results from other works that demonstrate photometric rotation amplitudes are generally less consistent tracers of absolute magnetic activity compared to other activity indicators (e.g., E. R. Newton et al. 2017), even when observed simultaneously with other metrics (A. García Soto et al. 2023). The photometric rotation amplitudes *are* always larger in our A components than B components, but only weakly so for NLTT 44989 AB—it remains unclear if this is a robust result or if the low number of three true twin systems randomly appeared this way given the changeable nature of spot modulation amplitudes. The trend is especially uncertain given the A and B component labels may not perfectly track which component is truly slightly more massive or not, as different magnitude measurements sometimes swap which star is brighter (see Section 2, Table 2, and Section 7.1.5). This

primary component rotation amplitude trend will be explored with more twin systems in our forthcoming second paper (A. A. Couperus et al. 2024, in preparation).

6. Additional System Notes

Here we provide further system-specific details for each pair, including any additional insights into the activity, rotation, ages, or multiplicity.

6.1. GJ 1183 AB

Both components are slightly elevated above the main sequence, as shown in Figure 1, indicating that the stars may be young. However, our analysis with BANYAN Σ found no reliable membership for the system in nearby young associations (see Section 2). Our speckle search, high-resolution lucky imaging work by M. Cortés-Contreras et al. (2017), and our RVs from the CHIRON spectra revealed no additional components.

$H\alpha$ indices (defined as $F_{H\alpha}/F_{\text{cont}}$) of 12.42 for A and 6.22 for B were measured for the pair during 1993–1994 by I. N. Reid et al. (1995). Stronger $H\alpha$ emission from A is consistent with our own mean EW results of A at -8.05 \AA and B at -6.37 \AA , so the activity differences we find were evident nearly three decades ago. This could either be due to sustained differences over those three decades, or from varying activity strengths due to underlying activity cycles, as indicated in our long-term photometry of the system seen in Figure 5—flares in the I. N. Reid et al. (1995) measurements are a possibility as well. This system was also observed for $H\alpha$ EWs by E. K. Pass et al. (2024), who found $A = -9.067 \pm 0.057 \text{ \AA}$ and $B = -9.289 \pm 0.057 \text{ \AA}$ from $R = 3000$ FLWO-FAST spectra. Our CHIRON measurements with $R = 27,000$ from seven epochs spread over 2.1 yr were taken earlier in time, yielding $H\alpha$ EWs of -7.65 \AA to -8.57 \AA for A and -5.61 \AA to -6.84 \AA for B, somewhat lower than the P24 results. These discrepancies may be due to systematic factors caused by different spectral resolutions and methods in determining EWs, or perhaps P24 captured stellar flaring events given both stars are quite active.

GALEX reports UV magnitudes for the stars that are consistent within the errors between components (A: FUV = 20.53 ± 0.25 NUV = 19.20 ± 0.10 , B: FUV = 20.46 ± 0.25 NUV = 19.38 ± 0.11 ; L. Bianchi et al. 2017), which could indicate similar activity levels in the UV. However, the FWHMs reported for the FUV and NUV sources range from $5''.2$ – $12''.4$, compared to the AB separation of $13''.07$, so some blending is likely. Radio detections were also found for GJ 1183 A by J. Pritchard et al. (2024), supporting the potential for future radio activity investigations of the pair.

GJ 1183 A was captured emitting two tremendous flares during our observations: the first in V at the 0.9 m where the star was seen about 2.6 magnitudes brighter than usual before dimming by 1.7 mag over 30 minutes (this flare is excluded from the 0.9 m light curves shown here in Figures 5 and 6), and the second in $H\alpha$ with an EW of -15.03 \AA compared to the average EW of -8.05 \AA . The absence of comparably strong events in GJ 1183 B is not conclusive evidence for activity differences given the random nature of flares, but GJ 1183 A is clearly an extremely magnetically active star.

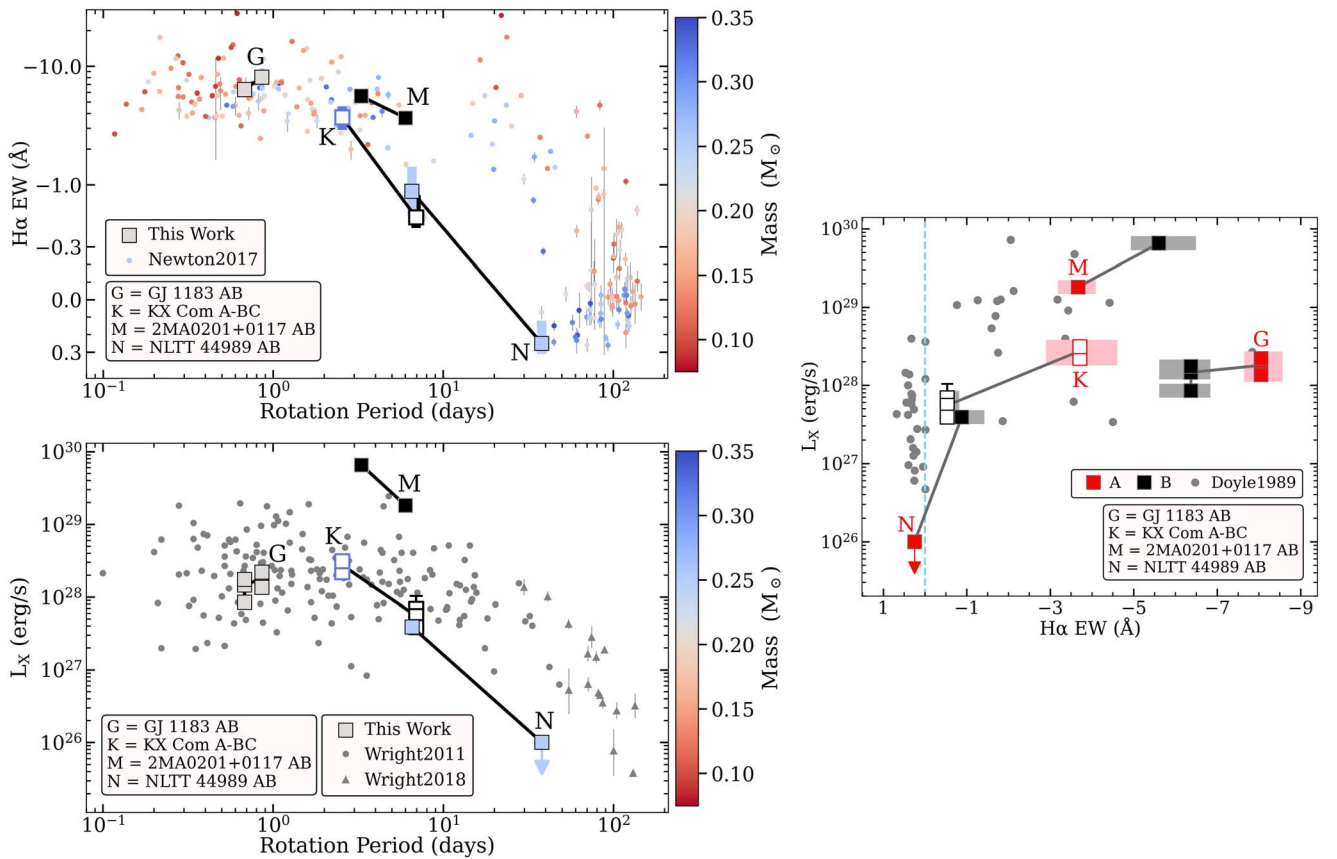


Figure 14. In each panel, stars studied here are represented by squares and lines connect components in a pair. Open squares indicate components A and BC in the non-twin triple KX Com. (Top left)— P_{rot} vs. H α EW, with fully convective stars ($M < 0.35$) from E. R. Newton et al. (2017) underplotted. All points for bona fide twins are color coded by mass except our stars that have less reliable mass estimates, shown in black. Bars on the squares for the stars studied here show the range of observed H α values for each star, excluding flares or epochs without A and B observed back-to-back. System letter labels are placed next to the A components in each pair. (Bottom left)—The same as above, now with L_X and underplotting fully convective stars from N. J. Wright et al. (2011) and N. J. Wright et al. (2018). An arrow indicates the upper limit in L_X for NLTT 44989 A (Section 3.4.1). The multiple Chandra epochs for GJ 1183 and KX Com are shown with multiple connected points. (Right)—H α EW vs. L_X , again showing the observed H α ranges as shaded bars and multiple connected points for the multiple Chandra visit cases. Underplotted gray points show field M dwarfs from J. G. Doyle (1989) for comparison. The vertical dashed blue line at EW = 0 divides active emission and inactive absorption stars. An arrow again indicates the upper limit in L_X for NLTT 44989 A. Overall, among twin pairs, strong H α emission is correlated with high L_X , and each of those observables is correlated with fast rotation.

6.2. KX Com A-BC

The KX Com system is not a true twin pair but rather an A-BC triple, where we find C to be a close companion to B using RVs, as discussed in Section 4.3.2. This system was also recently observed and discussed in detail by E. K. Pass et al. (2024), who use the alternate name LDS 942 from W. J. Luyten (1969). Care must be taken as the components labeled A and B are swapped between their work and ours—we find “A-BC” that P24 reported as “AC-B,” but we use our naming convention in the following text. The $R = 44000$ TRES spectra from P24 overlap in time with our CHIRON spectra, and SB2 behavior for BC is evident in both sets of spectra. Their data enabled a robust orbital fit for BC and yielded $P_{\text{orb}} = 25.274 \pm 0.016$ days; they estimated masses of $0.23 M_{\odot}$ and $0.20 M_{\odot}$ for the close binary components. This result is consistent with the $P_{\text{orb}} \gtrsim 24$ days lower limit we determined and indicates our own data very nearly wrapped the orbit. KX Com A did not display any close-in additional companions in Robo-AO high-resolution imaging by M. Ansdell et al. (2015), in agreement with our speckle and RV results and the RV results of P24. The KX Com B component was observed with high-resolution lucky imaging by M. Janson et al. (2012), who did not detect the very close C component and found no additional companions.

P24 reported H α EWs of -4.15 \AA and -4.52 \AA from TRES and FAST spectra, respectively, for the more active component we call KX Com A, consistent with the range of H α variability of -2.90 \AA to -4.61 \AA we observed over 1.2 yr. We see H α ranging from -0.43 \AA to -0.82 \AA in our blended KX Com BC results, in general agreement with P24’s median measure of -0.83 \AA or -0.78 \AA depending on the spectra they considered. P24 were able to ascribe this emission to KX Com B with the C component appearing flat in H α . Our X-ray results also align with H α , finding KX Com A is much more active than BC.

P24 suspected the 2.55 day rotation period in TESS belongs to KX Com A, which we have confirmed in our analysis here using higher-resolution 0.9 m data (Section 4.2). We also find a period of 6.93 days in our 0.9 m photometry of KX Com BC, which we presume belongs to the H α active B star and not the H α inactive C star, with C having an unknown and likely even longer third period. While the B and C component mass estimates are similar at $0.23 M_{\odot}$ and $0.20 M_{\odot}$, they could still display a strong rotation mismatch akin to the one we observe in NLTT 44989 AB. Rotational spindown in FC M dwarfs in general—and the various factors that could deviate spindown between otherwise twin stars—are discussed later in

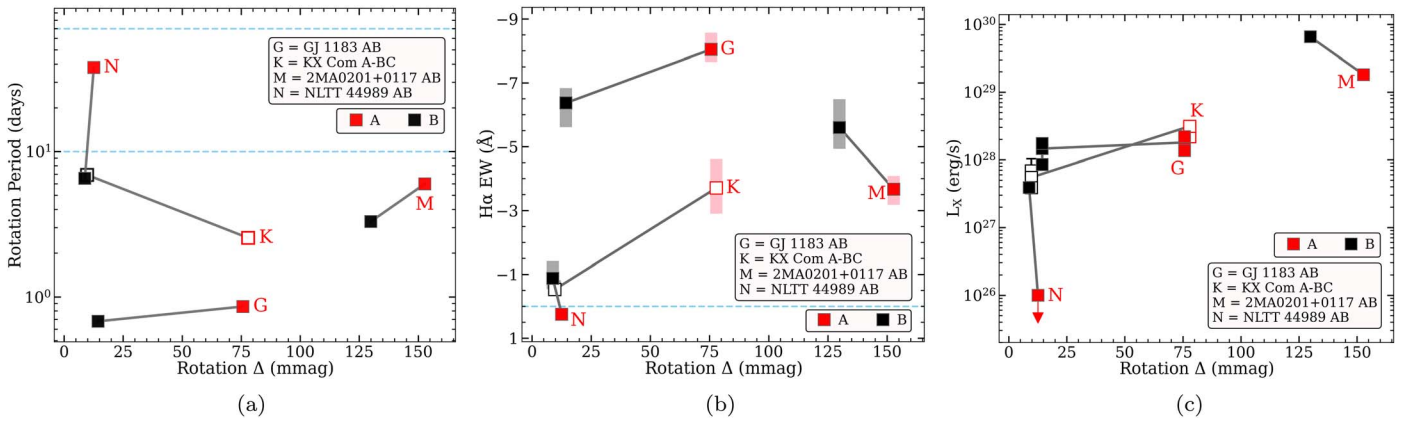


Figure 15. The 0.9 m V -band rotation amplitudes (peak-to-peak Δ) vs. (a) the rotation period, (b) H α EW, and (c) L_X . Lines connect the A (red) and B (black) components in a pair, with open squares indicating the non-twin triple KX Com A-BC. Overall, no clear correlations are seen. Blue horizontal dashed lines in panel (a) at 10 and 70 days bound the approximate region of intermediate rotation periods where few FC M dwarfs are found (E. R. Newton et al. 2018). The blue horizontal dashed line in panel (b) at EW = 0 marks the approximate transition between active H α emission and inactive H α absorption. Shaded red and gray bars in panel (b) are the ranges of observed H α EW values for each star, excluding flares or epochs without A and B observed back-to-back. Stars in panel (c) with three vertically stacked connected points show the three epochs of Chandra L_X measurements in those cases. An arrow in panel (c) indicates the upper limit in L_X for NLTT 44989 A.

Sections 7.2 and 7.1, but KX Com A-BC may also have dynamical triple-star interactions further disrupting the rotation and orbit angular momentum evolution of the entire system (C. Felce & J. Fuller 2023). Further observations to confirm our 6.93 day rotation period in B and find the presumably longer rotation period in C could help elucidate the role these dynamical interactions play in hierarchical triple spindown.

Following the rotation periods, it is noteworthy that the slightly more massive single-star component, KX Com A, is more magnetically active in H α and L_X than the lower-mass, binary KX Com BC components; this phenomenon was noted by P24 as well. Traditional expectations are that close-in companions will tidally interact to sustain rapid rotation and high levels of activity beyond typical active lifetimes. However, the 25 day orbital period for BC from P24 is much longer than the 6.93 day brightness modulation pattern we see in the component’s 0.9 m light curve and the ~ 7 days tidal circularization timescale of M dwarfs (E. Vrijmoet 2023), indicating B and C are not in tidal synchronization. This may be the result of the aforementioned dynamical interactions of hierarchical triples as discussed in C. Felce & J. Fuller (2023).

6.3. 2MA 0201+0117 AB

Both components in this system are elevated well above the main sequence, as shown in Figure 1. This is the only twin system in this paper with an age estimate, in this case because it is a member of the 25 Myr old β Pictoris association (F. J. Alonso-Floriano et al. 2015; S. Messina et al. 2017a). This means the $\sim 2\times$ difference we find in component rotation periods is likely a result of their formative rotation periods and disk lifetimes, having more connection to rotation starting points than our other twins that have had more time to evolve.

6.4. NLTT 44989 AB

Of the several different known twin or near-twin systems with active/inactive mismatches found throughout the combination of this work, E. K. Pass et al. (2024), and H. C. Gunning et al. (2014), NLTT 44989 AB is the only case with measured rotation periods for both components. The periods themselves

also confirm that the enormous activity differences we see in H α and L_X are aligned with strongly mismatched rotation in this case. To the best of our knowledge, we are the first to report rotation and activity measurements for each component in this fascinating twin system. Furthermore, no additional companions were uncovered for NLTT 44989 A or B from two speckle visits (Sections 3.5, 4.5), our 15 RV epochs over 1.5 yr (Figure 11), or various other related checks (Section 2.1), supporting their twin nature.

Both components reside toward the lower edge of the main sequence (see Figure 1), possibly implying an older age or lower metallicity for the pair compared to the other three systems—this is in agreement with NLTT 44989 A hosting the longest rotation period here as well. We do not find any reported UV sources for the system in L. Bianchi et al. (2017), but GALEX images of the field clearly show elevated counts near B and minimal counts near A, commensurate with our other activity signatures. Deeper studies of the UV activity are left for future work.

The system resides in a dense field, with particular care needed to assess potential contamination in any future observations—this is especially important for long-term campaigns where proper motion may become relevant as well. The contaminating sources are much fainter in the optical (see Section 3.6 for a discussion of this in our own observations), but even these small deviations could be relevant for validating and interpreting results for the system, such as we discuss later in Section 7.1.5.

7. Discussion

Here we focus on only the three true twin systems, GJ 1183 AB, 2MA 0201+0117 AB, and NLTT 44989 AB, and disregard KX Com A-BC because of its non-twin nature. See Section 6.2 for a separate discussion of KX Com A-BC.

7.1. Observed Differences and Possible Causes

We observe consistent activity differences in H α and L_X beyond the uncertainties in each twin pair case. The most modest of these is GJ 1183 AB, where A is $58\% \pm 9\%$ stronger

in L_X on average¹⁹ over three visits and $26\% \pm 9\%$ stronger in $H\alpha$ EW on average over seven visits. GJ 1183 A and B host functionally similar rotation periods of 0.86 day and 0.68 day—these both fall in the saturated regime, and we indeed see both stars similarly located in the rotation–activity plane in Figure 14. 2MA 0201+0117 AB demonstrates the next largest set of differences, with B 3.6 ± 0.5 times stronger in L_X from one visit and $52\% \pm 19\%$ stronger in $H\alpha$ on average from nine visits. This trend follows the rotation given that B is faster at 3.30 days compared to A at 6.01 days, a difference likely resulting from formation and disk evolution given the young ~ 25 Myr age for this β Pic association system. Finally, NLTT 44989 AB shows the strongest differences, with $B \geq 39 \pm 4$ times stronger in L_X , ~ 6 times faster in rotation period, and a complete A/B inactive/active mismatch in $H\alpha$ for 15 visits over 1.5 yr. In every system’s case, these differences are all despite component stars having the same mass, age, composition, and environment.

We next provide brief evaluations of the plethora of possible causes for the observed activity and rotation differences between components within these three twin systems. The potential causes are separated into characteristics of the stars themselves (Sections 7.1.1–7.1.5), effects of companions past or present (Sections 7.1.6–7.1.9), or purely observational consequences (Sections 7.1.10–7.1.12). We begin with the most straightforward explanation.

7.1.1. Could Different Rotation Periods Be Causing the Different Activity Levels?

Different rotation speeds are the obvious explanation for our observed activity differences, and higher activity levels generally track with faster rotation periods in our results (Figure 14). That said, this produces the obvious follow-up questions: *why* are the rotation periods different? And, how well can we predict rotation periods and activity levels? We primarily address these questions later in Sections 7.2 and 7.3, though some of the enumerated factors considered next are relevant to rotation evolution as well.

7.1.2. Could the Observations Be Snapshotting Stellar Activity Cycles?

Even if components have exactly the same rotation periods, out-of-phase stellar cycles could still manifest different levels of observed activity between otherwise twin stars at a snapshot in time. Long-term stellar activity cycles are known or strongly suspected to exist in a number of PC and FC M dwarfs (e.g., L. N. Mavridis & S. Avgoloupis 1986; P. Robertson et al. 2013; M. Route 2016; A. Suárez Mascareño et al. 2016; B. J. Wargelin et al. 2017; T. J. Henry et al. 2018; R. V. Ibañez Bustos et al. 2019a, 2019b, 2020; J.-F. Donati et al. 2023; B. Fuhrmeister et al. 2023; Z. A. Irving et al. 2023; A. A. Couperus et al. 2024, in preparation; L. T. Lehmann et al. 2024, and references therein). We even observe a candidate long-term photometric cycle in GJ 1183 A, in contrast to much lower-amplitude changes in B over a decade

baseline (Figure 5). That said, the activity differences between A and B may be the manifestation of even longer timescale stochastic variations in the dynamos as stellar cycles change in time—for example, B could be in a Maunder Minimum–like low-spot-activity state in contrast to A (J. A. Eddy 1976).

Beyond cycles seen via optical photometry, X-ray activity cycles also exist in some stars, including a candidate X-ray cycle in the FC M dwarf Proxima Cen (B. J. Wargelin et al. 2017). Theoretical work by A. O. Farrish et al. (2021) suggests that such cycles in M dwarfs cause variability in L_X/L_{bol} throughout spindown. Observationally, the long-term variability scatter in L_X for M dwarfs is about a factor of 2 for most stars, according to the results of E. Magaudda et al. (2022; see their Figure 13). D. Dsouza (2023) and N. Ilić et al. (2023) found a comparable level of scatter in L_X between similar components in M dwarf wide binaries. Similar behavior is also observed in the twin M dwarf system GJ 65 AB, where work by S. Wolk et al. (2022) revealed that X-ray flaring activity levels changed moderately for one component compared to observations taken nearly two decades earlier. X-ray cycles may therefore play a role in the L_X differences we observe in GJ 1183 AB and 2MA 0201+0117 AB (see Section 4.4 for additional details), whereas NLTT 44989 A and B differ well beyond the typical scatter seen for field stars and beyond the level likely attributable to cycles alone (see Figure 14).

Long-term cycles in chromospheric $H\alpha$ activity have also been found for M dwarfs, with a few such example cases reported in J. Gomes da Silva et al. (2011), P. Robertson et al. (2013), and B. Fuhrmeister et al. (2023). However, the expected amplitudes of the variations in $H\alpha$ EW for different FC M dwarfs are too poorly understood to offer robust constraints for informing our differences here. While there is $H\alpha$ EW scatter of up to several angstroms in low-mass field stars (see Figure 14), it is unclear what proportion of this variability may be caused by cycles, and a significant portion is likely from very short-term variability (see, e.g., K. J. Bell et al. 2012; H. C. Gunning et al. 2014; A. A. Medina et al. 2022a). It suffices to say that activity cycles may be partially responsible for some amount of the differences we see in $H\alpha$ EW between twin components, though again not in the extreme case of NLTT 44989 A/B, where a total inactive/active mismatch is seen.

7.1.3. Could a Dynamo Bistability Exist in Some M Dwarfs?

Beyond observational snapshotting, the magnetic dynamos themselves may host underlying instabilities. Theoretical work by T. Gastine et al. (2013) has suggested the possibility of a double-branched dynamo regime wherein late M dwarfs could fall into one of two dynamo states depending on the initial parameters. If a dynamo bistability exists, our twins may have had similar initial parameters but could have converged to two different dynamo states for some unknown duration, resulting in the mismatched activity and/or rotation we see today. In contrast, L. L. Kitchatinov et al. (2014) again implicated oscillatory stellar cycles to explain the underlying observations. Overall, we generally favor the explanation of oscillatory cycles given the growing observational and theoretical evidence for such stellar activity cycles in fully convective M dwarfs (e.g., M. Route 2016; A. Suárez Mascareño et al. 2016; R. K. Yadav et al. 2016; T. J. Henry et al. 2018; B. P. Brown et al. 2020; R. V. Ibañez Bustos et al. 2020; J.-F. Donati et al. 2023; B. Fuhrmeister et al. 2023; Z. A. Irving et al. 2023;

¹⁹ Relative differences in L_X and $H\alpha$ are calculated using simple ratios between components and standard uncertainty propagation techniques. L_X used the larger of the asymmetric errors for propagation, the upper limit in L_X with no error for NLTT 44989 A, and a weighted average of the three L_X visits for GJ 1183 AB. $H\alpha$ used the mean and standard deviation of EWs for each star, only including nonflaring epochs with both stars successfully observed back-to-back.

A. A. Couperus et al. 2024, in preparation; L. T. Lehmann et al. 2024, and references therein). This is also supported in our own data here given the candidate photometric cycle in GJ 1183 A (Figure 5). However, separate observational X-ray activity results from B. A. Cook et al. (2014) and E. Magaudda et al. (2024) support the presence of a bimodal dynamo in very-low-mass very-rapidly rotating stars, so this factor ultimately remains a possibility in some parameter regimes. Multiepoch Zeeman-Doppler imaging observations of our twins to reconstruct their magnetic field characteristics over cycle timescales would provide very strong evidence to investigate this further.

7.1.4. Could Metallicity Be Changing the Activity and Rotation?

Stellar activity can change with composition (i.e., metallicity), as shown in the results of V. See et al. (2021). Different metallicities could result in discordant rotation periods via different amounts of activity and subsequent magnetic braking over evolutionary timescales. However, our twins should have functionally identical compositions as members of the same wide binaries, as supported by the work of K. Hawkins et al. (2020), who found that wide binary components typically have $[\text{Fe}/\text{H}]$ matched to within 0.02 dex. Future work yielding detailed abundance measurements from our spectra could validate this assumption, but for now we note that no significant differences have been seen when inspecting overlapping spectra for components in the twin systems, see, e.g., Figure 10.

7.1.5. Could Slightly Different Component Masses Be Responsible?

Our selection for pairs being equal-mass is exclusively based on requiring BP, RP, J , H , and K_s to all match within <0.10 mag between components. Differences of 0.1 mag would correspond to slightly different masses and subsequently mildly deviated spindown timescales, possibly explaining any activity or rotation mismatches in our pairs, so we attempt to quantify this. The three true twin pairs here have an average difference of 0.04 mag between components across all five required filters, with estimated masses for A and B always differing by $<0.005M_\odot$ if we consider precisions higher than reported in Table 2. The G. F. Benedict et al. (2016) M_V MLR we use has an rms scatter of 0.19 mag or $0.023M_\odot$, so we are functionally at or within the MLR precision limits. E. K. Pass et al. (2024) calculated that a $0.02M_\odot$ difference would yield a 3.86% chance of observing a roughly twin binary pair during an active/inactive mismatch in their results due to just mass-dependent spindown. We observed 27 of our twin systems for $H\alpha$ activity, 25 if we remove the two known or suspected higher-order multiples, and found only NLTT 44989 AB had an active/inactive mismatch (A. A. Couperus et al. 2024, in preparation). This represents $1/25 = 4\%$ of our systems, very similar to the E. K. Pass et al. (2024) estimate, so we cannot rule out very slight mass differences as a possible explanation for NLTT 44989 AB. Furthermore, the NLTT 44989 B BP measurement we use for our mass estimate has up to $\sim 6.3\%$ extra contaminating flux from background sources (Section 3.6.1 and Figure 4), which, if removed, shifts B about 0.066 mag farther from A in terms of brightness (but still within the MLR scatter level), possibly favoring the slight mass difference explanation for this system specifically.

Despite this possibility, the present mass estimates we do have for NLTT 44989 A and B differ by only $0.0017M_\odot$, giving a much lower 0.33% chance to be observed with an active/inactive mismatch by chance from just mass-dependent spindown based on Equation (3) in E. K. Pass et al. (2024), so we disregard this factor for the remainder of the discussion and treat them as true twins. Higher-precision MLRs or mass measurements for our twins, or a larger sample of twins, would allow us to investigate this further.

7.1.6. Could Nonstandard Evolutionary Scenarios Explain NLTT 44989 AB?

It is worth considering if the extreme case of NLTT 44989 AB is a complex outlier. While we assume our binary components are the same age and formed together, we cannot strictly rule out the possibility that two stars with similar masses and compositions in a binary have different ages because of dynamical many-star interactions in the distant past (e.g., M. Valtonen & S. Mikkola 1991; K. M. Kratter 2011, and references therein). Another extreme possibility is past mass transfer from more-massive companions followed by the smaller low-mass star(s) subsequently being ejected via dynamical interactions—past stellar mergers could play a similar role (e.g., A. J. Frost et al. 2024). These scenarios are somewhat analogous to blue stragglers (e.g., P. J. T. Leonard 1989; F. R. Ferraro et al. 2006; M. Mapelli et al. 2006; R. Di Stefano 2011) but now hypothetically appearing in leftover low-mass stars. In these scenarios, we might expect different compositions between the components, which could be tested with a detailed abundance analysis of our spectra. We leave this for future work, and again simply note the extremely congruent overlapping continuum features in Figure 10 as evidence favoring similar compositions.

The strong activity level mismatch in NLTT 44989 AB has similar counterparts in $H\alpha$ activity found by E. K. Pass et al. (2024) and H. C. Gunning et al. (2014), as well as the results for BL+UV Ceti outlined in Section 1. While these binaries may all have such complex evolutionary histories that invalidate their twin natures, we consider this scenario highly unlikely in light of the more probable alternate explanations available involving spindown properties of FC M dwarfs, as discussed in Section 7.2 below.

7.1.7. Could There Be Dynamical Binary Interactions at Play?

Even assuming our stars formed together and are the same age, they may still be dynamically interacting in ways distinct from isolated stars. Our systems are presently in wide >80 au configurations, so this should generally not be the case. However, it is important to consider the possibility of the duplicity interfering with disks during formation, which could result in shorter disk lifetimes or otherwise impact star-disk rotational coupling and subsequently produce different stellar rotation periods. The rotation differences could then propagate and, depending on the age of the stars, remain today, resulting in both rotation and activity differences. Various efforts have found that these disk disruptions can occur in wide binaries out to component separations of ~ 80 – 100 au (e.g., E. L. N. Jensen et al. 1996; S. Meibom et al. 2007; L. A. Cieza et al. 2009; R. J. Harris et al. 2012; S. Messina et al. 2017a; S. Messina 2019; S. S. R. Offner et al. 2023), even in low-mass M stars. GJ 1183 AB and 2MA 0201+0117 AB have projected

separations well beyond this limit, at 229 au and 515 au, respectively, but NLTT 44989 A and B are closer at 87 AU. This means that disk disruption effects may be at play in the NLTT system, though the true separation is likely larger than the projected value. The two stars are functionally the same in mass as well, so could hypothetically have somewhat equal and opposite impacts on each other's disks. However, the extent to which twin M stars form with twin disks is not well informed, so future studies examining disk architectures of twin PMS M stars would prove insightful.

Secondarily, K. El-Badry et al. (2019) and H.-C. Hwang et al. (2022) proposed that an excess population of twin wide binaries may form close together via circumbinary disk accretion with subsequent dynamical widening to their present-day wider separations—we conjecture that this could hypothetically alter the initial rotation periods or early rotational evolution of our twin binary stars compared to isolated single stars. This twin excess fraction appears stronger at masses $<0.6M_{\odot}$ and extends out to binary separations of $\sim 10,000$ au (K. El-Badry et al. 2019), covering a very large portion of our broader sample. Finding only our single case with strongly deviated behaviors may therefore disfavor this hypothesis, but a robust statistical comparison of our sample against the results of K. El-Badry et al. (2019) is needed to investigate this hypothesis further. We leave this as future work given the significant uncertainty in how much this formation pathway would or would not disrupt the long-term rotational evolution of a given pair.

7.1.8. Could There Be Hidden Unresolved Companions?

Higher-order multiplicity beyond simple duplicity is also a concern. Any relatively massive unresolved companions, be they black holes, neutron stars, white dwarfs, red dwarfs, or brown dwarfs could break our twin comparisons and possibly explain any observed differences in either rotation or activity. We have tried to rule out this scenario as much as possible using speckle imaging (Section 4.5), time series RVs (Section 4.3.2), various Gaia parameters (Section 2.1), and literature checks (Sections 2.1 and 6), all of which uncovered no additional companions to our three true twin systems. We also do not see clear evidence for intermixed photometric patterns in our resolved 0.9 m data (Figures 5 and 6) that could suggest multiple blended stars, if they existed. That said, there are regions of parameter space not ruled out, such as a close-in companion orbiting at less than ~ 0.7 au (the SOAR and LDT ~ 40 mas speckle limits at the closest distance case of GJ 1183 B) in a face-on configuration that would result in no detectable RV signature. Unresolved sources could also have combined brightnesses that might not appear obviously elevated on the main sequence, or be similar brightness and thus less identifiable via the Gaia RUWE value. Altogether, while we cannot entirely disregard these various possibilities, we consider unseen massive companions relatively unlikely given our multifaceted investigation.

7.1.9. Could Exoplanets Orbiting the Stars Change the Stellar Behaviors?

Beyond hidden massive companions, planets could also drive mismatches, either via disk disruptions during formation or from star–planet interactions. In the former, planets could hypothetically impact the lifetime of a circumstellar disk and

the subsequent star–disk-locking duration, thereby possibly changing the rotation period at which a star forms and the consequent period we see today. For the latter, be they tidal or magnetic star–planet interactions, there is evidence to suggest impacts on the stellar rotation and/or activity are possible and observable (e.g., G. Privitera et al. 2016; N. Ilic et al. 2022; J. S. Pineda & J. Villadsen 2023; C. Triglio et al. 2023; E. Ilin et al. 2024). Finally, in an extreme case, past planetary mass transfer or complete engulfment into the host star could also disrupt the stellar rotation (J. Guillochon et al. 2011; B. D. Metzger et al. 2012). While low-mass M dwarfs host very few massive planets (E. M. Bryant et al. 2023; T. Gan et al. 2023; E. K. Pass et al. 2023b), a rare case might be the reason we only found a single case with significant rotation mismatches among our 13 twin systems with rotation results (A. A. Couperus et al. 2024, in preparation). Furthermore, stars with stellar companions (such as our binary targets) are actually one of the possible explanations responsible for dynamically placing gas giants very close in around M dwarfs (see, e.g., C. I. Cañas et al. 2023, and references therein). Overall, the extent and timescale of these various planetary effects on the host star are active areas of investigation and depend heavily on the system configuration (e.g., Y. Wu & N. Murray 2003; J. Guillochon et al. 2011; B. D. Metzger et al. 2012; C. Petrovich 2015).

This all implies a significant result—if planet interactions with the disk/star cause detectable disruptions in stellar spindown, this could enable the discovery of planets based on spin comparisons in the future. Future work obtaining higher-precision RV observations of NLTT 44989 A and B to determine if one has a massive close-in planet while the other does not would be valuable to investigate these hypotheses.

7.1.10. Could the Stars Have Different Rotational Inclinations?

Observational viewing angles are relevant because inclinations can significantly alter spot modulation amplitudes. This could explain the mismatched long-term photometric activity levels in GJ 1183 AB (Figure 5), but in this case, P_{rot} and $v \sin(i)$ are similar for A and B, and with similar twin radii, so we thus do not expect their inclinations to differ markedly. Mismatched inclinations also cannot explain the cases we find with different rotation rates, except for specific spot configurations as discussed next in Section 7.1.11. L_X and $H\alpha$ emission from active stars are largely the result of distributed magnetic heating in the chromosphere and corona, and they are therefore generally treated as largely independent of inclination. The role of inclination may be significantly more important in the context of theoretical results by B. P. Brown et al. (2020) that demonstrated dynamo action strongly manifesting in a single hemisphere when fully convective M dwarfs are modeled; these results remain to be verified observationally, but if correct, would have remarkable implications for studies of FC M dwarf activity.

7.1.11. Could Specific Spot Configurations Be Changing Our Measured Rotation Periods from the True Periods?

Spots rotating in and out of view can be an imperfect technique for measuring periods in certain cases, creating yet another observational effect related to viewing angle. Our measured rotation periods could be impacted by similar spot configurations on opposite sides of the stars manifesting

similar-amplitude modulations; these would masquerade as a periodic pattern twice as fast as the true rotation period (see recent examples of this for TESS data in S. Raetz & B. Stelzer 2024). This effect can only produce periods appearing falsely faster, primarily twice as fast, but not slower, assuming spot configurations do not change rapidly relative to the rotation timescales. So, if this case were occurring, the true rotation periods of our stars would be about double the duration of our measured periods.

GJ 1183 A and B have measured periods of 0.86 days and 0.68 days, where either doubling would still result in periods broadly similar and in the very active regime. In 2MA 0201+0117 A and B, we measured 6.01 and 3.30 day periods, respectively, where doubling B's 3.30 day period would repair their factor of ~ 2 difference. For NLTT 44989 A and B with adopted periods of 38 days and 6.55 days, respectively, doubling the shorter 6.55 day period to 13.10 days would still present a marked mismatch in rotation, and the two stars would still appear in different active/inactive regions of the rotation–activity diagrams in Figure 14. The impact on our overall results would therefore be relatively minor; the interpretation of GJ 1183 AB would not markedly change, 2MA 0201+0117 AB might no longer suggest different rotation during ongoing formation, and our most important result of NLTT 44989 AB would have the same general interpretation. The $H\alpha$ and L_X activity differences in each pair would also be unaffected.

We cannot entirely rule out these spot configuration possibilities, but we consider them quite unlikely given our multiple data sources from distinct and sometimes multiyear spans in time that often recover very similar periods for many of our stars (see Section 4.2). Longer baseline observations that allow time for spot configurations to change could investigate this further.

7.1.12. Could Distant Background Sources of Impactful Brightness Be Lurking Directly behind Our Stars?

There could also be contamination from astrophysically unassociated sources distinct from unseen orbital companions. Background sources more distant than our stars but of considerable brightness—such as evolved luminous stars, high surface brightness galaxies, or active galactic nuclei—would corrupt our results if aligned on the sky with our stars during our observations. Nearby contaminants assessed with Gaia are discussed in Section 3.6, and our speckle observations probe even closer to $\lesssim 0''.1$, but that still leaves area directly behind the stars unexplored. However, this possibility can be assessed in all cases because the pairs have large proper motions of $70\text{--}367\text{ mas yr}^{-1}$ that substantially change the sky positions over human timescales. Our visual assessment used archival images within Aladin from DSS2-Red (Ep. 1984–1998; B. M. Lasker et al. 1996; R. R. Gal et al. 2004), SkyMapper R-band (Ep. 2014–2015; C. Wolf et al. 2018), and ZTF DR7 r-band (Ep. 2018–2021; F. J. Masci et al. 2019), finding that at the epochs of our new observations, the pairs are not directly overlapping with any bright background sources to the extent the proper motions allow us to check (except the cases already discussed for NLTT 44989 AB in Section 3.6). In addition, the general astrophysical behaviors of the stars in our observations are consistent with that of pre- or main-sequence M stars, instead of, for example, active galactic nuclei.

7.2. Implications for Fully Convective M Dwarf Spindown

Considerable progress has been made in recent years toward understanding the spindown of fully convective M dwarfs (e.g., T. M. Brown 2014; E. R. Newton et al. 2016, 2017; C. Garraffo et al. 2018; E. R. Newton et al. 2018; A. A. Medina et al. 2022b; E. K. Pass et al. 2022, 2023a, 2024; S. G. Engle & E. F. Guinan 2023; W.-C. Jao et al. 2023; A. Sarkar et al. 2023; Y. Lu et al. 2024). To summarize: the stars typically begin and stay relatively rapidly rotating at $P_{rot} < 10$ days for roughly 1–3 Gyr (A. A. Medina et al. 2022b; E. K. Pass et al. 2022), around 2.4 ± 0.3 Gyr undergo very rapid spindown during a phase of strong rotational braking (A. A. Medina et al. 2022b), are settled into slow rotation at $P_{rot} > 90$ days by 12.9 ± 3.5 Gyr (A. A. Medina et al. 2022b), and can ultimately reach periods at least as long as ~ 180 days (A. A. Medina et al. 2022b). The intriguing “fast braking phase” is supported by the observed dearth of field FC M dwarfs with intermediate 10–70 day rotation periods (E. R. Newton et al. 2016, 2017, 2018), which is visible in the top-left panel of Figure 14 as a clustering into two groups with $P_{rot} \lesssim 10$ days and $\gtrsim 70$ days. The starting age of the fast braking phase is primarily set by stellar mass, with lower-mass stars exhibiting a greater span between their fast and slow rotation distributions. However, there is clear variability to this overall process because some stars have spun down considerably by < 1 Gyr (E. K. Pass et al. 2022). This may be caused in part by different initial rotation periods, potentially the result of different birth environments (E. K. Pass et al. 2024). The fast braking phase is also possibly linked to elevated flaring and $H\alpha$ emission (N. Mondrik et al. 2019; E. K. Pass et al. 2023a), but little is known about magnetic activity in this transitional time period due to the paucity of targets within it. The transition between different rotational evolutionary stages may ultimately be driven by changes in stellar magnetic morphology and dynamo state, as described in C. Garraffo et al. (2018), though alternative discussions are given in V. See et al. (2019) and A. Sarkar et al. (2023).

The key result we find here is the case of NLTT 44989 A and B, where twin FC M dwarfs with the same age/mass/composition/environment present rotation periods of 38 days and 6.55 days, respectively, with correspondingly strong mismatches in L_X and $H\alpha$. Our favored explanation is that NLTT 44989 A has already begun and progressed a moderate amount through its fast braking phase, while NLTT 44989 B has either not yet begun or only minimally progressed into the phase. This explanation is supported by the positions of each star in the top-left panel of Figure 14, where we see B on the lower envelope of the saturated regime and A already far along its transition to the slowly rotating inactive clump. The position of B being noticeably below the activity level of other similar-mass and similar-rotation field stars suggests it may indeed have already begun its transition into the fast braking phase but not yet markedly slowed its rotation. However, the aforementioned possibility of elevated activity during the fast braking phase could contradict this—the evolving strength of different activity tracers throughout the entirety of the transition phase clearly needs more study. The lack of field stars in the region directly between A and B tracks with the form of the saturated regime and implies that B will maintain a similar (or potentially greater) $H\alpha$ emission strength while it spins down to $\sim 30\text{--}50$ days, after which its $H\alpha$ activity will decrease. Component A already lacks $H\alpha$ activity, comparable to the

similar-mass slowly rotating field stars, suggesting its $H\alpha$ activity will remain largely the same going forward as it spins down from 38 days toward ~ 100 days and beyond. The L_X activity for both stars will likely follow similar pathways.

Our case of NLTT 44989 AB is akin to the two recently reported FC M dwarf wide binary systems in E. K. Pass et al. (2024), whose components display mismatched active/inactive $H\alpha$ despite very similar masses.²⁰ These three (near) twin systems all exhibit strong differences in $H\alpha$, as well as in L_X and rotation in NLTT 44989 AB. Each case controls for the age, composition, and mass, implying that the spindown process is not a function of any combination of these factors exclusively; this is in agreement with the observed dispersion in spindown epoch at similar mass and age as discussed in E. K. Pass et al. (2022) and E. K. Pass et al. (2024). Scatter in rotation periods before and after the star–disk–locking phase (star–disk–locking; A. Koenigl 1991; S. Edwards et al. 1993) could play a significant role in setting stars’ future spindown evolution as well. High-energy environments at birth may impact disk lifetimes (M. Ansdell et al. 2017), and consequently, rotation rates (J. Roquette et al. 2021), but should not be a differentiating factor in these three binary systems. The observed activity and rotation differences must therefore be manifesting at least in part from some combination of (1) initial rotation periods changing by factors other than birth energy environment, e.g., disk sizes and/or masses, (2) a stochasticity in the onset of the fast braking phase, or (3) other unknown parameters relevant to overall spindown evolution.

There are no present-day observables that can reach back in time to pinpoint initial rotation periods for stars, but our twin cases provide some context. We find very similar periods of 0.86 and 0.68 day in GJ 1183 AB, and in our forthcoming paper, we will report results for several more twin systems having components with similar rotation periods (A. A. Couperus et al. 2024, in preparation). On the other hand, in 2MA 0201+0117 AB we see periods of 6.01 days and 3.30 days at ~ 25 Myr, so rotation periods can differ at a very young age—this is in agreement with the scatter in rotation M stars show in young clusters as well (e.g., R. J. Jackson & R. D. Jeffries 2010; M. Popinchalk et al. 2021). For example, some stellar components could have had more massive disks with longer disk lifetimes and disk-locking durations, leading to subsequently slower stellar rotation periods after contraction finishes. The spindown models of A. Sarkar et al. (2023) can reproduce the very different rotation periods of NLTT 44989 AB at a range of ages $\gtrsim 2.5$ Gyr if different configurations of initial period and disk lifetime are assumed for each $0.25 M_\odot$ component (see their Figure 5). However, these models still generally struggle to match the very long periods seen in low-mass field stars, as well as the E. K. Pass et al. (2022) results. Altogether, differences in initial rotation rates remains a plausible hypothesis to explain present-day differences.

We summarize that possible culprits for generating these spin mismatches in NLTT 44989 AB and 2MA 0201+0117 AB could be early formation factors as discussed above, dynamical binary disk interactions (Section 7.1.7), planetary impacts on the disk and/or host star (Section 7.1.9), or complex dynamo behaviors (Section 7.1.3). These are joined by several other less likely explanations considered throughout Section 7.1. We

recommend that the key follow-up investigations to continue disentangling these various possibilities are higher-precision RV exoplanet searches of NLTT 44989 AB, Zeeman-Doppler imaging magnetic reconstructions of NLTT 44989 AB and other twin FC M dwarf binaries with activity mismatches, and studies of disks in twin PMS M stars. Future work should also try to obtain a more precise measurement of the NLTT 44989 A rotation signal,²¹ as it potentially has a period even longer than we measured here giving an even stronger mismatch (see Section 4.2).

7.3. Implications for Exoplanet Host Activity Predictions

It is desirable to reconstruct the complete stellar activity history of a given exoplanet host star to help model the impacted planetary atmospheric evolution and evaluate habitability factors. This is especially true for M dwarfs, given that they host key candidates for exoplanet atmospheric characterization with existing and upcoming observatories, while also exhibiting significant stellar activity. Alas, our results highlight the ongoing challenges in modeling M dwarfs’ activity evolution. For example, one could know the precise age, mass, and composition of the components in NLTT 44989 AB but would still be unable to predict their present-day rotation periods to within a factor of ~ 6 , or their X-ray luminosities to within a factor of ~ 40 or more. The rotation difference in particular has significant implications for any attempts to apply gyrochronology in FC M dwarfs as well. Even if rotation periods are known and match, GJ 1183 AB indicates that intrinsic differences of at least $58\% \pm 9\%$ in L_X and $26\% \pm 9\%$ in $H\alpha$ can exist. Further muddying our interpretations of activity, these intrinsic scatters are derived from multiepoch observations of just the activity *now*, not a fully reconstructed average history. Our results alone do not determine if most FC M dwarfs typically deviate by these amounts, but do demonstrate that presumed twin stars can differ by at least this much.

There is also likely a phase around the rapid spindown epoch during which the scatter in initial rotation periods drives scattered spindown epochs for even equal-mass FC M dwarfs, thus resulting in a degraded ability to predict any small star’s rotation and activity within the fast braking time period. This claim is supported by E. K. Pass et al. (2024), who found a 1σ dispersion upper limit of 0.5 Gyr in otherwise mass-directed FC M dwarf spindown. It is therefore important to further investigate NLTT 44989 AB and similar mismatched systems to determine if they represent a phase all FC M dwarfs go through—perhaps briefly making it rare to see—or if they are complex outliers.

Efforts continue to gradually improve our understanding and ability to estimate activity over M dwarf stellar lifetimes, but for now it is clear that considerable caution should be employed for any exoplanet studies relying on activity reconstructions for specific FC M dwarf hosts, such as Proxima Cen or TRAPPIST-1.

8. Conclusions

We have presented newly acquired long-term light curves (Sections 3.1, 4.1), rotation periods (Sections 3.2, 4.2), $H\alpha$ EWs (Sections 3.3, 4.3.1), RVs (Sections 3.3, 4.3.2), X-ray

²⁰ One of these two systems is also in our full twins sample and will be included in our future paper.

²¹ *TESS* is planned to observe the NLTT 44989 AB system again in 2025 during sectors 91 and 92, aiding future studies.

luminosities (Sections 3.4 and 4.4), coronal parameters (Sections 3.4, 4.4), and speckle imaging observations (Sections 3.5, 4.5) for four fully convective M star twin wide binaries. We found one system, KX Com A-BC, to be a hierarchical triple, in agreement with the recent results of E. K. Pass et al. (2024)—the other three systems present as true twin binaries with the same age/mass/composition/environment. The main takeaways from this work are as follows:

1. We uncover consistent activity differences in L_X and $H\alpha$ for all three true twin pairs. NLTT 44989 A/B shows a remarkable inactive/active disagreement between components, while long-term stellar activity cycles may be influencing the relative strength of the observed mismatches in other cases.
2. In each twin pair, the component more active in L_X is also the more active star in $H\alpha$, while photometric rotation amplitudes do not always follow this trend.
3. NLTT 44989 AB has a strong rotation rate mismatch of 38 days versus 6.55 days, 2MA 0201+0117 AB has a moderate mismatch at 6.01 and 3.30 days, and GJ 1183 AB hosts similar rotation periods of 0.86 and 0.68 days.
4. The discrepant rotation periods and activity levels in NLTT 44989 AB likely stem from one component having begun and progressed moderately through its fast braking phase before the other, despite both components having the same age, mass, composition, and environment. We hypothesize that material interactions may be responsible, either through disk interference at formation producing very different initial stellar rotation periods or from longer-term star–planet interactions as the system has evolved.
5. GJ 1183 AB shows mismatched spot activity levels throughout a decade of photometry and demonstrates that twin FC M dwarfs with very similar rotation periods can still deviate in photometric variability properties, as well as in L_X and $H\alpha$ that differ by $58\% \pm 9\%$ and $26\% \pm 9\%$, respectively.
6. 2MA 0201+0117 AB is a PMS twin pair in the β Pictoris association that provides a valuable system for future theoretical comparisons. In particular, this system indicates that differences may be present in twin stars at a very young age of only ~ 25 Myr.
7. Overall, the differences found here for twin stars indicate that it is *very* difficult to anticipate the integrated historical environments provided by fully convective M dwarfs for any orbiting planets.

This work has considered four systems from our broader sample of 36 total systems that span the entire partially and fully convective M dwarf sequence. Rotation and activity results for the remaining 32 twin pairs will be presented in our forthcoming paper.

RECONS CTIO/SMARTS 0.9 m light-curve data shown in this work are available as Data behind the Figure (DbF)

products. The Chandra X-ray observations used here are available from the Chandra Data Archive and are contained in doi:10.25574/cdc.305. CHIRON spectra can be obtained from the NOIRLab Data Archive.

Acknowledgments

A.C. thanks the following individuals for conversations that enhanced this work: Leonardo Paredes, Emily Pass, and Russel White. We also thank Andrei Tokovinin for his assistance in collecting and reducing the SOAR speckle results. We thank the anonymous referee for providing valuable feedback that improved this manuscript. This work has been supported by the NSF through grants AST-141206, AST-1715551, and AST-2108373, as well as via NASA/Chandra grant GO1-22013B. We have used data from the SMARTS 0.9 m telescope, which is operated as part of the SMARTS Consortium by RECONS (www.recons.org) members, and with the assistance of staff at Cerro Tololo Inter-American Observatory. This work has made use of data from the European Space Agency (ESA) mission Gaia, processed by the Gaia Data Processing and Analysis Consortium (DPAC). Funding for the DPAC has been provided by national institutions, in particular the institutions participating in the Gaia Multilateral Agreement. This publication makes use of data products from the Two Micron All Sky Survey, which is a joint project of the University of Massachusetts and the Infrared Processing and Analysis Center/California Institute of Technology, funded by the National Aeronautics and Space Administration and the National Science Foundation. This paper includes data collected by the TESS mission, which are publicly available from the Mikulski Archive for Space Telescopes (MAST) at STScI (2022). This research has made use of NASA’s Astrophysics Data System (ADS), as well as the SIMBAD database (M. Wenger et al. 2000) and VizieR catalog access tool (F. Ochsenbein et al. 2000) operated at CDS, Strasbourg, France. This research has also made use of software provided by the Chandra X-ray Center (CXC) in the application packages CIAO and Sherpa.

Facilities: CTIO:0.9m, CTIO:1.5m (CHIRON), CTIO:2-MASS, FLWO:2MASS, Gaia, TESS, CXO, PO:1.2m, SOAR, LDT.

Software: IRAF (D. Tody 1986, 1993), SExtractor (E. Bertin & S. Arnouts 1996), CIAO (A. Fruscione et al. 2006), Sherpa (P. Freeman et al. 2001), unpopolar (S. Hattori et al. 2022), Astropy (Astropy Collaboration et al. 2013, 2018, 2022), Matplotlib (J. D. Hunter 2007), NumPy (C. R. Harris et al. 2020), and Aladin (F. Bonnarel et al. 2000; T. Boch & P. Fernique 2014).

Appendix Chandra X-Ray Figures

This Appendix provides all of the X-ray light curves (Figure 16) and quiescent X-ray spectral fits (Figure 17) from our Chandra observations, except those already shown earlier in Figures 2 and 3.

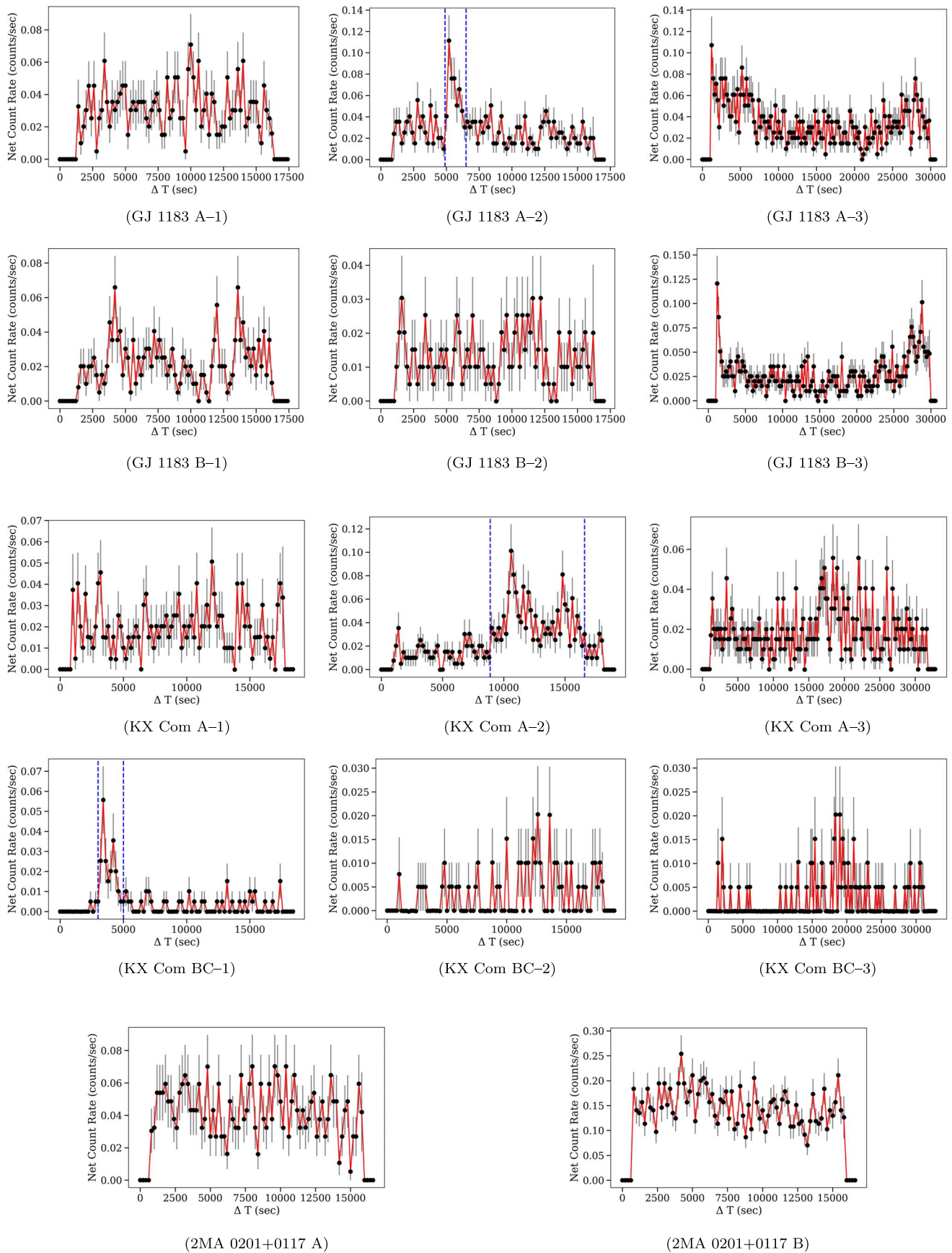


Figure 16. The same as Figure 2, now for all of the remaining X-ray data sets. NLTT 44989 A is not shown, given its lack of a confident detection (see Section 3.4.1).

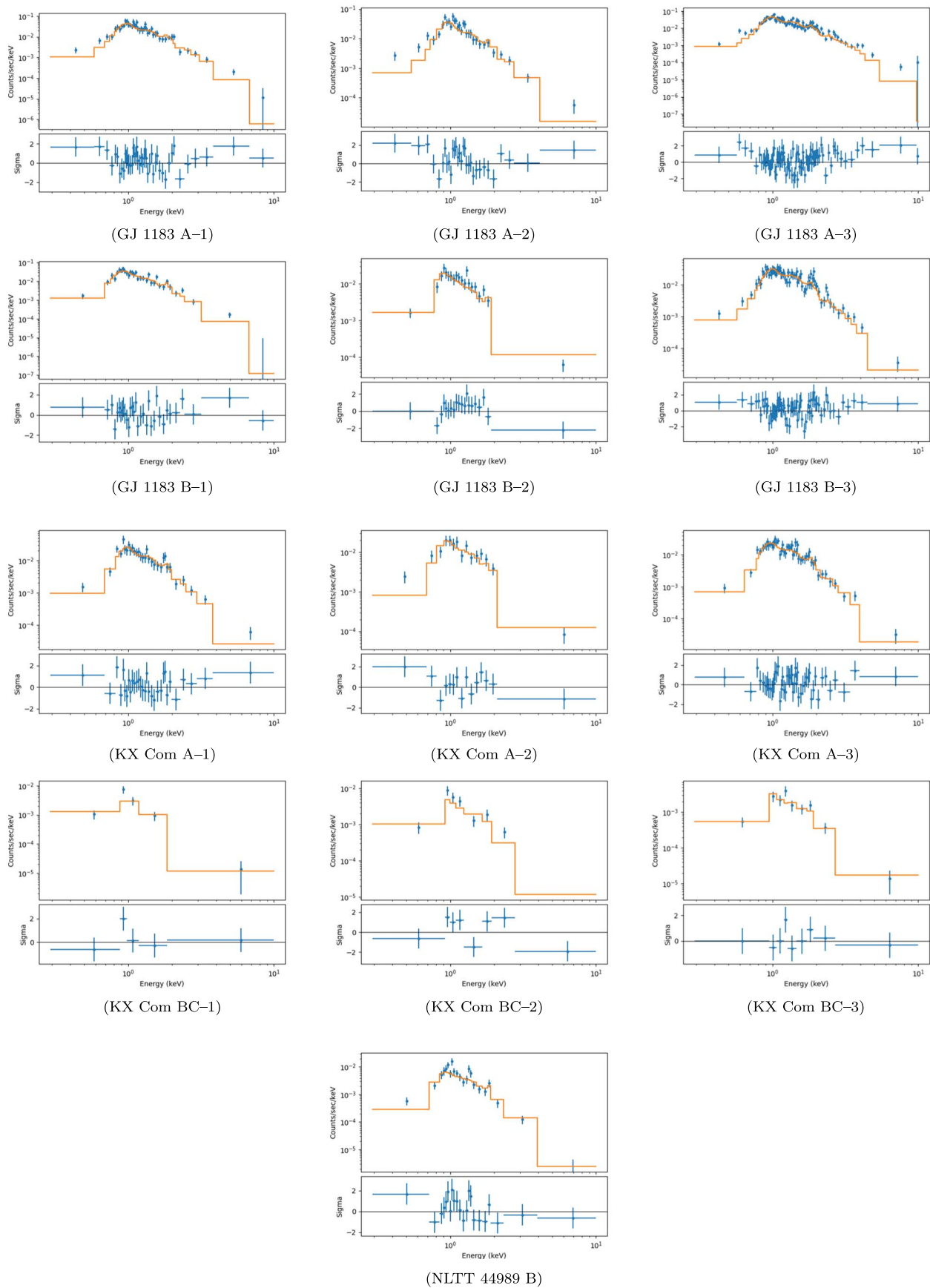


Figure 17. The same as Figure 3, now for all of the remaining quiescent X-ray data sets. NLTT 44989 A is not shown, given its lack of a confident detection (see Section 3.4.1).

ORCID iDs

Andrew A. Couperus  <https://orcid.org/0000-0001-9834-5792>
 Todd J. Henry  <https://orcid.org/0000-0002-9061-2865>
 Rachel A. Osten  <https://orcid.org/0000-0001-5643-8421>
 Wei-Chun Jao  <https://orcid.org/0000-0003-0193-2187>
 Eliot Halley Vrijmoet  <https://orcid.org/0000-0002-1864-6120>
 Aman Kar  <https://orcid.org/0000-0002-9811-5521>
 Elliott Horch  <https://orcid.org/0000-0003-2159-1463>

References

- Alonso-Floriano, F. J., Caballero, J. A., Cortés-Contreras, M., Solano, E., & Montes, D. 2015, *A&A*, **583**, A85
- Ansdell, M., Gaidos, E., Mann, A. W., et al. 2015, *ApJ*, **798**, 41
- Ansdell, M., Williams, J. P., Manara, C. F., et al. 2017, *AJ*, **153**, 240
- Astropy Collaboration, Price-Whelan, A. M., Lim, P. L., et al. 2022, *ApJ*, **935**, 167
- Astropy Collaboration, Price-Whelan, A. M., Sipőcz, B. M., et al. 2018, *AJ*, **156**, 123
- Astropy Collaboration, Robitaille, T. P., Tollerud, E. J., et al. 2013, *A&A*, **558**, A33
- Audard, M., Güdel, M., & Skinner, S. L. 2003, *ApJ*, **589**, 983
- Baluev, R. V. 2008, *MNRAS*, **385**, 1279
- Barnes, J. R., Jeffers, S. V., Haswell, C. A., et al. 2017, *MNRAS*, **471**, 811
- Basri, G. 2021, *An Introduction to Stellar Magnetic Activity* (Bristol: IOP Publishing)
- Bell, K. J., Hilton, E. J., Davenport, J. R. A., et al. 2012, *PASP*, **124**, 14
- Bellm, E. C., Kulkarni, S. R., Graham, M. J., et al. 2019, *PASP*, **131**, 018002
- Benedict, G. F., Henry, T. J., Franz, O. G., et al. 2016, *AJ*, **152**, 141
- Berta, Z. K., Irwin, J., Charbonneau, D., Burke, C. J., & Falco, E. E. 2012, *AJ*, **144**, 145
- Bertin, E., & Arnouts, S. 1996, *A&AS*, **117**, 393
- Bianchi, L., Shiao, B., & Thilker, D. 2017, *ApJS*, **230**, 24
- Boch, T., & Fernique, P. 2014, in *ASP Conf. Ser. 485, Astronomical Data Analysis Software and Systems XXIII*, ed. N. Manset & P. Forshay (San Francisco, CA: ASP), 277
- Bonnarel, F., Fernique, P., Bienaymé, O., et al. 2000, *A&AS*, **143**, 33
- Borucki, W. J., Koch, D., Basri, G., et al. 2010, *Sci*, **327**, 977
- Brown, B. P., Oishi, J. S., Vasil, G. M., Leccoanet, D., & Burns, K. J. 2020, *ApJL*, **902**, L3
- Brown, T. M. 2014, *ApJ*, **789**, 101
- Bryant, E. M., Bayliss, D., & VanEylen, V. 2023, *MNRAS*, **521**, 3663
- Cañas, C. I., Kanodia, S., Libby-Roberts, J., et al. 2023, *AJ*, **166**, 30
- Caldwell, D. A., Tenenbaum, P., Twicken, J. D., et al. 2020, *RNAAS*, **4**, 201
- Cayrel, R. 1988, in *IAU Symp. 132: The Impact of Very High S/N Spectroscopy on Stellar Physics*, ed. G. Cayrel de Strobel & M. Spite (Cambridge: Cambridge Univ. Press), 345
- Chabrier, G., & Baraffe, I. 1997, *A&A*, **327**, 1039
- Chen, X., Wang, S., Deng, L., et al. 2020, *ApJS*, **249**, 18
- Cieza, L. A., Padgett, D. L., Allen, L. E., et al. 2009, *ApJL*, **696**, L84
- Clark, C. A., van Belle, G. T., Horch, E. P., et al. 2020, *Proc. SPIE*, **11446**, 114462A
- Clements, T. D., Henry, T. J., Hosey, A. D., et al. 2017, *AJ*, **154**, 124
- Cook, B. A., Williams, P. K. G., & Berger, E. 2014, *ApJ*, **785**, 10
- Cortés-Contreras, M., Béjar, V. J. S., Caballero, J. A., et al. 2017, *A&A*, **597**, A47
- Cram, L. E., & Mullan, D. J. 1979, *ApJ*, **234**, 579
- Davis, J. E. 2001, *ApJ*, **562**, 575
- De Angeli, F., Weiler, M., Montegriffo, P., et al. 2023, *A&A*, **674**, A2
- Di Stefano, R. 2011, *AJ*, **141**, 142
- Domingo, A., Gutiérrez-Sánchez, R., Rísquez, D., et al. 2010, *ApSSP*, **14**, 493
- Donati, J.-F., Lehmann, L. T., Cristofari, P. I., et al. 2023, *MNRAS*, **525**, 2015
- Douglas, S. T., Agüeros, M. A., Covey, K. R., et al. 2014, *ApJ*, **795**, 161
- Doyle, J. G. 1989, *A&A*, **218**, 195
- Drew, J. E., Gonzalez-Solares, E., Greimel, R., et al. 2014, *MNRAS*, **440**, 2036
- Dsouza, D. 2023, Master's thesis, Univ. of Potsdam, <https://www.aip.de/media/thesis/desmond-dsouza-masterarbeit.pdf>
- Eddy, J. A. 1976, *Sci*, **192**, 1189
- Edwards, S., Strom, S. E., Hartigan, P., et al. 1993, *AJ*, **106**, 372
- El-Badry, K., Rix, H.-W., Tian, H., Duchêne, G., & Moe, M. 2019, *MNRAS*, **489**, 5822
- Engle, S. G., & Guinan, E. F. 2023, *ApJL*, **954**, L50
- Eyer, L., Audard, M., Holl, B., et al. 2023, *A&A*, **674**, A13
- Fabricsius, C., Bastian, U., Portell, J., et al. 2016, *A&A*, **595**, A3
- Farrish, A. O., Alexander, D., Johns-Krull, C. M., & Li, M. 2021, *ApJ*, **916**, 99
- Favata, F., Reale, F., Micela, G., et al. 2000, *A&A*, **353**, 987
- Felce, C., & Fuller, J. 2023, *MNRAS*, **526**, 6168
- Ferraro, F. R., Sabbi, E., Gratton, R., et al. 2006, *ApJL*, **647**, L53
- Fleming, D. P., Barnes, R., Davenport, J. R. A., & Luger, R. 2019, *ApJ*, **881**, 88
- Freeman, P., Doe, S., & Siemiginowska, A. 2001, *Proc. SPIE*, **4477**, 76
- Frost, A. J., Sana, H., Mahy, L., et al. 2024, *Sci*, **384**, 214
- Fruscione, A., McDowell, J. C., Allen, G. E., et al. 2006, *Proc. SPIE*, **6270**, 62701V
- Fuhrmeister, B., Czesla, S., Perdelwitz, V., et al. 2023, *A&A*, **670**, A71
- Gagné, J., Mamajek, E. E., Malo, L., et al. 2018, *ApJ*, **856**, 23
- Gaia Collaboration 2022, *yCat*, **1**/357
- Gaia Collaboration, Brown, A. G. A., Vallenari, A., et al. 2018, *A&A*, **616**, A1
- Gaia Collaboration, Vallenari, A., Brown, A. G. A., et al. 2023, *A&A*, **674**, A1
- Gal, R. R., de Carvalho, R. R., Odewahn, S. C., et al. 2004, *AJ*, **128**, 3082
- Gan, T., Wang, S. X., Wang, S., et al. 2023, *AJ*, **165**, 17
- García Soto, A., Newton, E. R., Douglas, S. T., Burrows, A., & Kesseli, A. Y. 2023, *AJ*, **165**, 192
- Garraffo, C., Drake, J. J., Dotter, A., et al. 2018, *ApJ*, **862**, 90
- Gastine, T., Morin, J., Duarte, L., et al. 2013, *A&A*, **549**, L5
- Gomes da Silva, J., Santos, N. C., Bonfils, X., et al. 2011, *A&A*, **534**, A30
- Guillochon, J., Ramirez-Ruiz, E., & Lin, D. 2011, *ApJ*, **732**, 74
- Gunning, H. C., Schmidt, S. J., Davenport, J. R. A., et al. 2014, *PASP*, **126**, 1081
- Harris, C. R., Millman, K. J., van der Walt, S. J., et al. 2020, *Natur*, **585**, 357
- Harris, R. J., Andrews, S. M., Wilner, D. J., & Kraus, A. L. 2012, *ApJ*, **751**, 115
- Hartman, Z. D., & Lépine, S. 2020, *ApJS*, **247**, 66
- Hattori, S., Foreman-Mackey, D., Hogg, D. W., et al. 2022, *AJ*, **163**, 284
- Hawkins, K., Lucey, M., Ting, Y.-S., et al. 2020, *MNRAS*, **492**, 1164
- Henry, T. J., & Jao, W.-C. 2024, *ARA&A*, **62**, 593
- Henry, T. J., Jao, W.-C., Subasavage, J. P., et al. 2006, *AJ*, **132**, 2360
- Henry, T. J., Jao, W.-C., Winters, J. G., et al. 2018, *AJ*, **155**, 265
- Honeycutt, R. K. 1992, *PASP*, **104**, 435
- Horch, E. P., van Belle, G. T., Davidson, J. W. J., et al. 2015, *AJ*, **150**, 151
- Horch, E. P., Veillette, D. R., Baena Gallé, R., et al. 2009, *AJ*, **137**, 5057
- Hosey, A. D., Henry, T. J., Jao, W.-C., et al. 2015, *AJ*, **150**, 6
- Howard, W. S., Corbett, H., Law, N. M., et al. 2020, *ApJ*, **895**, 140
- Howell, S. B., Sobek, C., Haas, M., et al. 2014, *PASP*, **126**, 398
- Hunter, J. D. 2007, *CSE*, **9**, 90
- Hwang, H.-C., El-Badry, K., Rix, H.-W., et al. 2022, *ApJL*, **933**, L32
- Ibañez Bustos, R. V., Buccino, A. P., Flores, M., & Mauas, P. J. D. 2019a, *A&A*, **628**, L1
- Ibañez Bustos, R. V., Buccino, A. P., Flores, M., et al. 2019b, *MNRAS*, **483**, 1159
- Ibañez Bustos, R. V., Buccino, A. P., Messina, S., Lanza, A. F., & Mauas, P. J. D. 2020, *A&A*, **644**, A2
- Ilić, N., Poppenhaeger, K., Dsouza, D., et al. 2023, *MNRAS*, **524**, 5954
- Ilic, N., Poppenhaeger, K., & Hosseini, S. M. 2022, *MNRAS*, **513**, 4380
- Ilin, E., Poppenhäger, K., Chebly, J., Ilić, N., & Alvarado-Gómez, J. D. 2024, *MNRAS*, **527**, 3395
- Irving, Z. A., Saar, S. H., Wargelin, B. J., & do Nascimento, J.-D. 2023, *ApJ*, **949**, 51
- Irwin, J. M., Charbonneau, D., Esquerdo, G. A., et al. 2018, *AJ*, **156**, 140
- Jackson, R. J., & Jeffries, R. D. 2010, *MNRAS*, **407**, 465
- Janson, M., Hormuth, F., Bergfors, C., et al. 2012, *ApJ*, **754**, 44
- Jao, W.-C., Couperus, A. A., Vrijmoet, E. H., Wright, N. J., & Henry, T. J. 2022, *ApJ*, **940**, 145
- Jao, W.-C., Henry, T. J., Gies, D. R., & Hambly, N. C. 2018, *ApJL*, **861**, L11
- Jao, W.-C., Henry, T. J., Subasavage, J. P., et al. 2011, *AJ*, **141**, 117
- Jao, W.-C., Henry, T. J., White, R. J., et al. 2023, *AJ*, **166**, 63
- Jayasinghe, T., Stanek, K. Z., Kochanek, C. S., et al. 2019a, *MNRAS*, **485**, 961
- Jayasinghe, T., Stanek, K. Z., Kochanek, C. S., et al. 2019b, *MNRAS*, **486**, 1907
- Jenkins, J. M., Twicken, J. D., McCauliff, S., et al. 2016, *Proc. SPIE*, **9913**, 99133E
- Jensen, E. L. N., Mathieu, R. D., & Fuller, G. A. 1996, *ApJ*, **458**, 312
- Kar, A., Henry, T. J., Couperus, A. A., Vrijmoet, E. H., & Jao, W.-C. 2024, *AJ*, **167**, 196
- Kimara, R., Faherty, J. K., Cruz, K. L., et al. 2021, *AJ*, **161**, 277
- Kiraga, M. 2012, *AcA*, **62**, 67
- Kitchatinov, L. L., Moss, D., & Sokoloff, D. 2014, *MNRAS*, **442**, L1
- Kochanek, C. S., Shappee, B. J., Stanek, K. Z., et al. 2017, *PASP*, **129**, 104502

- Kochukhov, O., & Lavail, A. 2017, *ApJL*, **835**, L4
- Koenigl, A. 1991, *ApJL*, **370**, L39
- Kratter, K. M. 2011, in ASP Conf. Ser. 447, Evolution of Compact Binaries, ed. L. Schmidtobreick, M. R. Schreiber, & C. Tappert (San Francisco, CA: ASP), 47
- Lasker, B. M., Doggett, J., McLean, B., et al. 1996, in ASP Conf. Ser. 101, Astronomical Data Analysis Software and Systems V, ed. G. H. Jacoby & J. Barnes (San Francisco, CA: ASP), 88
- Lehmann, L. T., Donati, J.-F., Fouque, P., et al. 2024, *MNRAS*, **527**, 4330
- Leonard, P. J. T. 1989, *AJ*, **98**, 217
- Lindgren, L. 2018, Re-normalising the astrometric chi-square in Gaia DR2 Gaia Technical Note GAIA-C3-TN-LU-LL-124-01, Gaia DPAC, <https://www.cosmos.esa.int/web/gaia/public-dpac-documents>
- Lindgren, L., Klioner, S. A., Hernández, J., et al. 2021, *A&A*, **649**, A2
- Lomb, N. R. 1976, *Ap&SS*, **39**, 447
- Lu, Y., See, V., Amard, L., Angus, R., & Matt, S. P. 2024, *NatAs*, **8**, 223
- Luyten, W. J. 1969, *PMMin*, **21**, 1
- Magaudda, E., Stelzer, B., Osten, R. A., et al. 2024, *A&A*, **687**, A95
- Magaudda, E., Stelzer, B., Raetz, S., et al. 2022, *A&A*, **661**, A29
- Mann, A. W., Dupuy, T., Kraus, A. L., et al. 2019, *ApJ*, **871**, 63
- Mapelli, M., Sigurdsson, S., Ferraro, F. R., et al. 2006, *MNRAS*, **373**, 361
- Masci, F. J., Laher, R. R., Rusholme, B., et al. 2019, *PASP*, **131**, 018003
- Mason, B. D., Wycoff, G. L., Hartkopf, W. I., Douglass, G. G., & Worley, C. E. 2001, *AJ*, **122**, 3466
- Mavridis, L. N., & Avgoloupis, S. 1986, *A&A*, **154**, 171
- Medina, A. A., Charbonneau, D., Winters, J. G., Irwin, J., & Mink, J. 2022a, *ApJ*, **928**, 185
- Medina, A. A., Winters, J. G., Irwin, J. M., & Charbonneau, D. 2022b, *ApJ*, **935**, 104
- Meibom, S., Mathieu, R. D., & Stassun, K. G. 2007, *ApJL*, **665**, L155
- Ment, K., & Charbonneau, D. 2023, *AJ*, **165**, 265
- Messina, S. 2019, *A&A*, **627**, A97
- Messina, S., Lanzafame, A. C., Malo, L., et al. 2017a, *A&A*, **607**, A3
- Messina, S., Millward, M., Buccino, A., et al. 2017b, *A&A*, **600**, A83
- Metzger, B. D., Giannios, D., & Spiegel, D. S. 2012, *MNRAS*, **425**, 2778
- Mondrik, N., Newton, E., Charbonneau, D., & Irwin, J. 2019, *ApJ*, **870**, 10
- Newton, E. R., Irwin, J., Charbonneau, D., et al. 2016, *ApJ*, **821**, 93
- Newton, E. R., Irwin, J., Charbonneau, D., et al. 2017, *ApJ*, **834**, 85
- Newton, E. R., Mondrik, N., Irwin, J., Winters, J. G., & Charbonneau, D. 2018, *AJ*, **156**, 217
- Nisak, A. H., White, R. J., Yep, A., et al. 2022, *AJ*, **163**, 278
- Ochsenbein, F., Bauer, P., & Marcout, J. 2000, *A&AS*, **143**, 23
- Offner, S. S. R., Moe, M., Kratter, K. M., et al. 2023, in ASP Conf. Ser. 534, Protostars and Planets VII, ed. S. Inutsuka et al. (San Francisco, CA: ASP), 275
- Paredes, L. A., Henry, T. J., Quinn, S. N., et al. 2021, *AJ*, **162**, 176
- Pass, E. K., Charbonneau, D., Irwin, J. M., & Winters, J. G. 2022, *ApJ*, **936**, 109
- Pass, E. K., Charbonneau, D., Latham, D. W., et al. 2024, *ApJ*, **966**, 231
- Pass, E. K., Winters, J. G., Charbonneau, D., Irwin, J. M., & Medina, A. A. 2023a, *AJ*, **166**, 16
- Pass, E. K., Winters, J. G., Charbonneau, D., et al. 2023b, *AJ*, **166**, 11
- Petrovich, C. 2015, *ApJ*, **799**, 27
- Pineda, J. S., & Villadsen, J. 2023, *NatAs*, **7**, 569
- Plant, K., Hallinan, G., & Bastian, T. 2024, *ApJ*, **970**, 56
- Pojmanski, G. 1997, *AcA*, **47**, 467
- Popinchalk, M., Faherty, J. K., Kiman, R., et al. 2021, *ApJ*, **916**, 77
- Pourbaix, D., Tokovinin, A. A., Batten, A. H., et al. 2004, *A&A*, **424**, 727
- Pritchard, J., Murphy, T., Heald, G., et al. 2024, *MNRAS*, **529**, 1258
- Privitera, G., Meynet, G., Eggenberger, P., et al. 2016, *A&A*, **591**, A45
- Quiroga-Núñez, L. H., Intema, H. T., Callingham, J. R., et al. 2020, *A&A*, **633**, A130
- Raetz, S., & Stelzer, B. 2024, *A&A*, **687**, A180
- Ranjan, S., Wordsworth, R., & Sasselov, D. D. 2017, *ApJ*, **843**, 110
- Redfield, S., & Linsky, J. L. 2000, *ApJ*, **534**, 825
- Reid, I. N., Hawley, S. L., & Gizis, J. E. 1995, *AJ*, **110**, 1838
- Ricker, G. R., Winn, J. N., Vanderspek, R., et al. 2015, *JATIS*, **1**, 014003
- Riello, M., De Angeli, F., Evans, D. W., et al. 2021, *A&A*, **649**, A3
- Robertson, P., Endl, M., Cochran, W. D., & Dodson-Robinson, S. E. 2013, *ApJ*, **764**, 3
- Robrade, J., & Schmitt, J. H. M. M. 2005, *A&A*, **435**, 1073
- Roquette, J., Matt, S. P., Winter, A. J., Amard, L., & Stasevic, S. 2021, *MNRAS*, **508**, 3710
- Route, M. 2016, *ApJL*, **830**, L27
- Rowell, N., Davidson, M., Lindgren, L., et al. 2021, *A&A*, **649**, A11
- Sarkar, A., Yungelson, L., & Tout, C. A. 2023, *MNRAS*, **526**, 870
- Scargle, J. D. 1982, *ApJ*, **263**, 835
- See, V., Matt, S. P., Finley, A. J., et al. 2019, *ApJ*, **886**, 120
- See, V., Roquette, J., Amard, L., & Matt, S. P. 2021, *ApJ*, **912**, 127
- Shappee, B., Prieto, J., Stanek, K. Z., et al. 2014, AAS Meeting Abstracts, **223**, 236.03
- Shields, A. L., Ballard, S., & Johnson, J. A. 2016, *PhR*, **663**, 1
- Shulyak, D., Sokoloff, D., Kitchatinov, L., & Moss, D. 2015, *MNRAS*, **449**, 341
- Skrutskie, M. F., Cutri, R. M., Stiening, R., et al. 2006, *AJ*, **131**, 1163
- Skumanich, A. 1972, *ApJ*, **171**, 565
- Stassun, K. G., & Torres, G. 2021, *ApJL*, **907**, L33
- Stauffer, J. R., & Hartmann, L. W. 1986, *ApJS*, **61**, 531
- STScI 2022, TESS Calibrated Full Frame Images: All Sectors, STScI/MAST, doi:10.17909/0CP4-2J79
- Suárez Mascareño, A., Rebolo, R., & González Hernández, J. I. 2016, *A&A*, **595**, A12
- Tarter, J. C., Backus, P. R., Mancinelli, R. L., et al. 2007, *AsBio*, **7**, 30
- Tody, D. 1986, *Proc. SPIE*, **0627**, 733
- Tody, D. 1993, in ASP Conf. Ser. 52, Astronomical Data Analysis Software and Systems II, ed. R. J. Hanisch, R. J. V. Brissenden, & J. Barnes (San Francisco, CA: ASP), 173
- Tokovinin, A. 2018, *PASP*, **130**, 035002
- Tokovinin, A. 2023, *AJ*, **165**, 180
- Tokovinin, A., Cantarutti, R., Tighe, R., et al. 2016, *PASP*, **128**, 125003
- Tokovinin, A., Fischer, D. A., Bonati, M., et al. 2013, *PASP*, **125**, 1336
- Tokovinin, A., Mason, B. D., & Hartkopf, W. I. 2010, *AJ*, **139**, 743
- Trigilio, C., Biswas, A., Leto, P., et al. 2023, arXiv:2305.00809
- Valtonen, M., & Mikkola, S. 1991, *ARA&A*, **29**, 9
- VanderPlas, J. T. 2018, *ApJS*, **236**, 16
- Vrijmoet, E. 2023, Dissertation, Georgia State Univ., doi:10.57709/35866812
- Vrijmoet, E. H., Henry, T. J., Jao, W.-C., & Dieterich, S. B. 2020, *AJ*, **160**, 215
- Vrijmoet, E. H., Tokovinin, A., Henry, T. J., et al. 2022, *AJ*, **163**, 178
- Wargelin, B. J., Saar, S. H., Pojmański, G., Drake, J. J., & Kashyap, V. L. 2017, *MNRAS*, **464**, 3281
- Wenger, M., Ochsenbein, F., Egret, D., et al. 2000, *A&AS*, **143**, 9
- Wolf, C., Onken, C. A., Luvaul, L. C., et al. 2018, *PASA*, **35**, e010
- Wolk, S., Kashyap, V., Yadav, R., et al. 2022, in The 21st Cambridge Workshop on Cool Stars, Stellar Systems, and the Sun, ed. A. S. Brun, J. Bouvier, & P. Petit (Toulouse: Zenodo), 151
- Woźniak, P. R., Vestrand, W. T., Akerlof, C. W., et al. 2004, *AJ*, **127**, 2436
- Wright, J. T., & Eastman, J. D. 2014, *PASP*, **126**, 838
- Wright, N. J., Drake, J. J., Mamajek, E. E., & Henry, G. W. 2011, *ApJ*, **743**, 48
- Wright, N. J., Newton, E. R., Williams, P. K. G., Drake, J. J., & Yadav, R. K. 2018, *MNRAS*, **479**, 2351
- Wu, Y., & Murray, N. 2003, *ApJ*, **589**, 605
- Yadav, R. K., Christensen, U. R., Wolk, S. J., & Poppenhaefer, K. 2016, *ApJL*, **833**, L28
- Zechmeister, M., & Kürster, M. 2009, *A&A*, **496**, 577